


UNIVERSITÀ DEGLI STUDI DI MILANO &
UNIVERSITÀ CATTOLICA DEL SACRO CUORE

SCUOLA DI DOTTORATO IN
FISICA, ASTROFISICA E FISICA APPLICATA

DIPARTIMENTO
MATEMATICA E FISICA

DOTTORATO DI RICERCA IN
FISICA, ASTROFISICA E FISICA APPLICATA
Ciclo XXVII

Carbon-based hybrid platforms for novel photovoltaic devices: buried interface chemistry and charge carriers dynamics

Settore scientifico disciplinare FIS/03

Coordinatore: Prof. Marco Bersanelli
Tutore: Prof. Luigi Sangaletti

Tesi di Dottorato di:
Chiara Pintossi

Anno Accademico 2014-2015

A Davide,
ovunque sia o non sia,
perché vivere non é esistere.

A poet once said: the whole universe is in a glass of wine. We will probably never know in what sense he meant it, for poets do not write to be understood. But it is true that if we look at a glass of wine closely enough we see the entire universe. There are the things of physics: the twisting liquid which evaporates depending on the wind and weather, the reflection in the glass; and our imagination adds atoms. The glass is a distillation of the earth's rocks, and in its composition we see the secrets of the universe's age, and the evolution of stars. There are the ferments, the enzymes, the substrates, and the products. There in wine is found the great generalization; all life is fermentation. How vivid is the claret, pressing its existence into the consciousness that watches it! If our small minds, for some convenience, divide this glass of wine, this universe, into parts (physics, biology, geology, astronomy, psychology, and so on), remember that nature does not know it! So let us put it all back together, not forgetting ultimately what it is for. Let it give us one more final pleasure: drink it and forget it all!

Una volta un poeta disse: L'universo intero é in un bicchiere di vino. Probabilmente non sapremo mai in che senso lo disse, perché i poeti non scrivono per essere compresi. Ma é vero che se osserviamo un bicchiere di vino abbastanza attentamente vediamo l'intero universo. Ci sono le cose della fisica: il liquido turbolento e in evaporazione in funzione del vento e del tempo, il riflesso sul vetro del bicchiere, e la nostra immaginazione aggiunge gli atomi. Il vetro é un distillato delle rocce della Terra, e nella sua composizione vediamo i segreti dell'etá dell'universo e l'evoluzione delle stelle. Ci sono i fermenti, gli enzimi, i reagenti e i prodotti. Nel vino si trova la grande generalizzazione: tutta la vita é fermentazione. Com'é vivido il novello, che imprime la sua esistenza nella consapevolezza di chi lo osserva! Se le nostre fragili menti, per convenienza, dividono il bicchiere di vino, l'universo, in parti (fisica, biologia, geologia, astronomia, psicologia e cosí via) ricordiamoci che la natura non lo sa! Quindi rimettiamo tutto insieme ma non dimenticandoci a cosa serve. Lasciamo che ci regali ancora un ultimo piacere: beviamolo e dimentichiamoci di tutto!

Richard P. Feynman (1918-1988)

Contents

Introduction and outline

Current photovoltaic (PV) market is strongly dominated by an intense use of silicon. Although it is the second most abundant element on the Earth crust, after oxygen, Si is never present in its pure form but always bounded with other elements, and relatively complex and expensive purification procedures are needed in order to have clean, crystalline and optimally doped pure silicon.

This issue, joined with the ever-increasing demand of clean Si by almost all the technological modern applications, led scientists all over the world to look for suitable alternatives.

One of the most promising options, is to try to substitute silicon with carbon, essentially for two reasons: (i) pure C not only exists in nature but can also be obtained and purified through easy and low-cost processes, (ii) carbon can behave as a metal or a semiconductor without being doped, depending only on the particular allotrope.

Moreover, carbon allotropes capability of arranging in various geometry allows C-based materials to assume different dimensionality, starting from the quasi zero-dimensional fullerene to three-dimensional diamonds. This makes carbon nanomaterials excellent candidate for a wide range of electrical and technological devices, offering the possibility to chose the suitable allotropes depending on the particular task that is needed to be fulfilled.

For photovoltaic application, a semiconducting material which can provide dissociation sites for excitons is necessary. To accomplish this role, the monodimensional form of C, carbon nanotubes (CNTs), revealed to be a perfect substitute of p-type silicon, on one side of the junction because CNTs are naturally p-doped in air. Moreover, thanks to their peculiar geometry and extraordinary electrical conductivity, they are able to provide excellent transport path for

the dissociated carriers with a very good transparency (which allows a relevant amount of incident light to reach the depletion region).

In the first chapter of this thesis, carbon nanotubes will be introduced, emphasizing the properties which make this nanostructured materials optimal for PV applications. Then, the different types of carbon/silicon heterojunctions will be analyzed, starting from the classical semiconductor theory, to a more complex and realistic model. At the end of the chapter CNTs solar cells state of the art will be presented, highlighting the open questions at which this thesis is aimed to answer.

The experimental techniques, such as angle-resolved X-rays photoelectron spectroscopy (AR-XPS) and transient reflectivity (TR) measurements, used to reach this goal will be presented in Chapter 2, together with the description of the manufacturing processes that yielded to the creation of three different series of PV devices, with an improvement of the efficiency from 0.1% to 12.2% in three years.

In the third chapter, we will show how the complex buried interface between CNTs and Si can be investigated and modelled by means of photoelectron spectroscopy techniques. A complex oxide interface, composed by silicon dioxide (SiO_2) and non-stoichiometric silicon oxide (SiO_x), has been unveiled and possible effects on the power conversion efficiency of PV devices are outlined.

A systematic study on the chemical and physical properties of the buried interface will be presented in Chapter 4. Oxides have been alternatively removed and regrown using suitable acids and the effects on the PV performances will be discussed in detail in this chapter. The doping effects of acids on the carbon nanotubes will also be investigated through Raman spectroscopy. Acid effects on the heterojunctions will be unambiguously shown by the XPS measurements, and the matching of these data with the electrical PV measurements allows us to discuss the nature of the heterojunction in more detail.

In order to properly address the operation mechanism of these devices, which can be either a conventional p-n or a metal-insulator-semiconductor (MIS) junc-

tion, the dynamics of charge transfer processes at the interface will be investigated in Chapter 5 with time-resolved pump-probe reflectivity measurement. The aim is to find a correlation between the thickness of the buried SiO_x layer and the carriers photogeneration and transport, comparing the device electrical parameter with the ultrafast behavior, analyzed by time-resolved reflectivity.

These last findings, along with several improvements in the CNTs dispersion and deposition, have led to the creation of optimized third-series solar cells with a record efficiency of 12.2%, which will be fully characterized at the end of this last chapter through a combination of suitable experimental techniques, in order to highlight the factors which contributed to this huge jump in the power conversion efficiency. The stability in time of this optimized PV devices will finally be discussed.

Chapter 1

Carbon Nanotubes and Carbon-based Hybrid Heterojunctions

Abstract

Carbon nanotubes play a central role in the field of nanotechnology, because of their peculiar electrical, mechanical and optical properties, arising from their monodimensional geometry. Here, the properties of carbon nanotubes are discussed, starting from their crystalline structure, in order to understand their optical, electrical and vibrational behaviour. In the second section, the most popular CNT synthesis mechanism are presented, while the last section is devoted to analyse the heterojunction between CNTs and Silicon, in order to understand why it is at the basis of a wide variety of applications, focusing in particular on photovoltaic devices.

1.1 Carbon nanotubes

Even though carbon filaments with a diameter of less than 10 nm were produced in 70's and 80's [1–5], it was only after the first observation with

high resolution transmission electron microscopy (HRTEM) of carbon nanotubes (CNTs) by Iijima in 1991 [6] that CNT field boosted up significantly, attracting more and more scientist all over the world. The simplest and fundamental type

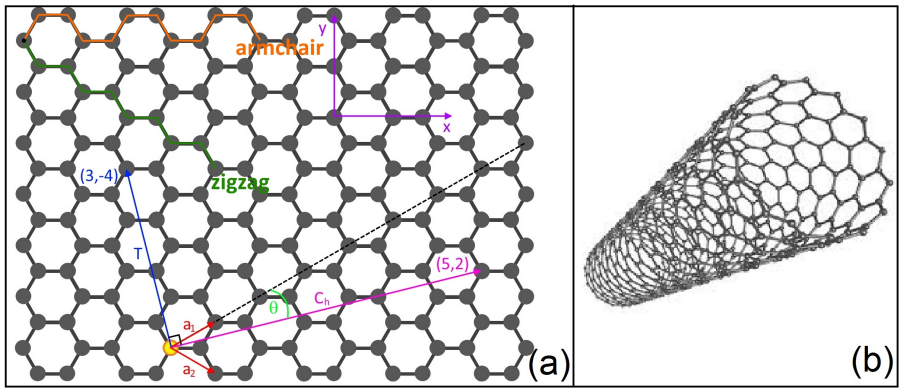

Figure 1.1: (a) Schematic representation of the graphene Bravais lattice in which the vectors $\mathbf{a}_1$, $\mathbf{a}_2$, $\mathbf{C}_h$ and $\mathbf{T}$ are highlighted for a (5,2) SWCNT. (b) A SWCNT obtained by rolling a single graphene sheet.

of CNTs is represented by single walled carbon nanotubes (SWCNT) which can be schematized as a single graphene sheet, rolled up to form a cylinder. Because the tube properties [7] are dramatically influenced by the way in which the graphene sheet is rolled, it worth to clearly understand the geometry of nanotubes and their relationship with graphene crystalline structure. Starting from the basis vectors of the graphene hexagonal honeycomb Bravais lattice, $\mathbf{a}_1$ and $\mathbf{a}_2$ represented in Fig.1.1, it is possible to express the circumference of any carbon nanotube in term of the chiral vector $\mathbf{C}_h$, which is defined as the linear combination of the basis vectors: $\mathbf{C}_h = n\mathbf{a}_1 + m\mathbf{a}_2$. The pair of integer (n,m) uniquely defines the chiral vector and is called nanotube chirality. Nanotubes with $m = 0$ are called zigzag, if $m = n$, the tube is denoted as armchair, while all the other CNTs are simply called chiral. The other unit lattice vector $\mathbf{T}$, perpendicular to the chiral vector can be also expressed in terms of n, m, $\mathbf{a}_1$ and $\mathbf{a}_2$ as:

$$T = \frac{(2m+n)}{b_R}\mathbf{a}_1 - \frac{m+2n}{b_R}\mathbf{a}_2 \tag{1.1}$$

where b_R is equal to $3b$, if $m - n$ is a multiple of $3b$, or b_R=b, when $m - n$ is not a multiple of $3b$, with b being the greatest common divisor between m and n. The tube diameter d is given by:

$$d = \frac{C_h}{\pi} = \frac{\sqrt{3}a_{C-C}}{\pi}\sqrt{m^2 + mn + n^2} \tag{1.2}$$

where a_{C-C} is the lenght of the carbon-carbon bond length (1.42 Å), i.e. the hexagon side in Fig.1.1. The chiral angle ϑ, defined as the angle between $\mathbf{C}_h$ and $\mathbf{a}_1$, is:

$$\vartheta = \tan^{-1}\frac{\sqrt{3}n}{2m + n} \tag{1.3}$$

and varies from $\vartheta = 0°$ for zigzag nanotubes to $\vartheta = 30°$ for the armchair ones. The number of hexagons in each unit cell is given by:

$$N = \frac{2}{b_R}(m^2 + mn + n^2), \tag{1.4}$$

from this equation, it follows that the CNT unit cell is N time larger than that of graphene. Theoretical studies predicted CNT electronic properties to

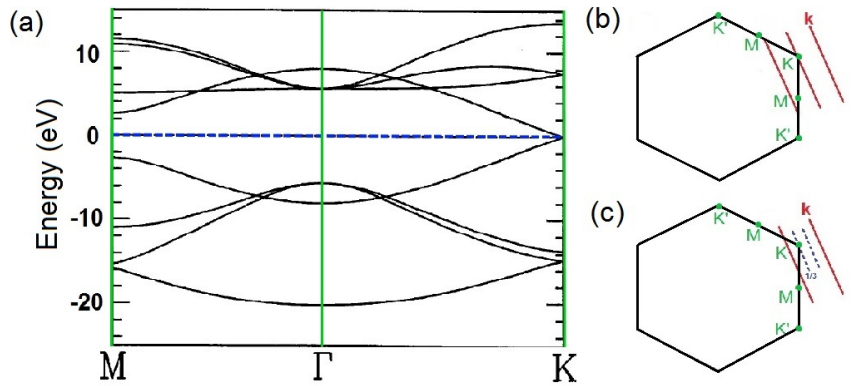

Figure 1.2: (a) Tight-binding band structure of graphene. The wave vector **k** for a 1D CNT is shown in the 2D Brillouin zone of graphite, in red, for (b) metallic and (c) semiconducting tubes.

be very sensitive to their geometrical structure. In fact, although graphene is a

zero-gap semiconductor, single walled carbon nanotubes can be either metallic or semiconducting, depending only on their chiral index (n,m). The electronic structure around the Fermi level of an isolated graphene sheet is given by an occupied π-band and an unoccupied π^*-band, characterized by having both linear dispersion and by crossing the Fermi level at the K point of the Brillouin zone (Figure 1.2a). When a graphene sheet is rolled to form a tube, only some **k** states are allowed, due to the periodic boundary conditions imposed in the circumferential direction. Whenever the set of allowed **k** states includes the K point (Figure 1.2b), the system has a non-zero density of states (DOS) at the Fermi level and is then a metal with two linear dispersing bands; otherwise, when the K point is located at one-third of the distance between two adjacent allowed **k** (Figure 1.2c), the CNT is a semiconductor with a variable energy band gap. All nanotubes with $n - m = 3b$, where b is an integer, are metallic, all the other are semiconductors. Each parallel k-line describes one pair of conduction and valence sub-bands in the nanotube. Transitions at the bandgaps of such sub-band pairs lead to strong optical resonances, and these transitions are traditionally labelled S_{ii} for semiconducting and M_{ii} for metallic nanotubes, where i is the sub-band index. Multi-walled nanotubes (MWCNTs) consist of multiple rolled layers (concentric tubes) of graphene, as in a Russian doll model. Individual shells in MWCNTs can be described as SWCNTs, which can be metallic or semiconducting. Because of statistical probability and restrictions on the relative diameters of the individual tubes, a MWCNT is usually a zero-gap metal. The 1D density of states of CNT, derived straightforward from the graphite one [8], increases when the energy band E(**k**) becomes flat as a function of k, giving rise to one-dimensional van Hove singularities (vHs) in the DOS, as shown in Figure 1.3; vHs are important for determining many solid state properties of carbon nanotubes, such as the Raman spectroscopy.

On the basis of tight binding calculations a simple relation between nanotube diameter d and the transition energies $E_{sc,m}$, the energy separation between the van Hove singularities, valid both for semiconducting (sc) and metallic (m) SWCNT can be determined:

$$E_{sc,m} = 2i\frac{\gamma_0\ a_{C-C}}{d} \tag{1.5}$$

with $i = 1$ for S_{11}, $i = 2$ for S_{22} and $i = 3$ for M_{11}; $\gamma_0 = 2.9$ eV is the nearest neighbour carbon-carbon interaction energy and $a_{C-C} = 0.144$ nm is the

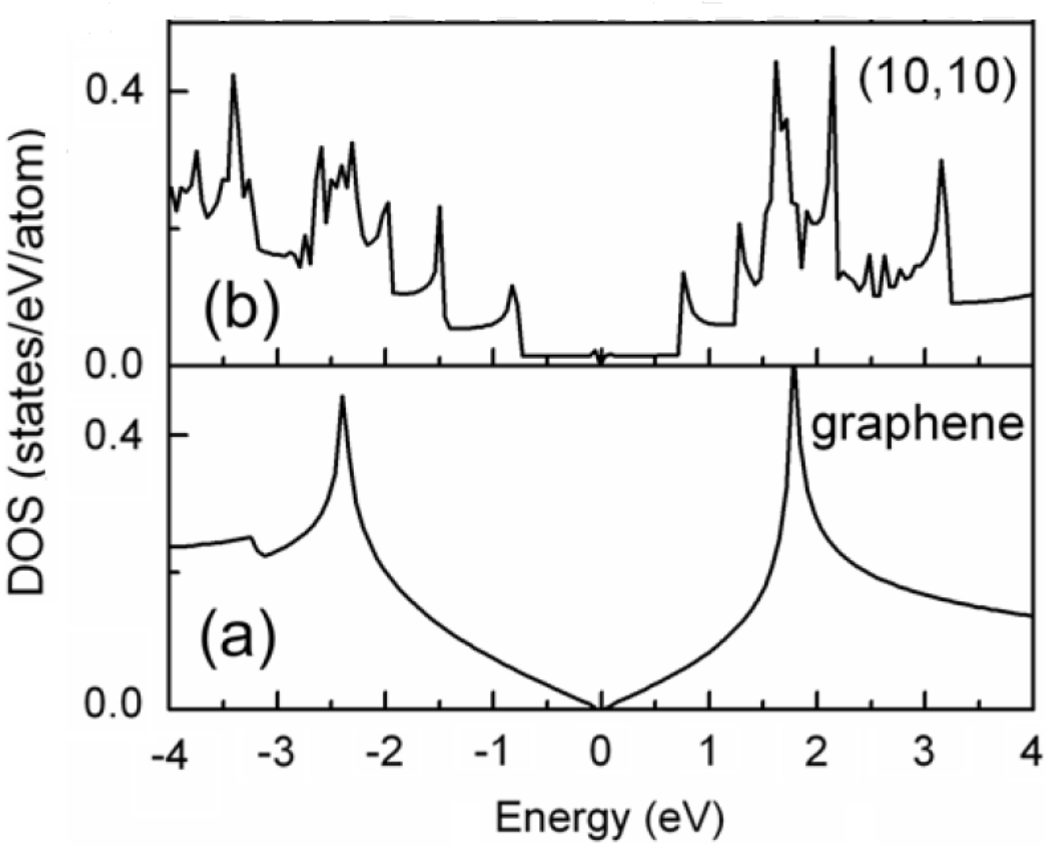

Figure 1.3: The density of state of graphene (a) is compared to the CNTs one (b). As a result of the 1D confinement in CNTs gives rise to the characteristic van Hove singularities.

nearest neighbour carbon-carbon distance. In UV/Vis/NIR absorption spectroscopy [9], the optical transitions, arising from vHs, are probed. After the light absorption, electrons in the van Hove singularities of the valence band jumps to the corresponding energy levels in the conduction band (the S_{11} and S_{22} in semiconducting tubes), while crossed transitions such as S_{12} and S_{21}

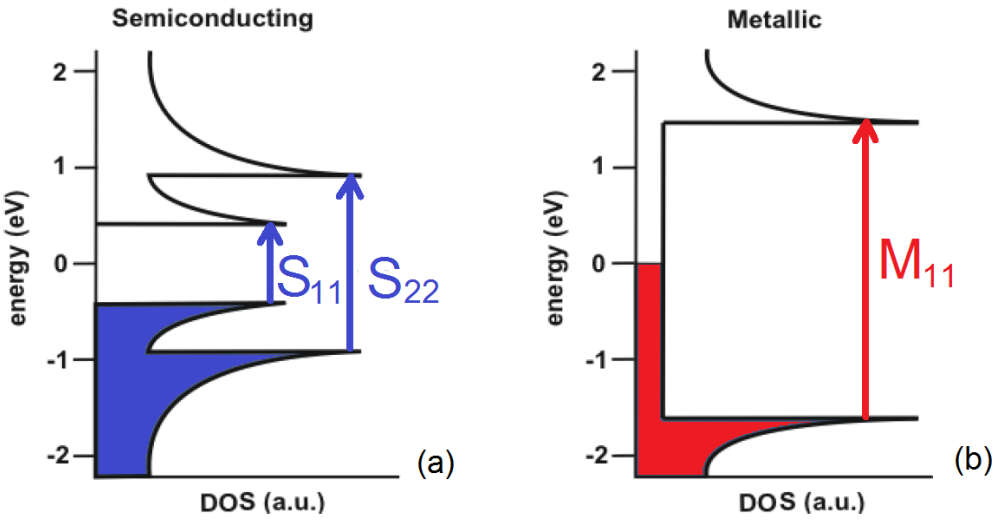

Figure 1.4: The density of state of semiconducting (a) and metallic (b) are sketched, highlighting the S_{11}, S_{22} an M_{11} transitions. These transitions give rise to the three peaks in the optical absorption spectrum (c).

are forbidden by selection rules. In principle, the same process happens in the case of metallic SWCNTs. However, the spacing between the van Hove singularities is larger so that only M_{11} transitions can be probed in the UV/Vis region (Figure 1.4). Besides the van Hove singularities in the phonon DOS, carbon nanotubes also exhibit some other unusual aspects regarding their phonon dispersion relations [10], such as four acoustic branches. In addition to the longitudinal acoustic and transverse acoustic modes, there are two acoustic twist modes for rigid rotation around the tube axis, which are important for heat transport and charge carrier scattering. In SWCNTs, the G band, present also in graphene, which is split into many features around 1580 cm^{-1}, and the lower frequency radial breathing mode (RBM) are usually the strongest features in Raman spectra, and are both first-order Raman modes (Figure 1.5). The RBM is a unique phonon mode, appearing only in carbon nanotubes and its observation in the Raman spectrum provides direct evidence that a sample contains SWCNTs. The RBM is a bond stretching out-of-plane phonon mode for which

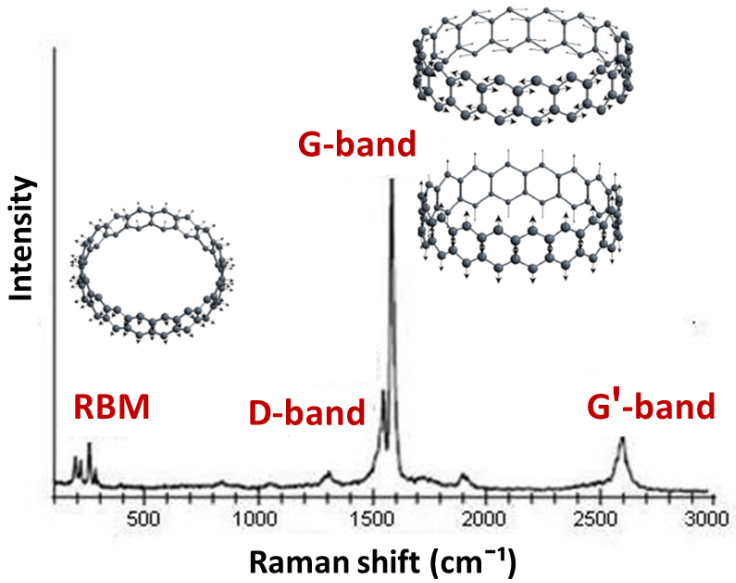

Figure 1.5: Raman spectrum of a SWCNT. The vibrational modes associated to RBMs and the G-band are represented.

all the carbon atoms move coherently in the radial direction, and whose frequency is about 100-500 cm^{-1}. The RBM frequency is inversely proportional to the tube diameter.

Carbon materials presents also two relatively weak Raman signals whose phonon frequencies change with different laser excitation energy, which is called *dispersive* behavior. Both in graphite and in SWCNTs, the D-band at 1350 cm^{-1} and the G′-band at 2700 cm^{-1} (for a laser photon energy of 2.41 eV) are, respectively, due to one- and two-phonon, second-order Raman scattering processes. In particular, because the D-band was firstly observed in the presence of defects in an otherwise perfect infinite graphite structure, it has to be associated to structural defects in the sample.

1.2 Carbon/silicon heterojunctions

Carbon materials are highly versatile due to the different combinations of sp^2 and sp^3 carbon bonds (Figure 1.6a). In contrast, silicon, the close neighbor of carbon in the periodic table, and one of the best understood elements in research, is incapable of forming multiple bonds because of low $p_\pi - p_\pi$ orbital overlap in multiple bonds (Figure 1.6b) [11]. Wang *et al.* [12] investigated the $\pi-$bond energies of various materials and obtained the bond energy of $C = C$ is 2.84 eV and the $Si = Si$ bond energy is 1.0 eV. If high-quality carbon layers

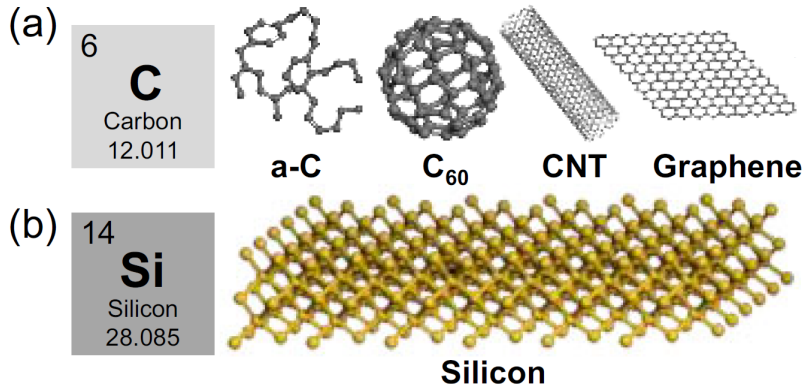

Figure 1.6: Selected structures of carbon and silicon building and the model of carbon/Si heterojunction solar cells. a) Based on the common graphite, four classes of carbon allotropes are shown here: a-C, fullerene, CNTs, and graphene. b) Silicon. c) The typical structure of C/Si heterojunction solar cells.

with different bandgaps can be prepared, efficient devices based on the C/Si heterojunction could be constructed, such as for example sensors, transistors and solar cells.

It should be noticed that there are obvious differences in the contact type between carbon and silicon, depending in particular on the carbon material geometries. Compared to the limited contact area between CNTs or fullerens (C_{60}) and Si, a carbon film, such as graphene or amorphous carbon (a-C) film, could exhibit surface-to-surface contact with planar silicon. However, the contact between carbon and silicon is not always perfect due to the roughness and

wrinkles of the thin film. The structure of the C/Si heterojunction will be discussed here firstly in an ideal and simplified situation in which a perfect junction between C and Si is created. In C/Si solar cells, the carbon layer serves multiple functions, including window electrode, hole collector, and antireflection layer. The working mechanism of C/Si solar cells can be characterized, in first approximation, by the classic theory of semiconductor physics.

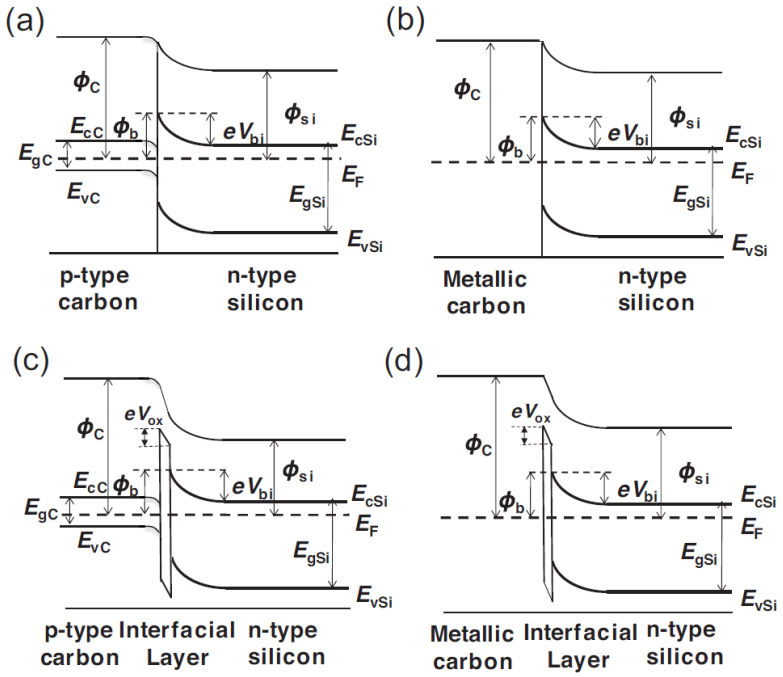

Figure 1.7: Energy-band diagrams of the C/Si heterojunction: a) p-n junction and b) Schottky (metal/semiconductor) junction. When an insulating layer lies between carbon and silicon, the energy-band diagrams of the heterojunction needs to be modified as shown in (c) and (d), respectively.

1.2.1 C/Si junction in thermal equilibrium

In figure 1.7, the energy band diagram of the possible C-Si heterojunction, in thermal equilibrium is shown. E_{gC} and E_{gSi} represent the bandgaps of carbon and silicon, E_{cC} and E_{cSi} are the conduction band energies, E_{vC} and E_{vSi} are the valence band energies, E_F is the energy of the Fermi level. The work functions carbon and silicon are respectively φ_C and φ_{Si}, and in the ideal thermal equilibrium diagram, φ_b is the ideal barrier height and V_{bi} is the built-in potential barrier.

Carbon materials can form two types of heterojunctions when placed in contact with silicon substrates: p-n (semiconductor/semiconductor) junction (Figure 1.7a) and Schottky (metal/semiconductor) junctions (Figure 1.7b).

The semiconducting properties enable carbon nanomaterials, such as a-C, C_{60} , CNTs and graphene, to form p-n junctions with Si. Generally, a diffusion process of charge carriers at the interface level occurs when p-type carbon (p-C) materials are placed in contact with n-type silicon (n-Si), due to the concentration difference of electrons and holes. From the basic semiconductor physics, the total current density J is given by two terms: (i) the *drift* current, due to the electric field inside the junction and (ii) the *diffusion* current depending on the variation of carrier concentration.

$$J = qn\mu E + qD\frac{dn}{dx} \tag{1.6}$$

where D is the diffusion coefficient for the electron in the considered medium, n is the number of electrons per unit of volume, q is the charge of one electron, μ is electron mobility in the medium, and E the electric field. Once the junction is made, holes are injected into the n-Si, and electrons move towards the p-C. As a result of the charge diffusion, the charge neutrality is broken and a built-in field is formed, which hinders further carrier drift. The injection process would bend the energy band of C and Si. The energy band of the p-C bends down to approach the Fermi level, while n-Si would be away from the Fermi level. While the drift current is always in the same of the electric field, the diffusion current direction can switch with a variation of charge carrier concentration. In particular, it can be demonstrate that, when no external voltage is applied, the drift current totally balances the diffusion current, hence, the net current is always zero.

A similar picture holds in the conditions of a Schottky junction between metallic carbon materials and n-Si, with differences in the magnitude of the reverse saturation current and the switching characteristics. Another interesting condition that we will discuss in more detail during this thesis, occurs when an interfacial insulating layer (usually represented by silicon oxides) exists between the carbon layer and the silicon substrate in the heterojunction (Figure 1.7 c,d). With the existence of the insulating layer, the barrier height of the heterojunction is enlarged. The carrier transport mechanism through the insulating layer would either be tunnelling or recombination. Especially in case *d*, but also in *c*, the device operation mechanism is better described by the Metal-Insulator-Semiconductor (MIS) picture.

1.2.2 C/Si heterojunction at non-equilibrium conditions

In order to understand C/Si solar cells operation, the thermal equilibrium picture is not indicative of the real physical situation and the introduction of an applied bias voltage is used to simulate the effects of illumination in order to understand the complex mechanism of generation, transport, and separation of charge carriers occurring at the interface of the C/Si heterojunction.

When a bias voltage is applied to the junction, positive charges will accumulate near the surface of the silicon side and negative charges appear on the other side, near the p-C layer, due to the electrons departing from the n-Si. In this way, the direction of the built-in field is from the silicon to the carbon. When a positive bias is applied from the p-C to the n-Si in the C/Si heterojunction, the potential barrier of the C/Si junction becomes lower and the diffusion current increases, whereas the drift current decreases. The total current, in this case, is fairly high due to the dominant contribution of majority carriers. In contrast, the total current caused by minority carriers is quite low when a negative bias is applied to the C/Si heterojunction.

For this reason, when the C/Si heterojunction is illuminated, the thermal equilibrium is shifted out of balance as shown in Figure 1.8. As photons are absorbed by the heterojunction, photons with energy larger than the bandgap can excite electrons in the valence band to the conduction band, leaving a hole at the place an electron previously occupied. At this point, the photogenerated carriers can be separated due to the built-in field. The work function of carbon

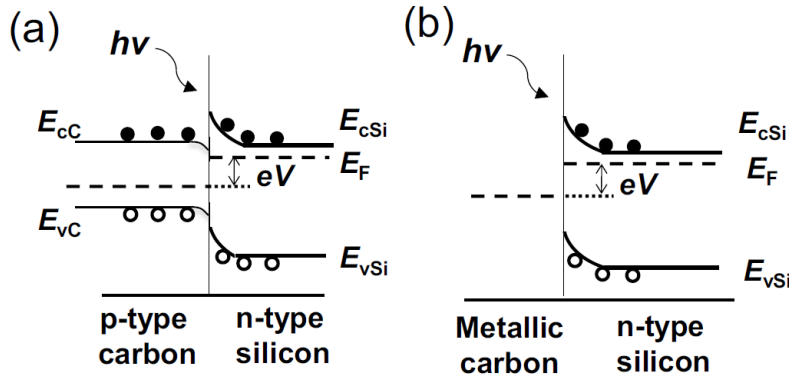

Figure 1.8: Energy-band diagrams of the C/Si heterojunction upon illumination. The energy-band diagrams of the heterojunction for an open circuit are shown as: a) p-n junction and b) Schottky junction, respectively.

layer can be adjusted in order to get a higher built-in field, hence improving the junction's capability to collect photogenerated carriers.

1.2.3 C/Si solar cells

So far, the C/Si junctions had been treated considering simply a general *carbon layer* without specifying anything about the properties of the top layer. This vision, however, risks to be too simplistic, because carbon has the capability of forming a large number of allotropes, the most common being summarized in Figure 1.9. Since every carbon allotropic form displays peculiar optical, mechanical and electrical properties, it worth to treat these heterojunctions with more details, separately.

Over the years, the use of inorganic semiconducting materials has dominated the solar energy conversion market. However, the production of organic or mixed organic/inorganic solar cells has visibly increased the potential of solar energy conversion and made an impact with a broad range of innovative technologies. The photovoltaic effect involves the generation of electron and hole pairs and their subsequent collection at the opposite electrodes.

Both in organic and inorganic materials, the photon absorption causes a de-

localization of the excited states, which leads to a generation of bound electron-hole pairs called *excitons*. These excitons have to dissociate into free charges in order to be transported to the electrodes. Exciton dissociation is known to occur in strong electric fields normally found at polymer-metal interfaces and at dissociation centres, such as oxygen impurities acting as electron traps. This feature has led to the idea of blending polymers with electron acceptor molecules, having a larger electron affinity than the polymer. Under these conditions, internal junctions between the electron donating polymer and the electron acceptor molecule are created. This allows the preferential transfer of the electrons into the electron acceptor molecule while leaving the holes to be preferentially transported through the polymer, a process known as *photoinduced charge transfer*.

Since the discovery of photoinduced charge transfer between conjugated polymers as donor and C_{60} and carbon nanotube, as acceptors, several efficient photovoltaic systems using a combination of polymer and carbon allotropes have been fabricated.

Single-wall carbon nanotubes are attractive platforms for photovoltaic applications because possess extended π-electron systems, in combination with photoexcitable electron donors, which could be useful for novel, highly efficient photo-electrochemical. In fact, SWCNT are good electron acceptors and, at the same time, one-dimensional nanowires. Therefore, they are ready to accept electrons, which are then transported with high efficiency. In light of this feature, the combination of SWCNT with donor groups represent a novel concept to harvest solar energy and convert it into useful electricity. PV devices are fabricated from thin films of organic semiconductors, such as polymers and small-molecule compounds, and are typically on the order of 100 nm thick or less. Because polymer based PVs can be made using a coating process such as spin coating or inkjet printing, they are an attractive option for inexpensively covering large areas as well as flexible plastic surfaces, a promising low cost alternative to silicon solar cells. There is a large amount of research being dedicated throughout industry and academia towards developing PVs and increasing their power conversion efficiency. For a summary about solar cells properties and characterizing parameters, see appendix A.

a-C/Si PV heterojunctions: The first C/Si heterojunction was fabricated and reported by Bhagavat and Nayak in 1979 [13] where amorphous carbon

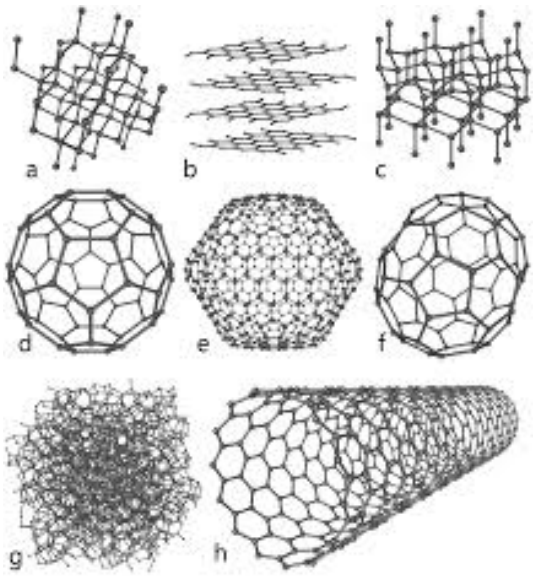

Figure 1.9: Some carbon allotropes: a) diamond, b) graphite, c) lonsdaleite, d) (Buckminster)fullerene (C_{60}), e) fullerite (C_{540}), f) C_{70} fullerene, g) amorphous carbon, and h) single-walled carbon nanotube.

films, thicker than 50 nm were deposited on monocrystalline n-Si prepared by arc-evaporation technique using pure graphite. For the first time, a photovoltage of about 280 mV and a photocurrent of 10 mA (under an illumination corresponding to Air Mass 1) was recorded using carbon instead of silicon. After this first work, the research of C/Si heterojunctions has risen steadily with the development of materials processing technology. In 1990, Fang *et. al.* [14] observed that the a-C film formed a natural anti-reflection coating and the heterojunction exhibited a Schottky-type structure. In the same year, Amaratunga *et. al.* carried out an independent study on C/Si heterojunctions, depositing ca. 50-100 nm-thick carbon films containing polycrystalline diamond grains onto the n-Si substrates by radio-frequency plasma-enhanced chemical vapor deposition (RF-PECVD) using a CH_4/Ar gas mixture. With an average bandgap of 2.0 eV, this carbon film was considered to possess semiconductor properties and a rectifying diode behaviour of the C/Si heterojunction was observed. Inspite

of these convincing reports on the PV effect of a-C/Si heterojunction, the first demonstration of a-C/Si solar cells was reported by Yu *et al.* in 1996 [16] using a 40 nm-thick carbonaceous thin film with a bandgap of 0.25 eV, deposited on the n-Si by chemical vapor deposition (CVD). The solar cells displayed a perfect rectifying current-voltage characteristic in the dark and generated a PCE of 3.8% with a J_{SC} of 2.73 mA cm^{-2} and a V_{OC} of 325 mV. This study also proved that this a-C/Si diode current came from the diffusion current, and it implied that this thin homogeneous a-C film by a low-temperature process could provide a nearly flawless interface with few defects for the C/Si heterojunction with a low recombination current caused by carrier scattering and carrier trapping. Although much effort has been devoted to improving the fabrication techniques of C/Si heterojunction PV cells and adjusting the bandgap of a-C, the development of a-C/Si heterojunction PV cells have been slowed by the high density of defects, difficulties of controlling the sp^2 /sp^3 ratio of the a-C, and inhomogeneity of dopants [17–19].

C_{60}/Si PV heterojunctions Fullerene face-centered-cubic structure was found to exhibit n-type semiconductor behaviour with a direct bandgap of 1.4-2.3 eV, which is an optimal value for PV applications [20–22]. In 1994, the first attempt to fabricate a C_{60}/Si heterojunction have been done by Chen *et al.* [23] by evaporating C_{60} powders onto the Si substrate, demonstrating that the C_{60}/p-Si heterojunctions exhibited rectifying properties in the dark.

In the same year, Wen *et al.* [24] demonstrated that a photovoltage of 0.2 V in a C_{60}/p-Si heterojunction could be generated. Due to the high resistance of the intrinsic C_{60}, controlling the thin film conductivity was necessary for PV applications. Fu *et al.* [25] demonstrated that the sheet resistance could be decreased by suitable ions implantation which would induce amorphization: n-type C_{60} could be obtained by phosphorus implantation while doping the film with aluminium during the deposition would lead to p-type C_{60}. The doped C_{60}/Si heterojunction exhibited rectification characteristics and an improved PV effect. Although many techniques were adopted, the PCEs of C_{60}/Si heterojunction solar cells were still low because of the big limiting factor of the low intrinsic conductivity. For further applications in solar cells, C_{60} and its derivatives would be used as additives with other organic/inorganic active materials for better solar spectrum conversion and charge transfer [26, 27].

Graphene/Silicon solar cells Graphene (Gr) has been attracting a growing interest in nanotechnology thanks to its relevant electrical and optical properties, such as an extraordinary electron mobility of $2.5 \cdot 10^5\ cm^2\ V^1 S^1$, which means that, at room temperature, electrons can move for several micrometers without scattering. On the other hand, graphene has a quasi-zero bandgap and its absorbance spectrum is dominated by intra-band transitions [29]. The possibility of depositing large area, clean, graphene monolayer, along with its outstanding strength and flexibility, make graphene particularly suitable for optoelectronic devices. Thanks to the previous research on the carbon/Si het-

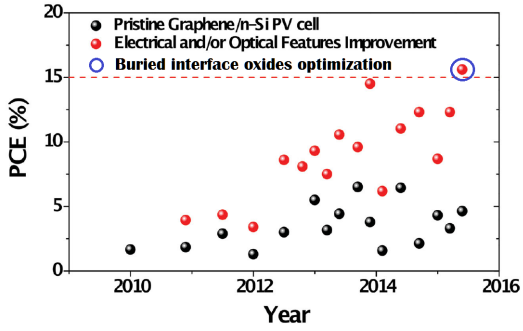

Figure 1.10: Evolution and selected representative results of the PCEs of laboratory graphene/Si solar cells. The pristine solar cells PCE values are represented in black while the electrical and optical improved ones are displayed in red. With the blue circle, the record PCE, obtained with interface oxide optimization, is highlighted. Adapted from Ref. [28].

erojunction, the development of graphene/Si solar cells was very fast. Graphene film could be transferred on Si, to form Schottky junctions, with a relatively large built-in field for charge-carrier separation. In these devices, graphene served not only as a transparent electrode but also as an active layer for electron-hole separation and hole transport.

To enhance the performance of the solar cell, the work function and the number of graphene layer need to be adjusted are in such a way that the built-in field can equal the work-function difference between graphene and silicon. By enlarging the work function of graphene, a stronger electric field is formed, improving the junction capability to collect photogenerated carriers. On the other hand,

the number of graphene monolayers would determine the film transmittance and sheet resistance of graphene, thus affecting the performance of the solar cell. Hence, taking direct inspiration from what already proved for CNTs/Si solar cells (see section 1.3), many attempt have been made to improve electrical and optical features of the Gr/Si heterojunctions, resulting in a PCE increase from 1.65% [30] to 15.6% [31] in 5 years (Figure 1.10).

The first strategy adopted was to p-dope graphene, by using oxidizing acids [32], by spin casting a polymer layer on graphene [33], or by gold nanoparticle functionalizzation [34], in order to reduce the sheet resistance, to modify the work function and to increase the carrier density and the built-in potential (red dots in Fig. 1.10).

However, the best result in term of PCE had been reached recently by Song *et al.* [31] who systematically investigated the role of the native silicon oxide layer in the Schottky barrier between graphene and Si. Each silicon substrate was first etched using hydrofluoric acid (HF) to remove native oxides and then left in air for varying amounts of time to allow the oxide to regrow. Finally a graphene sheet was transferred on top. The thickness of interfacial layer increased from 0.5 nm immediately after HF treatment to 1.5 nm after 2 weeks in air, as measured by ellipsometry. The junction behaviour changes with the oxide, in particular, under illumination the holes in excess inside the heterojunction should either tunnel through the barrier or recombine with electrons. In absence of the oxide layer, or with a very thin one, the low number of photoexcited carriers lead to a small recombination, but also the tunnelling across the junction is negligible. As the thickness of the native layer increases, further excess holes would accumulate near the interface of graphene/ Si and therefore recombination of carriers took place. The total photocurrent was determined by a balance between tunneling and recombination. Thus, the recombination would dominate over tunnelling under the thicker native silicon oxide layer in graphene/Si, resulting in reduced fill factor of solar cell. However, the V_{oc} increases from 0.45 V to 0.59 V with the 1.5 nm thickness of the oxide layer. Further chemical doping by Au nanoparticles and an anti-reflective coating results in the record PCE of 15.6%, with J_{sc} of 36.7 mA·cm^{-2} , V_{oc} of 0.595 V, and FF of 72%.

1.3 Carbon nanotubes in PV devices

In the recent years, CNTs have been widely used in organic photovoltaic devices (OPV). The following subsections will be dedicated to discuss how CNTs are able to play differen roles in the photovoltaic, i. e. part of the photoactive layer, transparent electrode or in dye-sensitized solar cells.

1.3.1 CNTs in photoactive layer

In 2001, E. Kymakisa and G. A. J. Amaratunga [35] used poly(3-octylthiophene) (P3OT) as the photoexcited electron donors, blended with single walled carbon nanotubes, which acted as the electron acceptors. The single wall nanotubes SWCNTs also allow the transferred electrons to be transported by providing percolation paths. Diodes were fabricated in the sandwich configuration shown

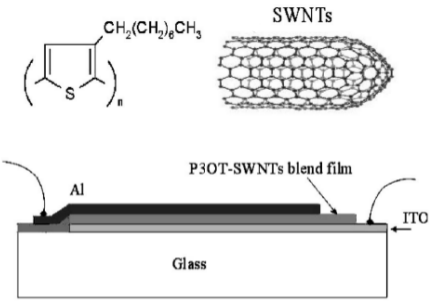

Figure 1.11: Chemical structures of P3OT and SWCNT and the architecture of the photovoltaic setup.

in Fig. 1.11. Organic films were deposited by drop and spin coating from a chloroform solution onto a glass substrate coated with indium-tin oxide (ITO) and aluminum electrodes were thermally evaporated. Enhancements of more than two orders of magnitude have been observed in the photocurrent from adding SWCNTs to the P3OT matrix (Fig.1.12). Improvements were speculated to be due to charge separation at polymer-SWCNT connections and to a more efficient electron transport through the SWCNTs. However, a rather low power conversion efficiency of 0.04% under 100 mW/cm^2 white illumination was

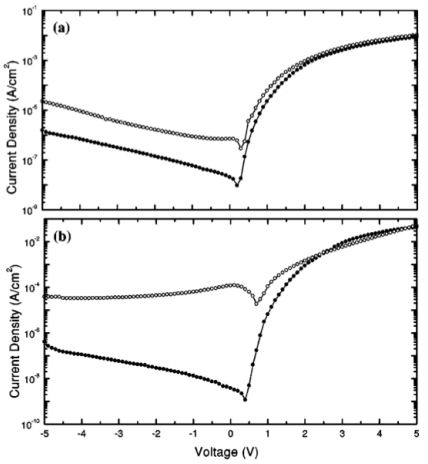

Figure 1.12: (a) IV characteristics of an ITO/P3OT/Al device (in dark filled circles) and under illumination (open circles). (b) The same data for an ITO/P3OT-SWCNTs/Al device.

observed for the device, suggesting incomplete exciton dissociation at low CNT concentrations. Because the lengths of the SWCNTs were similar to the thickness of photovoltaic films, introducing a higher percentage of SWCNTs into the polymer matrix was believed to cause short circuits.

To supply additional dissociation sites, other researchers [36] have physically blended functionalized MWCNTs into poly(3-hexylthiophene) (P3HT) polymer to create a P3HT-MWCNT with C_{60} double-layered device. However, the power efficiency was still relatively low at 0.01% under 100 mW/cm^2 white illumination. Weak exciton diffusion toward the donor-acceptor interface in the bilayer structure may have been the cause, along with the fullerene C_{60} layer possibly experiencing poor electron transport. More recently, a polymer photovoltaic device from C_{60}-modified SWCNTs (Fig.1.13) and P3HT has been fabricated. Microwave irradiating a mixture of aqueous SWCNT solution and C_{60} solution in toluene was the first step in making these polymer-SWCNT composites. Conjugated polymer P3HT was then added resulting in a power conversion efficiency

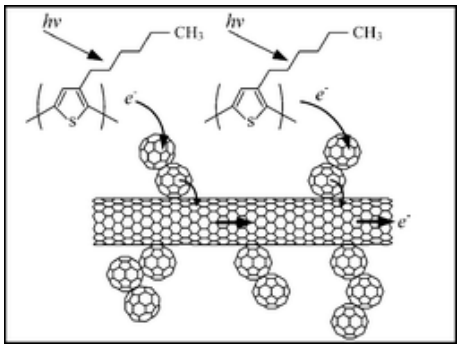

Figure 1.13: C_{60}-modified SWCNTs.

of 0.57% under simulated solar irradiation (95 mW/cm^2). It was concluded that improved short circuit current density was a direct result of the addition of SWCNTs into the composite, causing faster electron transport via the network of SWCNTs. It was also concluded that the morphology change led to a greater fill factor. Overall, the main improvement after the SWCNTs addition was on the power conversion efficiency (PCE); however, further optimization was thought to be possible. Additionally, it has been found that heating to the point beyond the glass transition temperature of either P3OT or P3HT after construction can be beneficial for manipulating the phase separation of the blend. This heating also affects the ordering of the polymeric chains, improving the transfer, the transport, and the collection of charges throughout the OPV device. The hole mobility and power efficiency of the polymer-CNT device also increased significantly as a result of this ordering [37]. Emerging as another valuable approach for deposition, the use of tetraoctylammonium bromide (TOABr) in tetrahydrofuran (THF) has also been the subject of investigation, exposing SWCNTs to an electrophoretic field. Photoconversion efficiencies of 1.5% and 1.3% were achieved when SWCNTs were deposited in combination with light harvesting cadmium sulfide (CdS) quantum dots (Fig.1.14) and porphyrins, respectively [38]. However, even though CNTs have shown potential in the photoactive layer, they have not resulted in a solar cell with a power conversion efficiency greater than the best tandem organic cells (6.5% efficiency [39]). But,

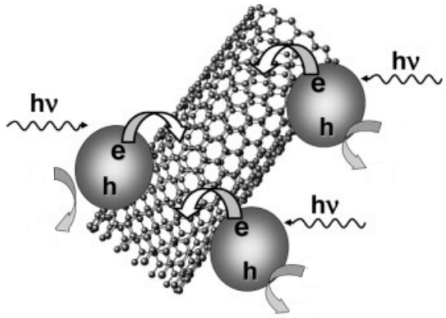

Figure 1.14: Charge-transfer interaction between photoexcited CdS nanoparticles and SWCNTs.

it has been shown in most of the previous investigations that the control over a uniform blending of the electron donating conjugated polymer and the electron accepting CNT is one of the most difficult as well as crucial aspects in creating efficient photocurrent collection in CNT-based OPV devices. Therefore, using CNTs in the photoactive layer of OPV devices is still in the initial research stages and there is still room for novel methods to better take advantage of the beneficial properties of CNTs.

1.3.2 Carbon nanotubes as transparent electrode

ITO is currently the most popular material used for the transparent electrodes in OPV devices, even if, howevere, it present a number of drawbacks. Firstly, ITO is not very compatible with polymeric substrates due to its high deposition temperature of around 600 °C. Traditional ITO also has unfavourable mechanical properties such as being relatively fragile. In addition, the combination of costly layer deposition in vacuum and a limited supply of indium results in expensive high quality ITO transparent electrodes. Therefore, developing and commercializing a replacement for ITO is a major focus of OPV research and development.

Conductive CNT coatings have recently become a prospective substitute based on wide range of methods including spraying, spin coating, casting, layer-

by-layer, and Langmuir-Blodgett deposition. The transfer from a filter membrane to the transparent support using a solvent or in the form of an adhesive film is another method for attaining flexible and optically transparent CNT films. Furthermore, the work function of SWCNT networks is in the 4.8 to 4.9 eV range (compared to ITO which has a lower work function of 4.7 eV) leading to the expectation that the SWCNT work function should be high enough to assure efficient hole collection.

Another benefit is that SWCNT films exhibit a high optical transparency in a broad spectral range from the UV-visible to the near-infrared range. Only a few materials retain reasonable transparency in the infrared spectrum while maintaining transparency in the visible part of the spectrum as well as acceptable overall electrical conductivity.

SWCNT films are highly flexible, do not creep, do not crack after bending, theoretically have high thermal conductivities to tolerate heat dissipation, and display a high radiation resistance. However, the electrical sheet resistance of ITO is an order of magnitude less than the sheet resistance measured for SWCNT films.

Nonetheless, initial research studies demonstrate SWCNT thin films can be used as conducting, transparent electrodes for hole collection in OPV devices with efficiencies between 1% and 2.5% confirming that they are comparable to devices fabricated using ITO [40]. Thus, possibilities exist for advancing this

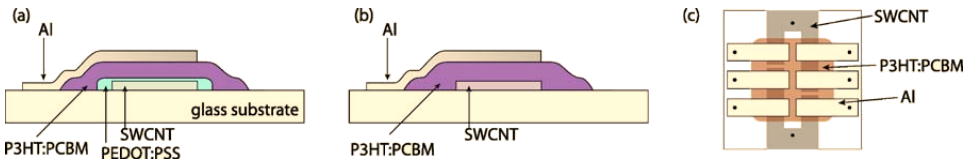

Figure 1.15: (a) Device A in which ITO is replaced by the SWCNT layer but PEDOT:PSS remains.(b) Device B in which both PEDOT:PSS and ITO are replaced by the SWCNT layer. (c) Top view of the device structure. Six devices are created on glass slide.

research to develop CNT-based transparent electrodes that exceed the performance of traditional ITO materials.

1.3.3 CNTs in dye-sensitized solar cells

Due to the simple fabrication process, low production cost, and high efficiency, large expectations have so far been shown in dye-sensitized solar cells (DSSCs). Thus, improving DSSC efficiency has been the subject of a variety of research investigations because it has the potential to be manufactured economically enough to compete with other solar cell technologies. Titanium dioxide nanoparticles have been widely used as a working electrode for DSSCs because they provide a high efficiency, more than any other metal oxide semiconductor investigated.

Yet the highest conversion efficiency under AM 1.5 irradiation, reported for this device, is about 11%. Despite this initial success, the effort to further enhance efficiency has not produced any major result.

The transport of electrons across the particle network has been a key problem in achieving higher photoconversion efficiency in nanostructured electrodes. Because electrons encounter many grain boundaries during the transit and experience a random path, the probability of their recombination with oxidized sensitizer is increased. Therefore, it is not adequate to enlarge the oxide electrode surface area to increase efficiency because photo-generated charge recombination should be prevented.

Promoting electron transfer through film electrodes and blocking interface states lying below the edge of the conduction band are some of the non-CNT based strategies to enhance efficiency that have been employed. With recent progress in CNT development and fabrication, there is promise to use various CNT based nanocomposites and nanostructures to direct the flow of photogenerated electrons and assist in charge injection and extraction. To assist the electron transport to the collecting electrode surface in a DSSC, a popular concept is to utilize CNT networks as support to anchor light harvesting semiconductor particles.

Research efforts along these lines include decorating SWCNTs with CdS quantum dots on SWCNTs [38]. Charge injection from excited CdS into SWCNTs was documented upon excitation of CdS nanoparticles. Other varieties of semiconductor particles including CdSe and CdTe can induce charge-transfer processes under visible light irradiation when attached to CNTs. Including porphyrin and fullerene, assembling of photoactive donor polymer and acceptor fullerene on electrode surfaces has also been shown to offer considerable improve-

ment in the photoconversion efficiency of solar cells [41]. Therefore, there is an

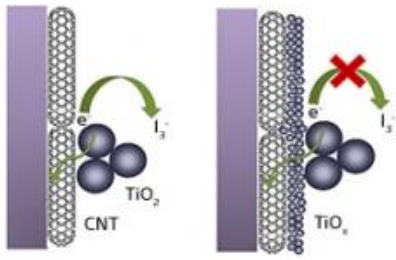

Figure 1.16: In earlier designs (left), CNTs degraded through chemical processes. Using a thin protective layer of titanium oxide stabilizes the nanotubes (right), increasing the performance of these cells [42].

opportunity to facilitate electron transport and increase the photoconversion efficiency of DSSCs utilizing the electron-accepting ability of semiconducting SWCNTs.

Because pristine MWCNTs have a hydrophobic surface and poor dispersion stability, pretreatment was necessary for this application. A relatively non-destruction method for removing impurities, H_2O_2 treatment was used to generate carboxylic acid groups by oxidation of MWCNTs.

Another positive aspect was the fact that the reaction gases including CO_2 and H_2O were non-toxic and could be released safely during the oxidation process. As a result of treatment, H_2O_2 exposed MWCNTs have a hydrophilic surface and the carboxylic acid groups on the surface have polar covalent bonding. Also, the negatively charged surface of the MWCNTs improved the stability of dispersion. By coating the MWCNTs with titanium dioxide nanoparticles using the sol-gel method, an increase in the conversion efficiency of about 50% compared to a conventional titanium dioxide cell was achieved. The enhanced interconnectivity between the titanium dioxide particles and the MWCNTs in the porous titanium dioxide film was concluded to be the cause of the improvement in short circuit current density. Here again, the addition of MWCNTs was thought to provide more efficient electron transfer through film in the DSSC.

1.4 CNTs/Silicon solar cells

As seen so far, the role of carbon nanotubes in organic solar cell applications was mainly confined as nanoscale fillers (providing transport path) in polymer matrix or as transparent electrodes for collecting charge carriers. It was believed that the high aspect ratios and large surface area of nanotubes could be beneficial to exciton dissociation and charge carrier transport, improving the power conversion efficiency. However, all these cells have shown negligible efficiency ($\simeq$0.1%), even with the addition of dye.

The nanotubes dispersion in polymers, the separation of semiconducting tubes from metallic species plus the very low hole mobilities of polymers, all represent limiting factors to the device fabrication and performance. In addition, nanotube films (by spin-cast or direct growth) used as transparent electrodes have shown negligible efficiency improvement, if compared with ITO glass.

In the studies so far presented, nanotubes do not participate in photogeneration process. Actually, the conjugated polymers (e.g., P3HT or P3OT) are the component that produce excitons under optical excitation. Nanotubes, when embedded into the polymer matrix, only to provide more interfacial area for exciton dissociation and charge transport path.

Nonetheless, the response of individual nanotube, as well as of CNTs films, to the impinging light has been studied and experiments have shown that SWCNT networks are able to generate a photocurrent with peaks in correspondence of the S_{11} and S_{22} transitions [43] and that photoexcitation across pairs of van Hove peaks enhances the conductivity of individual semiconductor nanotubes. Later, Mohite *et al.* [44] reported the observation of the M_{11} transition in the photocurrent energy spectrum, evidencing that also metallic nanotubes contribute to photocurrent, thus allowing the extension of the spectral response of these nanostructures toward the visible region.

In addition, it has been recently suggested that the standard limit of photovoltaic efficiency, first established by Shockley and Queisser in 1961 [45], setting the conversion of a single photon into electron-hole (e-h) pair, can be overcome for carbon nanotubes. In fact, efficient multiple exciton generation (MEG) in carbon nanotubes upon single photon absorption has been shown to occur in (6,5) SWCNTs under 335 nm and 400 nm excitation through pure optical pump and probe experiments [46] and in individual SWCNT based photodiodes. On

the other hand, solar cells need to be efficient not only in e-h pair generation but also in the subsequent carrier separation and transport. Intrinsically carbon nanotubes have very high electrical conductivity of approximately 10^6 S/cm at room temperature [47], a value well above that of metals, such as copper, at room temperature.

In SWCNT films, conductivity origins from the carrier transport along the cylindrical sidewall and the carrier hopping from one tube to another and can be interpreted in the percolation theory framework. So, in principle, conductivity should increase with nanotube density. However, this is not the only parameter to take into account when the electrical performances of a carbon nanotube film are considered. As a matter of facts, the presence in the 2D or 3D random network of both semiconducting and metallic nanotubes (forming several metal-metal, semiconductor-semiconductor and metal-semiconductor junctions) as well as the tube sensitivity to chemical doping play fundamental roles and make the transport mechanism very complex to understand. In particular, the tunnelling barrier at the junction of two semiconducting and, at a lower extent, of two metallic tubes has been reported to favour the charge carrier percolation, thus suggesting that to increase the electrical conductivity it is necessary to fabricate SWCNT films with a high percentage of semiconducting (or metallic) nanotubes. Therefore, getting a highly conductive SWCNT network necessarily requires a chirality sorting process since, naturally, SWCNTs are characterized by many chiralities. Moreover, structural defects and SWCNT tendency to self-assemble in bundles are other limiting factors of the nanotube and CNT network conductivity. As far as e-h pair separation regards, ideal structurally perfect SWCNTs possess no junction where excitons can be splitted. On the other side, it is well known that real nanotubes can present structural defects, kinks, twisting and bending or are organized in networks where two or more CNTs intersect so giving rise to local unconventional p-n or Schottky junctions [48] which may act as exciton splitters. Nonetheless, it has been demonstrated that, for carbon nanotube networks, either self-standing or deposited on an insulating substrate (e.g., glass,), the driving force of the e-h pair separation are the Schottky barriers.

Among the variety of CNT combinations reported in literature, the carbon nanotube/Si heterojunction represents a good tool to further investigate nanotube network behaviour upon light illumination, due to the wide knowledge of

the silicon properties. Besides, carbon nanotube/Si heterojunction solar cells are the most promising in terms of the power conversion efficiency currently obtained on small research cells which, when addressed the scaling-up problem, could lead to reduced fabrication costs with respect to the conventional silicon technology.

Starting from 2007, J. Wei *et al.* [49] have demonstrated that macrosize bundles consisting of double-walled nanotubes (DWNTs) could generate photocurrent at an energy conversion efficiency of up to 0.5% under illumination of light in the visible region. For the first time, they directly use DWNTs as the energy conversion material to construct thin-film solar cells, without using polymers. The DWNTs [50] serve as photogeneration sites as well as a transport path for charge carriers (holes), while a n-type silicon wafer was used to extract electrons (Fig.1.17(a)).

Here, the DWNT film was involved in three key processes for energy conversion. First, the DWNTs form a junction interface with Si that is responsible for charge separation. The band gap of semiconducting DWNTs (2-3 nm in diameter) is estimated to be less than 0.5 eV, according to the energy gap equation (see eqn. 1.5) for CNTs. The band diagram in Fig. 1.17(b) shows a large built-in voltage of 0.64 V. Charge separation could occur at this built-in field, where electrons are directed to the n-type Si region and holes are transported through the DWNTs (Fig. 1.17(c)).

The DWNTs then form a percolated network that is favourable for fast charge (hole) transport (Fig. 1.17(d)). The DWNT film also serves as a transparent electrode for light illumination and charge collection. While most of work has primarily focused on single-walled or multiwalled nanotubes, DWNTs have been seldom introduced to solar cells even though they have advantages such as possessing similar diameter with single-walled tubes but with higher stability. Initial tests have shown a power conversion efficiency of >1%, ascribable to the photoconductivity and high mobility of nanotubes.

Figure 1.18 shows an I-V characteristics of a typical DWNT/n-Si solar cell, in which the DWNT film is about 50 nm in thickness, in dark and under standard white light illumination. The device shows an evident p-n junction behaviour in the dark, where the reversed current density is very low (over 500 times lower than the forward current density) when the bias voltage sweeps from -2.0 to 0 V compared to forward current ($\sim$16 mA/cm^2 at 1.0 V). Under illumination,

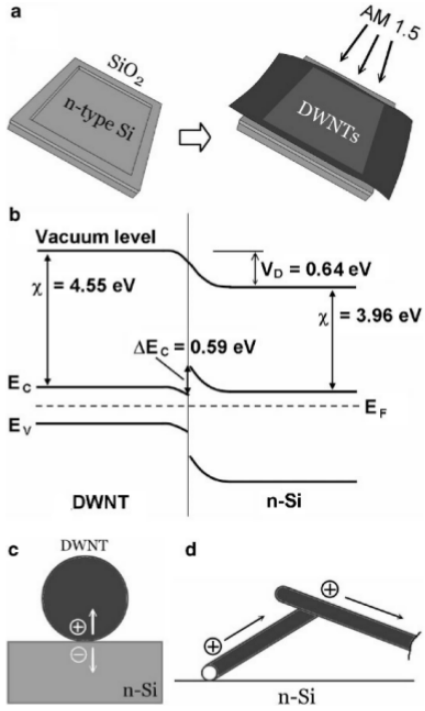

Figure 1.17: (a) Illustration of coating a patterned Si/SiO_2 substrate with a DWNT film in cell fabrication. The DWNT film serves as a transparent electrode for light illumination (AM 1.5) and charge collection. (b) Band scheme diagram of the DWNT-Si heterojunction. (c) Illustration of the charge separation occurred at the interface between a DWNT and the Si substrate. (d) Illustration of charge transport through a percolated DWNT network.

the I-V curve shifts downward, with an open-circuit voltage V_{oc} of $0.5V$ and short-circuit current density J_{sc} of about 13.8 mA/cm^2.

The fill factor (FF) and power efficiency (η) of the DWNT/n-Si solar cell are about 19% and 1.38%, respectively. Compared with previous solar cell configurations based on conjugated polymers mixed with SWCNTs or DWCNTs, with a FF of 15-30% and $\eta \ll 1\%$, these devices show a comparable fill factor

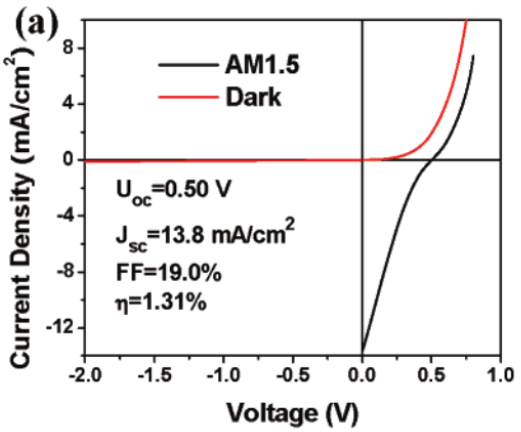

Figure 1.18: Current-voltage plot of a DWNT/n-Si device in dark and under illumination, showing typical solar cell performance with efficiency of 1.3%.

but much higher efficiency.

Furthermore, it was found that the photoinduced current is very weak (<1 μ A/cm^2) when solar light irradiates only DWNT films without the presence of n-Si substrate, indicating that a significant value of V_{oc} and J_{sc} of the DWNT solar cells originates from the creation of heterojunctions at the interface between the DWNT film and the n-Si. Although having similar diameter to SWCNTs, which usually behave as p-type semiconductors, the DWCNTs have shown ambipolar (both p- and n-type) conducting behaviour, due to smaller band gaps.

Oxide-free Si surfaces were found to assist in the formation of more efficient heterojunctions with DWNTs. The Si substrate was therefore dipped into diluted hydrofluoride acid to remove the native oxide layer prior to DWNT transfer.

The current density versus voltage (JV) 1.19 curve of one of the devices shows an open-circuit voltage V_{oc} of 0.54 V, a shortcircuit current density J_{sc} of 26 mA/cm^2, a fill factor FF of 53%, and a power-conversion efficiency η of 7.4%, showing the fundamental role played by silicon oxidation in the cell behaviour. Starting from these first works, a large number of papers appeared reporting

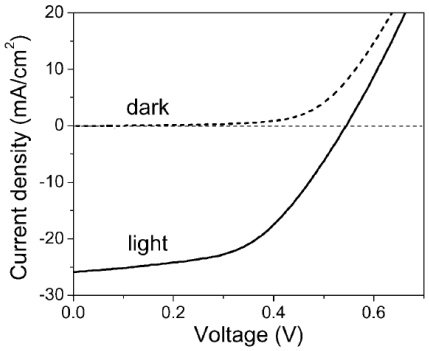

Figure 1.19: Dark and light JV curves of a heterojunction cell.

improvements to the CNT/Si solar cell, enhancing PCEs, up to the current maximum value of 15% [52]. Nevertheless, the characteristics and the behaviour of such devices, have been not fully understood and deserve more studies. Up to now, several factors, strictly connected to the physical properties of the materials involved, have been evidenced to contribute to the cell performances.

As in conventional silicon solar cells, in order to achieve the maximum efficiency, it is necessary to minimize the series resistance (R_s) and to maximize the shunt resistance (R_{sh}). The CNT network thickness and density are mainly affecting its R_{sh}. However, since a nanotube network is a porous structure made of randomly distributed small bundles or single CNTs, it is hard to define its thickness. In order to circumvent this difficulty, optical transmission has been widely used in order to estimate the thickness, averaging on the morphological inhomogeneities.

This permits to correlate optical transmittance (T) of the CNT network and its R_{sh} value [53, 54], showing that R_{sh} decreases with T, i.e., the denser and thicker is the nanotube network, the lower is its sheet resistance. Thus, one should expect that the lowest T network presents the highest power conversion efficiency. On the contrary, Wei et al. [50] reported that J_{SC} and PCE have their maximum values in correspondence of an intermediate optical transparency. This finding was subsequently confirmed in other papers even for SWCNTs and MWCNTs [53–56] and can be interpreted as following. A reduction of the film

transparency can be associated to an increase of i) the density of CNTs on the silicon surface and ii) of the average thickness of the overall network. The increase of the total area covered by CNTs on the Si surface could enhance the charge carrier transport towards the surface electrodes (giving rise to R_{sh} reduction) and implies that a higher number of CNT/Si junctions are available for the separation of the photogenerated e-h pairs. However, for thicker films, the topmost CNT bundles are not in direct contact with the Si substrate to form junctions. Therefore, they do not contribute to photocurrent generation and, at the same time, they absorb light thus preventing radiation from reaching the silicon substrate (where most of the e-h pairs are generated).

Chapter 2

Experimental Techniques and Samples Preparation

2.1 X-rays photoelectron spectroscopy (XPS)

X-ray photoelectron spectroscopy (XPS) is an experimental technique based on the photoelectric effect. This effect was firstly observed by H. R. Hertz in 1891, but only Einstein in 1905 [57] was able to give a theoretical explanation of the phenomenon. Two years after Einstein's publication, in 1907, P.D. Innes experimented with a Roentgen tube, Helmholtz coils, a magnetic electron kinetic energy analyzer and photographic plates, to record broad bands of emitted electrons as a function of velocity, in effect recording the first XPS spectrum. Other researchers, including Henry Moseley, Rawlinson and Robinson, independently performed various experiments to sort out the details in the broad bands. World Wars I and II halted research on XPS. After WWII, Kai Siegbahn and his research group in Uppsala (Sweden) developed several significant improvements in the equipment, and in 1954 recorded the first high-energy-resolution XPS spectrum of cleaved sodium chloride (NaCl), revealing the potential of XPS. A few years later in 1967, Siegbahn published a comprehensive study of XPS, bringing instant recognition of the utility of XPS, which he referred to as ESCA (Electron Spectroscopy for Chemical Analysis). In cooperation with

Siegbahn, a small group of engineers (Mike Kelly, Charles Bryson, Lavier Faye, Robert Chaney) at Hewlett-Packard in the USA, produced the first commercial monochromatic XPS instrument in 1969. Siegbahn received the Nobel Prize for Physics in 1981, to acknowledge his extensive efforts to develop XPS into a useful analytical tool.

In parallel with Siegbahn's work, David Turner at Imperial College (and later at Oxford University) in the UK developed ultraviolet photoelectron spectroscopy (UPS) on molecular species using helium lamps

In the photoelectric effect, electrons are emitted from matter (metals and non-metallic solids, liquids or gases) as a consequence of their absorption of energy from electromagnetic radiation of short wavelength and high frequency, such as visible or ultraviolet radiation (Fig. 2.1). Electrons emitted in this manner may be referred to as photoelectrons. This process must preserve the

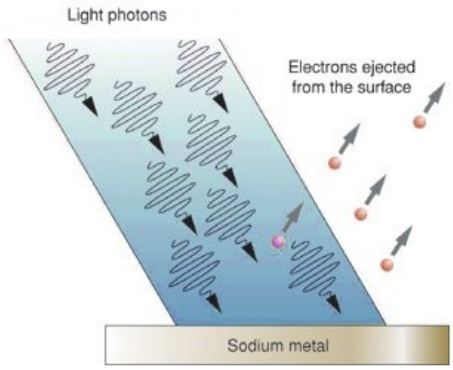

Figure 2.1: Schematic representation of the photoelectric effect: when sufficient energy is absorbed from an incident photon electrons can be ejected from a solid.

total energy so, the absorption of a photon with an energy $\hbar\omega$ by an electron in an energy level E_B, provides a kinetic energy E_k to the electron, subtracted by the work function of the material Φ.

$$E_k = \hbar\omega - \Phi - E_B \tag{2.1}$$

The basic mechanism behind an XPS instrument is illustrated in Fig. 2.2.

Photons of a specific energy are used to excite the electronic states of atoms. Electrons ejected from the surface are energy filtered via a hemispherical analyzer (HSA) before the intensity, for a defined energy is recorded by a detector. Since electronic core levels in atoms are quantized, the resulting energy spectra exhibit resonance peaks, characteristic of the electronic structure for atoms at the sample surface.

While the x-rays may penetrate deep into the sample, the escape depth of the ejected electrons is limited. That is, for energies around 1400 eV, ejected electrons from depths greater than 10 nm have a low probability of leaving the surface without undergoing an energy loss event, and therefore contribute to the background signal rather than well defined primary photoelectric peaks. In order to mantain a well defined potential during all the acquisition process,

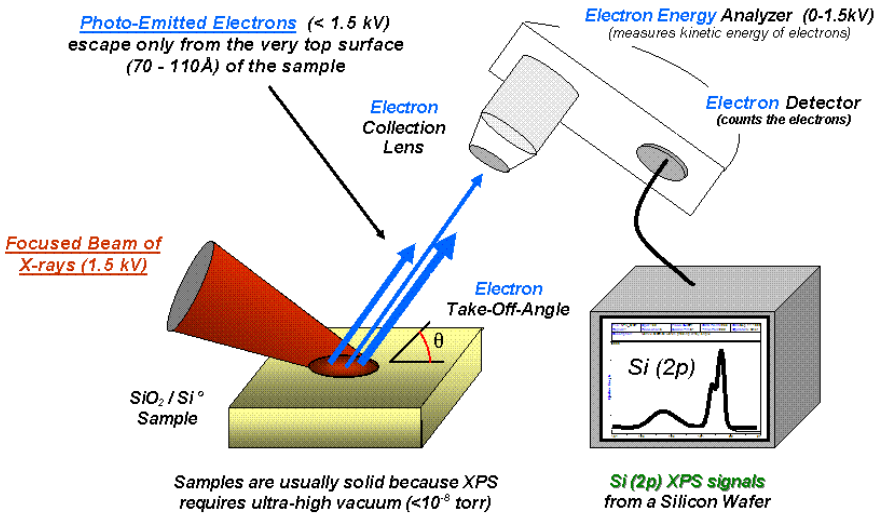

Figure 2.2: A typical XPS setup.

sample and spectrometer are put in electric contact. A schematic representation of the energy levels and kinetic energies in an XPS process in shown in Fig. 2.3.

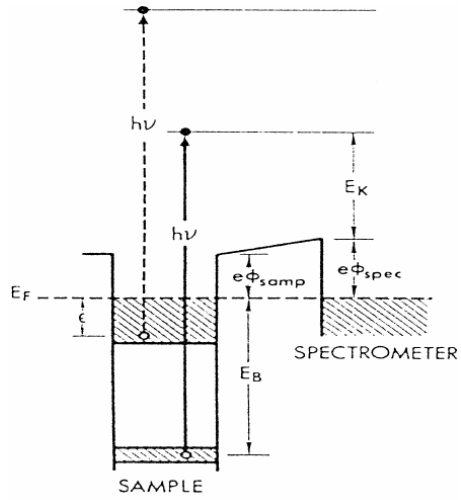

Figure 2.3: Energy level diagram for sample and spectrometer in a XPS experiment.

The thermodynamic equilibrium is reached only if sample and spectrometer have the same chemical potential. In this case their Fermi levels are aligned, leading to a misalignment of the vacuum levels which produces an accelerating or retarding potential $\Phi = \Phi_{sample} - \Phi_{spec}$ with the effect of modifying the kinetic energy.

$$E'_k = E_k + \Phi_{sample} - \Phi_{spec} \tag{2.2}$$

Knowing the work function, one can easily determinate the binding energy of the outcoming electron. The result of a photoemission experiment is an XPS spectrum which reports the emission intensity as a function of the kinetic energy of electrons reaching the analyzer (Fig. 2.4). In principle, the energies of the photoelectric lines are well defined in terms of the binding energy of the electronic states of atoms. Furthermore, the chemical environment of the atoms at the surface may yield characteristic energy shifts of the peak energies. The detected electron energies can be referred to the Fermi energy of the spectrometer, an absolute energy scale can be established, thus aiding the identification of species.

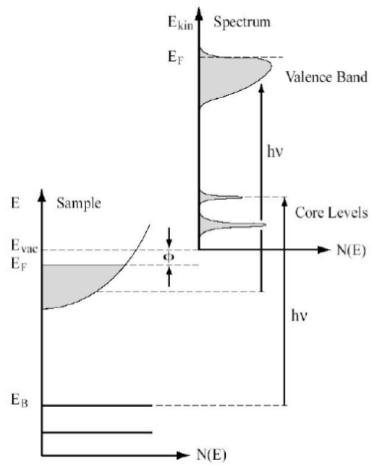

Figure 2.4: A comparison between the level scheme of a solid and its XPS spectrum.

In case of conducting samples it is easy to find the Fermi level, that at room temperature can be well approximated by the chemical potential and is the last occupied level. However, for non-conducting samples, insulators and semiconductors, finding the Fermi level is not an easy task because it lies in the energy gap between valence and conduction bands.

Here, the problem of energy calibration is significant. Electrons leaving the sample surface cause a potential difference between the sample and the spectrometer resulting in a retarding field acting on the electrons escaping the surface. Charge compensation, designed to replace the electrons emitted from the sample, is used to reduce the influence of sample charging on insulating materials, but nevertheless identification of chemical state based on peak positions requires careful analysis. In this case the Fermi energy can be found putting a metal in electric contact with the sample, for example, in our set up, the sample was fixed to the sample holder. Charge induced shifting is normally due to a modest excess of low voltage (-1 to -20 eV) electrons attached to the surface, or a modest shortage of electrons (+1 to +15 eV) within the top 1-12 nm of the sample caused by the loss of photo-emitted electrons. The degree of charging

depends on various factors. If, by chance, the charging of the surface is excessively positive, then the spectrum might appear as a series of rolling hills, not sharp peaks.

2.1.1 The three-step model for XPS

Photoemission can be described as a sequence of three events, independent of each other:

1. optical excitation of one electron in the bulk.
2. electron migration to the surface.
3. overcome of the potential barrier and emission of the electron in the vacuum state.

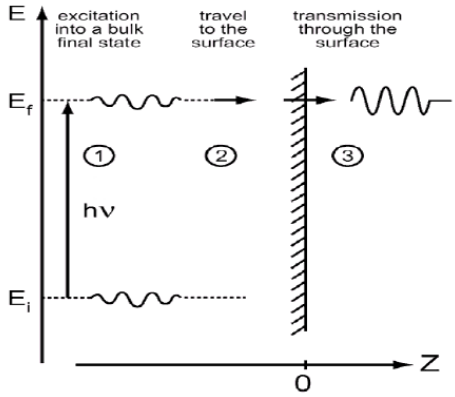

Figure 2.5: The three step model scheme for XPS.

The total photoemission intensity is then given by the product of three independent terms: the total probability of optical excitation in the bulk, which contains all the informations about the electronic structure of the material, the scattering probability of the excited electron by the atoms that constitute the solid, during its path to the surface, defined by the *mean free path*, and the

probability of transmission through the potential barrier of the surface, dependening on the energy of the electron and on the work function of the sample Φ_s [60].

2.1.2 Structure of an XPS spectrum

XPS is a quantitative technique in the sense that the number of electrons recorded for a given transition is proportional to the number of atoms at the surface. In practice, however, to achieve an accurate evaluation of atomic concentrations from XPS spectra is not straightforward. The precision of the intensities measured using XPS is not in doubt: intensities measured from similar samples are repeatable to good precision. What may be doubtful are results reporting to be atomic concentrations for the elements at the surface. An accuracy of 10% is typically quoted for routinely performed XPS atomic concentrations. For specific carefully performed and characterised measurements better accuracy is possible, but for quantification based on standard relative sensitivity factors, precision is achieved but not accuracy.

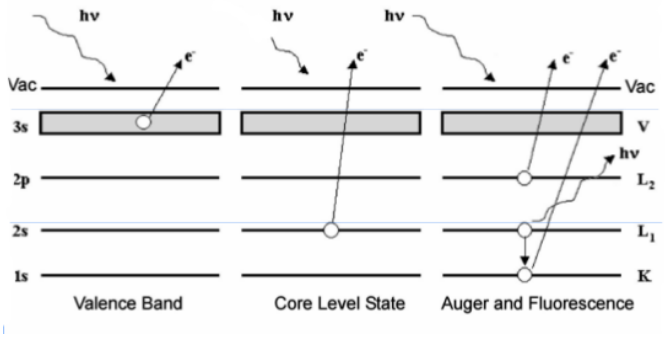

Figure 2.6: The three of the most important photoemission processes which can be detected in XPS.

A photoemission spectrum is composed of a multitude of peaks and structures of different origin and we shall now proceed to analyze them in detail [58, 59].

- **Core levels**

We define core levels all the photoemission peaks with energy greater than 20 eV, originated from photoelectrons that have not been inelastically scattered. These peaks are thus characteristic of the emitter element, being detected at the binding energy of the core level from which electrons are photoemitted. The signals originating from levels characterized by orbital quantum number $l > 0$ and a closed shell are *doublets*, two separate states for spin-orbit coupling effect, characterized by two different values of the total angular momentum quantum number $j = l \pm s$, where s is the spin quantum number. The energy separation ΔE_j of the doublet can range from less than one eV up to tens of eV (for Cu 2p, e.g., the energy separation is about 20 eV), depending on the spin-orbit coupling constant. ΔE_j increases with the atomic number Z, with constant n and l, and with the decrease of n, with a fixed l. Moreover, the relative intensity of the two components of the doublet is given by the ratio of the respective degeneracy:

$$R = \frac{2j_+ + 1}{2j_- + 1} \tag{2.3}$$

The line width of an XPS peak is generally the width at half height (FWHM, Full Width at Half Maximum), which is given by the overlap of three separate contributions:

$$\Delta E = \sqrt{\Delta E_c^2 + \Delta E_a^2 + \Delta E_{ph}^2} \tag{2.4}$$

where ΔE_c is the intrinsic width of the peak referred to the core level (related to the average lifetime of the excited state, due to the process of photoionization), ΔE_a is the resolution of the analyzer, which depends on the working conditions (fixed pass energy [1] or $\Delta E/E_0$) and ΔE_{ph} represents the relative width of the line of the exciting source of X-rays.

The chemical status of a given element slightly affects the spectrum, leading to shifts in energy of a few eV, giving origin to chemical shifts. For this reason, the XPS analysis allows to distinguish between different types of atoms, according to their oxidation state or their different role in a molecular bond. Atoms of

[1] Electrostatic fields within the hemispherical analyzer (HSA) are established to only allow electrons of a given energy (the so called Pass Energy PE) to arrive at the detector slits and onto the detectors themselves, the pass energy influences the energy resolution achieved within a spectrum.

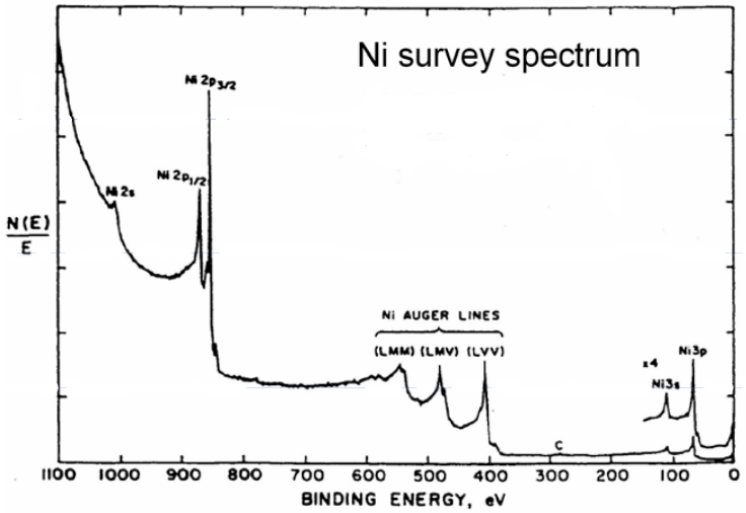

Figure 2.7: An example of XPS survey spectrum. Core levels appear at high BE (low KE), shallow core levels and valence band at low BE (high KE), while in the mid-range Auger lines are detectable.

the same chemical element but located in different chemical environments (e.g. different chemical bond), present photoemission peaks with binding energies that may differ from 1 to 10 eV from each other. This phenomenon is known as *chemical shift*. Two atoms can be not equivalent in many circumstances; the factor that weights more is the oxidation state, that is, the charge distribution in the neighborhood of a given atom. By measuring the chemical shift, it is thus possible to determine the type of the chemical bonding of the elements and the chemical group to which they belong.

- **Valence levels**

The valence levels are those occupied by electrons with binding energy less than $\sim 20eV$. In this range of energies, the spectrum consists of several peaks, very close to each other and difficult to resolve, the latter of which defines the Fermi level in the case of conductive materials. This set of peaks constitute the band structure of valence levels, whose relative intensities of photoemission peaks are

very small compared to the core levels, as at the photon energies typically used in the XPS probe (Al K_α or Mg K_α), the VB peaks cross section is usually lower than those of deep levels. To investigate in more detail the valence band, exciting sources with a lower energy are used, in order to work with the highest photoemission cross sections for valence levels; the most common technique for this case is the UPS analysis (Ultraviolet Photoelectron Spectroscopy).

- **Auger series**

When the photoionization process involves a deep level, the system acquires an extra energy, due to the presence of a core vacancy, and is left in a highly unstable state. The decay to the ground state can be achieved through two different channels, one radiative (X-ray fluorescence) and one non-radiative (*Auger emission*).

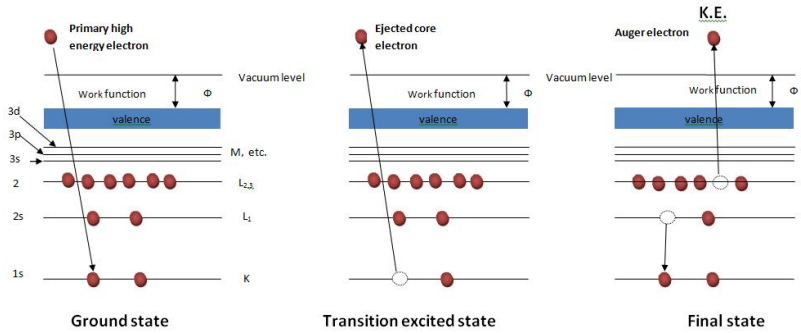

Figure 2.8: The Auger process.

The basic Auger process starts with the removal of an inner shell atomic electron to yield a vacancy. The electron can be removed from an atom A by an X-photon with energy $\hbar\omega$.

$$A + \hbar\omega \rightarrow A^+ + e^- \tag{2.5}$$

When a vacancy is created, an electron from a higher energy level (e.g. L_1) may fall into the core level (e.g.K) to fill the vacancy, releasing energy during this

process. This energy can be transferred to another electron (e.g. $L_{2,3}$), which is ejected from the atom. This second ejected electron is called Auger electron.

$$A^+ \rightarrow A^{2+} + e^- \tag{2.6}$$

The excess energy in this process is dissipated as kinetic energy E_{Aug} of this electron.

$$E_{Aug} = E_K - E_{L_1} - E_{L_{2,3}} \tag{2.7}$$

and does not depend on the energy of the exciting photon. Therefore, in an XPS spectrum, the characteristic Auger series always appear, because the Auger electrons are collected and analyzed just as the photoelectrons. However, these two contributions are easily distinguished by the fact that the energies of the Auger peaks depend only upon the electronic levels of the atom and are emitted at constant kinetic energy, irrespective of the photon energy [61].

- **Satellite and Ghost peaks**

Satellite lines are the result of the fact that conventional double-anode X-ray sources (Al and Mg) are not monocromatized, therefore, in addition to the classical Bremsstrahlung radiation and the characteristic line K_α, it is possible to have the generation of photoemission peaks which derive from anode electronic transitions that are less probable and less intense than the main line.

Otherwise, *ghost peaks* have a strictly instrumental origin, arising from any impurity present on the anode of the source, which in turn emits X-rays to an own energy. In Al/Mg dual sources mutual contamination can occur, resulting in the appearance of the characteristic line of the anode not in use. Finally, it is not uncommon that the aluminum window, used as a shield to protect the sample from electron bombardment, is itself a source of undesired Al K_α lines.

- ***Energy loss* peaks**

During its path in the solid, from the emitter atom to the surface, an electron with sufficient energy may lose part of its kinetic energy to excite collective modes of oscillation of the valence charge density, giving origin to *plasmons*. These appear as bands of reduced intensity and large width near the core peak, at higher binding energy. There are two different types of plasmons:

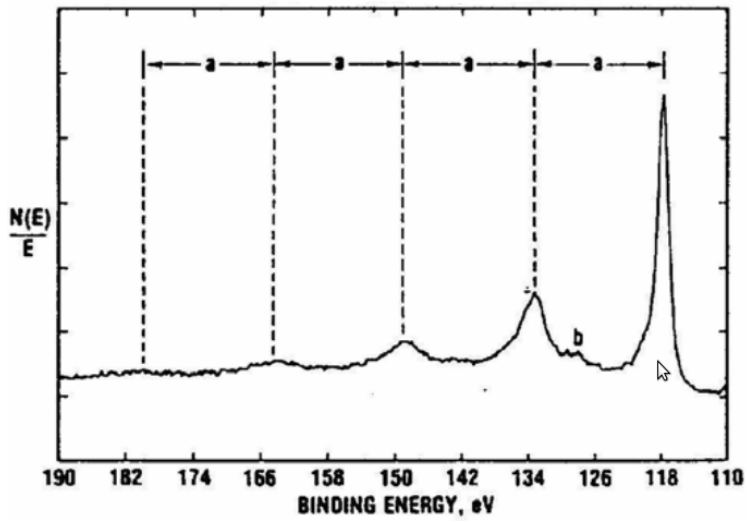

Figure 2.9: Energy loss (plasmon) lines associated with the 2s line of aluminum.

- *Bulk plasmons* are common in metallic materials where the conduction electrons constitute a Fermi gas. According to the Drude-Lorentz model, metals have a Plasma frequency given by

$$\omega_{P_b}^2 \simeq \frac{N_v e^2}{\varepsilon_0 m} \tag{2.8}$$

  where N_v is the density of valence electrons, m is the free electron mass and ε_0 is the dielectric constant.

- *Surface plasmons* constitute a plasma oscillation parallel to the surface of the sample, which decays exponentially in the normal direction. It can be shown in addition that the fundamental frequency of a surface plasmon ω_{P_s} is linked to the bulk plasmon one ω_{P_b} by the expression:

$$\omega_{P_s} \simeq \frac{\omega_{P_s}}{\sqrt{2}} \tag{2.9}$$

In both cases, the loss of energy during the electron-plasmon interaction is quantized by $\hbar\omega_{P_{b,s}}$, which yields a series of inelastic peaks at binding energies

$E_b + n\hbar\omega_{P_{b,s}}$, next to the main peak of binding energy E_b, where $n = 1$ is the fundamental frequency, while the following n are the higher harmonics, with decreasing intensity.

- **Background**

The first issue involved with quantifying XPS spectra is identifying those electrons belonging to a given transition. The standard approach is to define an approximation to the background signal. The background in XPS is non-trivial in nature and results from all those photoelectrons which may be involved in inelastic scattering process (i.e. energy losses). The zero-loss electrons constituting the photoelectric peak are considered to be the signal above the background. A variety of background algorithms are used to measure the peak area (Figure 2.10); none of the practical algorithms is perfect and therefore background subtraction represents a source for uncertainty when computing the peak area. Peak areas computed from the background subtracted data form the basis for most elemental quantification results from XPS.

2.1.3 Intensity of the XPS peaks

The quantitative interpretation of the X-ray photoemission peak intensity requires the development of a model, able to account for the characteristics of the X-ray source, the sample under consideration, the electron analyzer and the measuring system. In general, the intensity of a photoelectronic peak N_k, i.e. the number of counts registered by the detector per unit of time for a given energy range, which originated from a subshell of the k-th atom, can be calculated by integrating the differential intensity dN_k due to the various elements of volume of the sample under analysis. Referring to figure 2.11, we denote by x, y and z the positions within the sample, assuming that the phenomena of reflection and refraction, at the surface are negligible, i.e. $\phi_x = \phi'_x$ and $\vartheta = \vartheta'$. Assuming further that specimen is homogeneous, ideally flat and polycrystalline, it is possible to express the differential intensity dN_k as the product of the following contributions:

- the X-ray flux at x, y, z;
- the number of atoms or molecules;

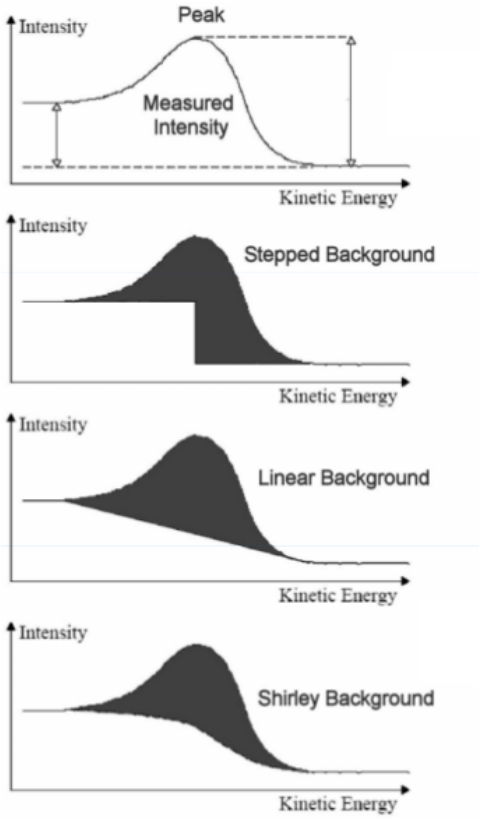

Figure 2.10: Most common background approximations for an XPS peak, starting from the simpler and inaccurate on top, to the most complex one at the bottom.

- the solid angle of acceptance of the electronic analyzer;
- the differential section for the subshell k;
- the fraction of electrons that reach the surface without energy loss;
- the efficiency of instrumental detection.

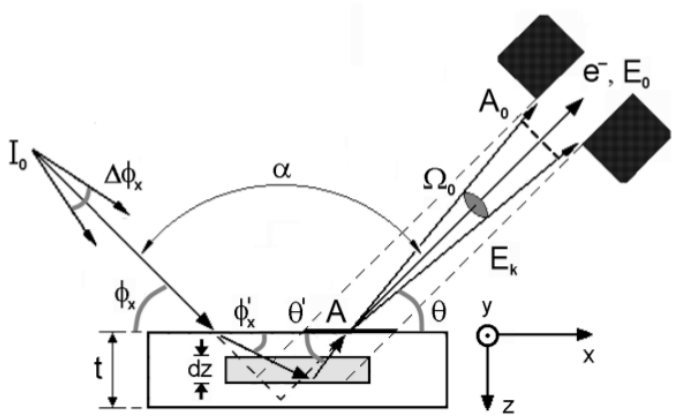

Figure 2.11: Geometry of an XPS setup.

A uniform beam of X-rays I_0, with an angular divergence $\Delta\phi_x$, illuminates a solid sample of thickness t, much greater than the inelastic attenuation lenght Λ_e, forming an angle ϕ_x with the surface. The exciting radiation penetrates to a depth z, where it is absorbed to yield the photoemission of electrons. Once leaked from the sample, the photoelectrons move in the direction defined by their wavevector, thus forming an angle ϑ with respect to the surface of the sample. Finally, the angle α between the incidence and the detection directions is determined by the geometry of the experimental setup. Using a non-monocromatized X-ray source, it is plausible to fix the incident flux of X radiation to a given constant value I_0 over the entire sample volume defined by $dx \cdot dy \cdot dz$, sensitive to the photoemission of electrons. In fact, the X-rays penetrate into the sample according to an exponential law, presenting an attenuation as a function of the path in the middle much weaker than that exhibited by the photoelectron during their way to the surface. Therefore, the active region of the production of photoelectrons without loss of energy is essentially exposed to a constant flow of X-rays I_0. The number of atoms or molecules in x, y, z is equivalent to the atomic density $\rho(z)$ of the element analyzed to a precise depth z within the

sample, multiplied by the volume element sampled in dx, dy, dz, that is

$$\rho(z)dxdydz. \tag{2.10}$$

The photoemission probability for an electron with a kinetic energy E_k, emitted within the solid angle of acceptance of the analyzer Ω_0, is proportional to the differential cross section of photoemission for the subshell k averaged over all the solid angle $d\sigma_k/d\Omega$ and multiplied by the acceptance angle Ω_0, whose value depends on the coordinates x and y, on the take-off angle ϑ and on the electron energy E_k, i.e.

$$\frac{d\sigma_k}{d\Omega}\Omega(E_k, \vartheta, x, y) \tag{2.11}$$

The fraction of electrons that reach the surface without loss of energy is given by

$$I(z) = I_0 e^{-\frac{z}{\Lambda_e \sin\vartheta}} \tag{2.12}$$

where Λ_e represents the inelastic mean free path, as we will discuss later. The efficiency of the detector is generally a function of the photoelectron kinetic energy, referred to as $D_0(E_k)$, that can be less than 1 if not all the electrons are collected in the solid angle Ω_0, or greater than 1 in the case where the spectrometer possesses a system for signal amplification. In conclusion, the differential intensity of the photoemission peak per unit of volume can be expressed as:

$$dN_k(z) = I_0 \cdot \rho(z)dxdydz \cdot \frac{d\sigma_k}{d\Omega}\Omega(E_k, \vartheta, x, y) \cdot e^{-\frac{z}{\Lambda_e \sin\vartheta}} \cdot D_0(E_k) \tag{2.13}$$

which, summed up over the whole sample thickness , gives the peak intensity as a function of the kinetic energy of the electron.

2.2 Angle-resolved X-rays photoelectron spectroscopy

Angle-resolved X-ray Photoelectron Spectroscopy (ARXPS) [62] is an experimental technique widely used for studying the thickness and the chemical composition of thin overlayers of solid materials. The depth range of this spectroscopic method is however limited by the *escape depth* of photoelectrons in the upper layers of the material.

After the photoemission process, the electrons drift through the solid and move toward the surface. During this phase, photoelectrons undergo elastic and inelastic collisions, due to interactions with electrons and ions in the crystal lattice.

Electron-phonon scattering is defined as a quasi-elastic collision, as it changes the direction of the electron leaving the solid but alter the kinetic energy of only a few meV. The inelastic scattering leads to losses of energy of several eV, related to the creation of electron-hole pairs or to the generation of electronic collective oscillations, called plasmons.

The XPS and ARXPS techniques are used for compositional analysis of the solids surfaces, due to the high surface sensitivity, that is a direct consequence of the small values of the inelastic attenuation length Λ_e of the photoelectrons. Λ_e is also called escape depth or inelastic mean free path (IMFP) between two inelastic consecutive collisions. Because the penetration depth of X-rays is of the order of μm, only the electrons emitted in the first atomic layers can reach the detector without undergoing inelastic scattering events.

In the simplest case, in which electrons are detected along the direction normal to the surface, the inelastic mean free path corresponds exactly to the escape depth. In this case, the probability that the electron, generated at a depth x, comes out perpendicular to the surface without undergoing inelastic collisions is equal to:

$$P(E_k) = e^{-\frac{x}{\Lambda_e(E_k)}} \tag{2.14}$$

In case of off-normal incidence (i.e. at an angle ϑ different from 90°, Fig. 2.12) the photoelectric intensity is:

$$I(z) = I_0 e^{-\frac{z}{\Lambda_e \sin\vartheta}} \tag{2.15}$$

where ϑ is the detection angle of photoelectrons and $z/\sin\vartheta$ is the distance traveled by the electron.

The inelastic attenuation length Λ_e can range between a few units and a few tens of angstroms.

This parameter turns out to be independent of the emission angle, slightly sensitive to the atomic nature of the species that limits the electronic pathway and dependent in large part on the kinetic energy of the photoelectron. From the previous equation, it can be noted that the 95% of the photoelectric signal consists of electrons that have traveled for distances shorter than $3\Lambda_e$. In fact,

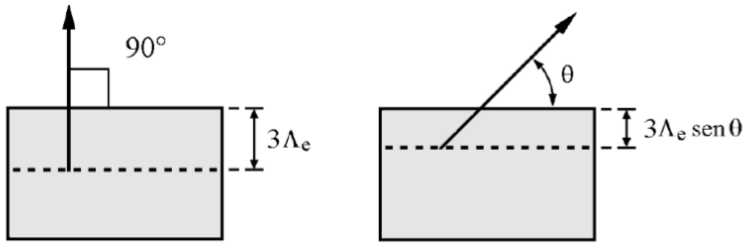

Figure 2.12: Two different geometries for an XPS experiment.

referring to Fig 2.12, when the direction of detection is along the normal to the surface, the average depth of the sample being analyzed will be then $\sim 3\Lambda_e$, but if one records a signal at an angle $\vartheta < 90$ with respect to the surface, the thickness sampled is reduced to $\sim 3\Lambda_e \sin\vartheta$. In conclusion, we can therefore affirm that the surface sensitivity increases for small detection angles. In the region of soft X-rays (100 - 1000 eV), it is possible to obtain a rough estimate of $\Lambda_e(E_k)$ using the empirical law:

$$\Lambda_e(E_k) = \frac{A}{E_k^2} + B\sqrt{E_k} \tag{2.16}$$

where $A = 2170$ and $B = 0.365$ are constants that can be applied at all types of inorganic compound.

A more accurate calculation for the inelastic attenuation length Λ_e was developed by Tanuma, Powell and Penn [63] for electrons with energies between 50 eV and 20 keV. The formula TPP-2M IMFP, which expresses Λ_e as a function of the kinetic energy E_{kin}, is:

$$\Lambda_e = E_{kin}\left[E_p^2\left(\beta\log(\gamma E_{kin}) - \frac{C}{E_{kin}} + \frac{D}{E_{kin}^2}\right)\right]^{-1} \tag{2.17}$$

with:

$$
\begin{aligned}
E_p &= 28.8\sqrt{\frac{N_v\rho}{M}} \\
\beta &= -0.10 + \frac{0.944}{\sqrt{E_p^2 + E_g^2}} + 0.069\rho^{0.1} \\
\gamma &= \frac{0.191}{\sqrt{\rho}} \\
C &= 1.97 - \frac{0.91 N_v \rho}{M} \\
D &= 53.4 - \frac{20.8 N_v \rho}{M}
\end{aligned}
$$

where:

$N_v =$ number of valence electrons per atom or molecule
$\rho =$ density of the material expressed in g/cm^3
M $=$ atomic or molecular mass in g/mol
$E_p =$ plasmon energy for a free electrons gas in eV
$E_g =$ band gap energy in eV

In figure 2.13, the behavior of the IMFP with respect to the kinetic energy is shown. An element can have different chemical states in different compounds (or even between surface and bulk), but this has no consequences in the determination of the values N_v because it is not identifiable with the chemical valence of an element.

There is in effect a certain ambiguity in the choice of this semi-empirical parameter, especially for those elements of the Periodic Table that exhibit a completely filled subshell; even if for alkaline metals, the value $N_v = 1$ coincides exactly with the valence, is not so for the halogens, in which $N_v = 7$. If we consider instead a compound, as Al_2O_3, there will be 6 electrons from Al ($N_v = 3$) and 18 electrons from O ($N_v = 6$) for a total of $N_v = 24$. Although the equation TPP-2M depends in a complex way on N_v through the terms E_p, β, C and D, the returned values of IMFP for solid elements and compounds does not depend significantly by the choice of N_v. In fact it has been found, also for elements very different from each other, that a variation of 50% of the value of N_v involves a change of the IMFP of less than 15%.

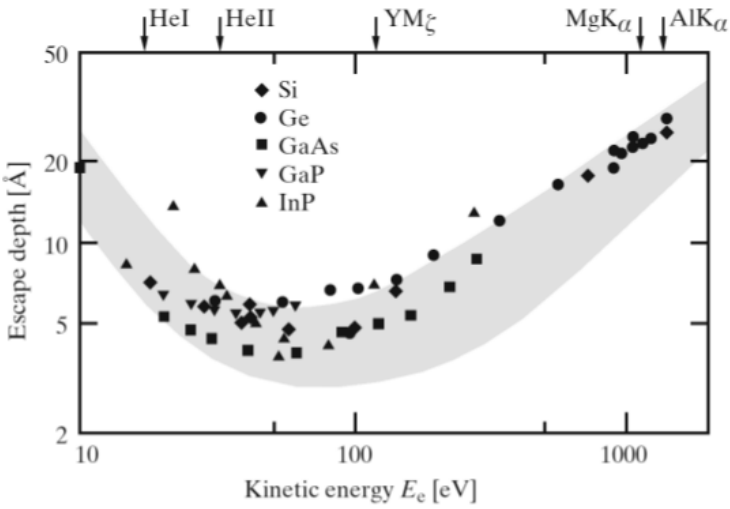

Figure 2.13: Inelastic mean free path versus kinetic energy for different atomic species.

The thickness of a layer can be estimated by considering the ratio $I(\vartheta)/I(0)$ However, this approach gives rise to large errors due to the strong correlation between the layer thickness d, the atomic density ρ_k and the inelastic attenuation length Λ_e of photoelectrons.

An angle-resolved XPS experiment can be carried out by moving the sample in two ways (Fig.2.14). In the *azimuthal scan* the polar angle ϑ is fixed and ϕ varies, whereas in the *polar scan* is the azimuthal angle ϕ to be fixed an ϑ is changed during the scan. If the photoelectronic signal modulation, recorded either by varying the angle ϑ or ϕ is due to diffraction effects, the analysis is called XPD (X-ray Photoelectron Diffraction). If, however, the photoelectron diffraction effects are negligible, by analyzing the signal modulation, varying the angle ϑ, it is possible to determine a distribution profile of the various elements present in the sample.

In addition, the dependence of the intensity of core level peaks as a function of the take-off angle ϑ arises not only because the length of the electrons

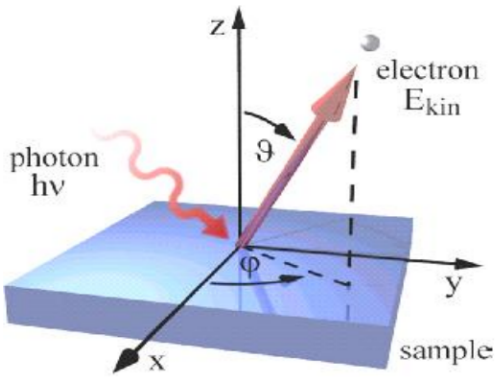

Figure 2.14: Angle resolved XPS. We define the azimuthal angle ϕ, the polar angle ϑ (also known as take-off angle), the incidence angle of the photon $\vartheta_{h\nu}$ and the angle between the photon incidence direction and the photoemission direction α

trajectory, subject to inelastic scattering, varies within of the solid, but also by the geometry of the XPS setup. In most of the experimental setups, the change in polar angle ϑ is obtained by rotating the sample directly. In this way, both the spot of the X-ray source on the sample surface and the focus point of the analyzer are modified in size and shape (Fig.2.15). Generally, in ARXPS studies this problem is solved by processing the experimental data by considering the relationship between the peak areas of atomic species in the film surface with the peaks area corresponding to the substrate. This procedure is performed in the hope that most of problems of geometric nature would cancel each other.

2.2.1 ARXPS of a semi-infinite substrate

According to the *escape depth* theory of the photoemission process, the photoelectronic signal, coming from the k-subshell of an atomic species i placed at a depth z, is reduced by the presence of upper layers through a Lambert-Beer factor:

$$exp\left(-\int_0^z \frac{1}{\Lambda_e(z')\sin\vartheta}dz'\right) \tag{2.18}$$

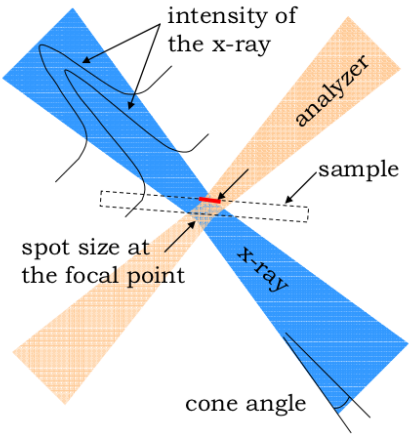

Figure 2.15: Diagrammatic representation of the x-ray intensity and analyzer efficiency in an XPS experiment. The red line is the region where the x-ray beam and the focal spot of the analyzer overlap with the sample surface.

where z is the depth, Λ_e represents the inelastic mean free path IMFP, while ϑ is the polar (or take-off) angle. Referring to the TPP-2M expression (2.17), we note that Λ_e varies as a function of z, because the film layers are made up of different materials. The IMFP is also dependent on the kinetic energy the photoelectron [64]. Starting from the differential intensity $dN_{k,i}$ of an XPS peak, given in equation (2.13), we consider a sample of infinite thickness ($t \gg \Lambda_e$) assuming that it has constant composition and uniform electron density, $\rho_i(z) = \rho_i$. Integrating $dN_{k,i}$ over the thickness t we obtain:

$$\begin{aligned} I_{k,i}(t) &= \int_0^t dz \int_S dxdy I_0 \rho_i D_0(E_k) \left(\frac{d\sigma_k}{d\Omega}\Omega_0\right) e^{-\frac{z}{\Lambda_e \sin\vartheta}} \\ &= \rho_i D_0(E_k) \frac{d\sigma_k}{d\Omega} \Lambda_e \sin\vartheta \left(1 - e^{-\frac{t}{\Lambda_e \sin\vartheta}}\right) \int_S dxdy \Omega_0 \cdot I_0 \end{aligned} \quad (2.19)$$

where I_0 is the intensity of the incident beam of X-rays, $D_0(E_k)$ is the efficiency of the analyzer, Ω_0 represents the solid angle of acceptance of the detector and $d\sigma_k/d\Omega$ is the differential cross section of photoemission for the subshell k, aver-

aged over the solid angle. We define the *response function* of the instrumentation for a peak k, as:

$$R_k(E_k, \vartheta) = D_0(E_k) \int_S dxdy\Omega_0 \cdot I_0. \tag{2.20}$$

If we consider an infinite thickness ($t \to \infty$), we have that $e^{-t} \to 0$, giving:

$$I_{k,i}(+\infty) = R_k(E_k, \vartheta)\rho_i \frac{d\sigma_k}{d\Omega}\Lambda_e \sin\vartheta \tag{2.21}$$

As shown in Fig. 2.11, the analysis system is described in terms of a solid angle of acceptance Ω_0, projected on an effective area A_0, perpendicular to the electrons trajectory, so the electrons, detected by the analyzer, are emitted from the surface $A = A_0/\sin\vartheta$ in the solid angle Ω_0. The expression for the response function can then be rewritten as follows:

$$R_k(E_k, \vartheta) = D_0(E_k)\Omega_0 I_0 \frac{A_0}{\sin\vartheta} \tag{2.22}$$

giving an XPS peak intensity which does not depend on the measurement angle.

$$I_{k,i}(+\infty) = \Omega_0 I_0 \rho_i \frac{d\sigma_k}{d\Omega} D_0(E_k) A_0 \Lambda_e \tag{2.23}$$

This result is fundamental for obtaining an XPS measure of the quantitative results about the sample composition. In fact, despite the quantities I_0, A_0 and D_0 are generally unknown, the relationship between the areas of two peaks from the same sample eliminates these terms, making it possible to neglect their dependence on the kinetic energy. It is thus possible to obtain the atomic density ratio of two chemical species k and k' by the formula:

$$\frac{\rho_k}{\rho'_k} = \frac{I_{k,i}(+\infty)}{I_{k',l}(+\infty)} \frac{\Lambda_e(E_k)}{\Lambda_e(E_{k'})} \frac{d\sigma_k}{d\Omega} \left(\frac{d\sigma_{k'}}{d\Omega}\right)^{-1} \tag{2.24}$$

where $I_{k,i}(+\infty)$ is the integrated area of the photoelectronic peak, subtracted of the inelastic background.

2.2.2 ARXPS on a substrate of finite thickness t

If the thickness t of the substrate is comparable with the IMFP, $t \sim \Lambda_e$, then the sampled depth will be greater than t, leading to a reduction of the signal as

the angle of take-off increases, according to the expression:

$$\begin{aligned} I_{k,i}(\vartheta) &= \Omega_0 I_0 \rho_i \frac{d\sigma_k}{d\Omega} D_0(E_k) A_0 \Lambda_e \left(1 - e^{-\frac{t}{\Lambda_e \sin\vartheta}}\right) \\ &= I_{k,i}(+\infty)\left(1 - e^{-\frac{t}{\Lambda_e \sin\vartheta}}\right). \end{aligned} \tag{2.25}$$

2.2.3 ARXPS on a semi-infinite substrate with a uniform film of thickness t

Unifying what has been showm in the two preceding paragraphs, we can consider the case where, passing from a shallow angle to one normal to the surface, the photoemission intensity from the substrate tends to increase, while the film one decreases. For the k, i peak of the bulk with energy E_k, it results that:

$$\begin{aligned} I_{k,i}(\vartheta) &= \Omega_0 I_0 \rho_i \frac{d\sigma_k}{d\Omega} D_0(E_k) A_0 \Lambda_e(E_k) \left(e^{-\frac{t}{\Lambda'_e(E_k)\sin\vartheta}}\right) \\ &= I_{k,i}(+\infty)\left(e^{-\frac{t}{\Lambda'_e(E_k)\sin\vartheta}}\right) \end{aligned} \tag{2.26}$$

while for the k, j peak one has:

$$\begin{aligned} I_{k',j}(\vartheta) &= \Omega_0 I_0 \rho_j \frac{d\sigma_{k'}}{d\Omega} D_0(E_{k'}) A_0 \Lambda'_e(E_{k'}) \left(1 - e^{-\frac{t}{\Lambda'_e(E_{k'})\sin\vartheta}}\right) \\ &= I_{k',j}(+\infty)\left(1 - e^{-\frac{t}{\Lambda'_e(E_{k'})\sin\vartheta}}\right). \end{aligned} \tag{2.27}$$

Here, the use of the apex for the escape depth Λ'_e in the expression 2.26 has to be noted, because the thin film is responsible of the attenuation, while the energy at which Λ'_e is calculated, is that of the photoelectrons from the substrate. The relationship between the areas of photoemission peak is given by:

$$\frac{I_{k',j}(\vartheta)}{I_{k,i}(\vartheta)} = \frac{I_{k',j}(+\infty)}{I_{k,i}(+\infty)} \frac{1 - e^{-\frac{t}{\Lambda'_e(E_{k'})\sin\vartheta}}}{e^{-\frac{t}{\Lambda'_e(E_k)\sin\vartheta}}} \tag{2.28}$$

with

$$\frac{I_{k',j}(+\infty)}{I_{k,i}(+\infty)} = \frac{\rho_j \frac{d\sigma_{k'}}{d\Omega} \Lambda'_e(E_{k'})}{\rho_i \frac{d\sigma_k}{d\Omega} \Lambda_e(E_k)} \tag{2.29}$$

Finally, if are known the values of the lengths of inelastic attenuation $\Lambda'_e(E_{k'})$, $\Lambda'_e(E_k)$ and $\Lambda_e(E_k)$, the atomic density of the two materials ρ_j and ρ_i and differential cross sections, then it is possible to derive an estimation for the thickness t by reversing the previous formula.

2.3 Ultrafast spectroscopy of carbon nanotubes

Ultrafast optical spectroscopy techniques are widely used to study the dynamics and the kinetics of scattering and relaxation processes of excited carriers in solid state systems. These processes typically take place in a few femtosecond to some picosecond time interval, so they are outside the time scale accessible to conventional electronic instruments. In order to overcome this limitation pump-probe techniques are employed. In time resolved pump-probe optical experiments an intense light pulse pumps the sample in an excited state whilst a weaker pulse probes the transient variation of its optical properties, such as transmittivity or reflectivity, at a selectable delays from the excitation. The capability of generating a few femtoseconds light pluses, with mode-locked lasers, and to precisely control their relative delays allows to follow the transient relaxation overcoming the detector speed limit. It can be shown that in a time resolved transient transmittivity experiment, performed on centrosimmetric materials, the detected signal I_{pp} is dominated by the third order nonlinear polarization of the medium $P^{(3)}$.

$$I_{PP}(\omega_{pr}, \tau) = 2\omega_{pr} Im \int_{-\infty}^{+\infty} E_{pr}(t') P^3(\tau, t') dt' \tag{2.30}$$

where ω_{pr} is the frequency of the probe pulse, E_{pr} is its electric field envelope function and τ is the relative time delay between the pump and the probe pulses. If the processes involving the carrier relaxation dynamics are slower than the dephasing times of the polarization, the optical transients are due to a variation of the frequency dependent absorption coefficient $\alpha(\omega)$ and thus to a variation of the complex part of the dielectric function ϵ_2.[2] Using the density matrix

[2]The absorption coefficient depends explicitly on the refractive index n which contains also the real part of the dielectric function. Anyway the real and the complex part of the dielectric function are linked together by the Kramers-Kroenig transformations which prescribes the causality of the optical process. Even if these transformations written in the usual form [65]

formalism and considering only transitions between two particular states $|1\rangle$ and $|2\rangle$ the variation reads

$$\Delta\epsilon_2(\omega) = \frac{2\pi e}{m_e\omega}|M_{21}|^2\left[(1-\rho_{22})\Delta\rho_{11} - \rho_{11}\Delta\rho_{22}\right] \tag{2.31}$$

where M_{21} is the transition dipole matrix element and ρ_{ii} are the population of the two states. In case of small population of the excited state ($\rho_{11} << \rho_{22}$) the variation of the absorption coefficient is

$$\Delta\alpha(\omega) = \frac{2\pi e}{m_e n(\omega) c}|M_{21}|^2\left[\Delta\rho_{11} - \Delta\rho_{22}\right] \tag{2.32}$$

where the variation of the refractive index is also neglected. This incoherent limit of the absorption variation is frequently used as starting point for the interpretation of transient absorption spectra [67]. This formula describes a saturation of the optical transition and give an overall reduction of the absorption coefficient commonly referred to as photobleaching. If more than two states are involved an additional optical transition may arise from the first excited state to another state at an higher energy. This process gives a transient increase of the absorption coefficient at the probe frequency, commonly referred to as photoabsorption. (Fig.2.16)

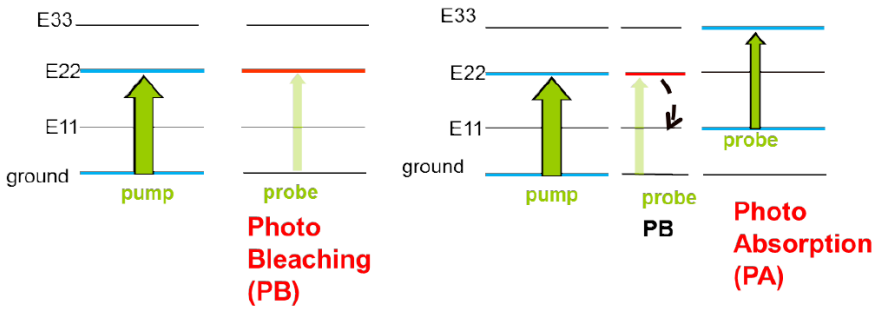

Figure 2.16: Schematic representation of a photobleaching and a photoabsorption process in a 4 level system.

holds only for linear systems a modified version can be obtained for nonlinear systems as well (see for example [66]).

In carbon nanotubes the presence of strong exciton effects justify the use a multilevel approximation. Resonant excitation of higher lying excitonic states, such as E_{22} is followed by a rapid (< 100 fs) intersubband relaxation towards the lowest exciton state, due to the strong interaction with phonons [68, 69]. It has also been proposed that the exciton levels in SWCNT belongs to an exciton manifold which will give an additional intersubband relaxation channel [70]. The intersubband relaxation dynamics was directly measured in isolated carbon nanotubes by Manzoni *et al.* [71] using a tunable 10 fs pulsed laser systems. The ground state relaxation dynamics was found in the order of 1 ps. This results conflicts with the relaxation times measured with time resolved photoluminescence experiments which are in the order of tens of nanoseconds. The huge difference can be due to nonradiative relaxation processes detectable only by the former technique.

If the excitation intensity is sufficiently high, exciton-exciton interaction can take place. The interaction of two excitons can lead to an exciton-exciton annihilation process (EEA) in which one of the exciton rapidly relax transferring it energy to the other and promoting it to an higher excited state. The signature of this process was detected by several researchers using photoluminescence spectroscopy, and time resolved transient transmittivity [72, 73] In case of EEA the excite state population n_{ex}, being a two body process, follow a simple nonlinear rate equation which reads

$$\frac{dn_{ex}}{dt} = -\gamma n_{ex}^2 (t)$$

where γ is a time independent rate constant from which an annihilation rate in the order of 0.8 ps^{-1} can be calculated [72]. Other researchers fund an explicit time dependence for the rate constant γ in the form $\gamma = \gamma_0 t^{-1/2}$. This time dependance is expected from a diffusion limited EEA process in one dimensional systems [74] but the discrepancies between the two relaxation dynamics are still matter of debate [67].

On the other side metallic carbon nanotubes (MSWCNT) present both strong exciton and interband transitions and their transient optical properties are somewhat less studied. The excited carriers dynamics in this systems where investigated primary via time resolved photoemission spectroscopy [75] which can directly track the electron distribution and its relaxation kinetic in the vicinity of the Fermi level. Since the semiconducting tubes do not contribute

to the electronic population at the Fermi level this technique can, in principle, single out the dynamics of the metallic tubes even in a sample with the usual mix of semiconducting and metallic species. From the differential photoemission spectra Hertel and Moos [75] found that electron-electron scattering processes in MSWCNT rapidly thermalize the photoexcited electron population on a 200 fs time scale. for longer delays the slower electron-phonon scattering processes cool the electron population until the thermal equilibrium with the lattice is reached. The coupling of a thermalized electron population with the lattice was described using the two-temperature model [76]

$$\begin{aligned} C_e \frac{dT_e}{dt} &= \nabla \left(k \nabla T_e \right) - H \left(T_e, T_l \right) + S \left(t \right) \\ C_l \frac{dT_l}{dt} &= H \left(T_e, T_l \right) \end{aligned} \quad . \tag{2.33}$$

Where $S\left(t\right)$ is the laser pulse energy, T_e and T_l are the electron and the lattice temperature, k is the electronic thermal conductivity, C_e and C_l are the electronic and lattice heat capacities. The coupling term $H\left(T_e, T_l\right)$ describes the interaction between the electronic and the phononic degrees of freedom which, for electronic and phononic temperature similar or smaller than the Debye temperature Θ_d reads [77]

$$H \left(T_e, T_l \right) = \frac{144 \zeta \left(5 \right) k_b \gamma}{h} \frac{\lambda}{\Theta_d^2} \left(T_e^5 - T_l^5 \right) \tag{2.34}$$

where ζ is the Reimann zeta function, k_b the Boltzmann constant, γ the electronic heat capacity coefficient, h the Planck constant and λ the electron-phonon mass enhancement factor. λ is related to the electron-phonon scattering time τ_{e-ph} [78] which for MSWCNT turns out to be in the order of 15 ps. This long scattering time is consistent with the extraordinary current-carrying capacity of MSWCNT and their long ballistic electron mean free path [79].

2.3.1 Experimental Setup

Two-color high fluence setup The light source of this setup is an α-line amplified Ti:Sapphire laser system. The pulse wavelength is centered around 795 nm with a temporal width about 150 fs FWHM and an energy of $\approx$600 μJ per pulse. The repetition rate is 1 KHz, therefore the average output power is 0.6

W, and the peak power is 4×10^9 W. The 70 % of the output beam is directed in a traveling wave optical parametric amplifier (TOPAS), manufactured by Light Conversion, whist the remaining 30 % is further attenuated and used as a probe beam. The TOPAS output frequency can be tuned from 1150 to 1600 nm with an average output power of nearly 40 mW. In order to further extend the tunable range a pair of BBO nonlinear crystal are employed. With this configuration the pump photon energy can be tuned in the 575-800 nm and in the 290-400 nm intervals. Unwanted components at the fundamental TOPAS output frequencies are eliminated using a dispersive element and a set of filters. The pump fluence range depends on the used configuration but values between 2.5 and 20 mJ/cm^2 are commonly achievable. In fig.2.17 a schematic representation of the optical line is reported.

The spot sizes at the sample position are 100 μm and 50 μm for the pump and the probe respectively. Due to the low repetition rate of laser source the pump beam is chopped at 500 Hz and a boxcar integration technique is used to retrieve both the static value of the transmittivity (or reflectivity) signal and its variation. The instrument resolution is in the order of $\Delta I/I \approx 1 \times 10^{-4}$.

2.4 Device manufacturing and samples list

The samples analyzed in this thesis can be classified in three series which differ from each other for the type of nanotubes used, the contacting pads, the geometry of the PV devices and especially the way in which CNTs are treated before being deposited on silicon. All the samples had been realized at the Carbon Lab, in the Physics Department of the University of Roma Tor Vergata.

First series devices. The first devices were created starting from a rectangular slab of n-type silicon, provided by FBK (Fondazione Bruno Kessler, Trento, Italy), consisted of 5x10 mm^2 slices of a SiO_2 passivated (thickness 300 nm), with a resistivity of 3-12 $\Omega\cdot$ cm with an aluminum ohmic back contact. The oxide layer was patterned by a lithographic process with a positive resist followed by a chemical etching in order to obtain a bare silicon window delimited aside by two SiO_2 steps, yielding a device active area 5x5 mm^2. Networked SWCNT films were obtained from metallic and semiconducting SWCNT powders. Metal-

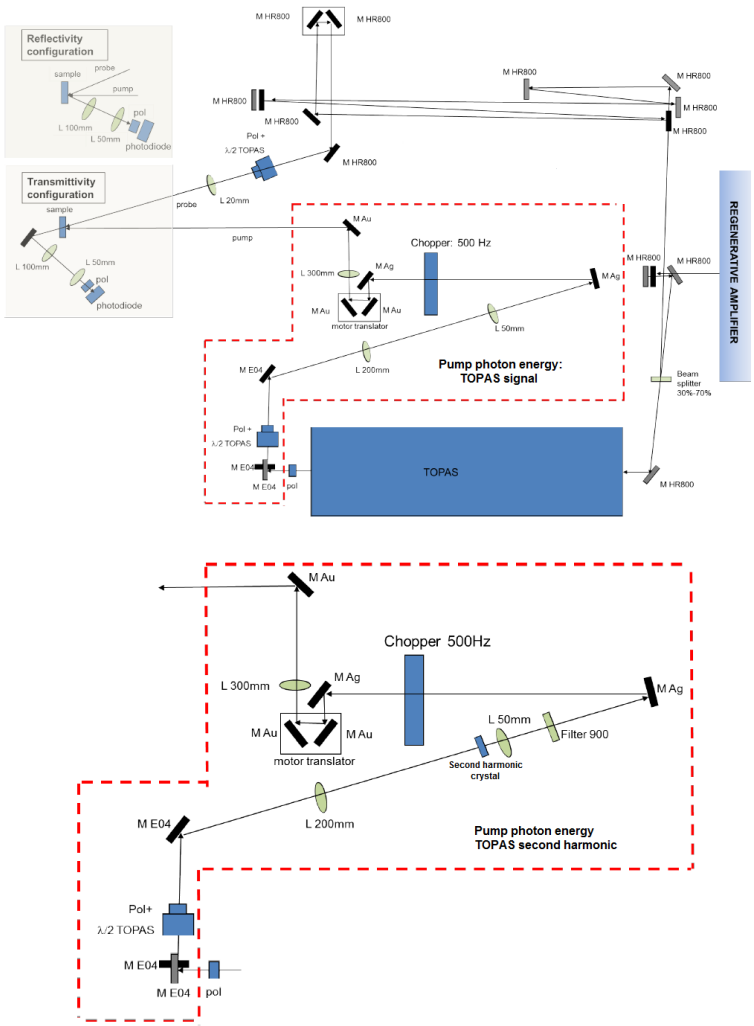

Figure 2.17: Schematic representation of the high fluence time resolved setup

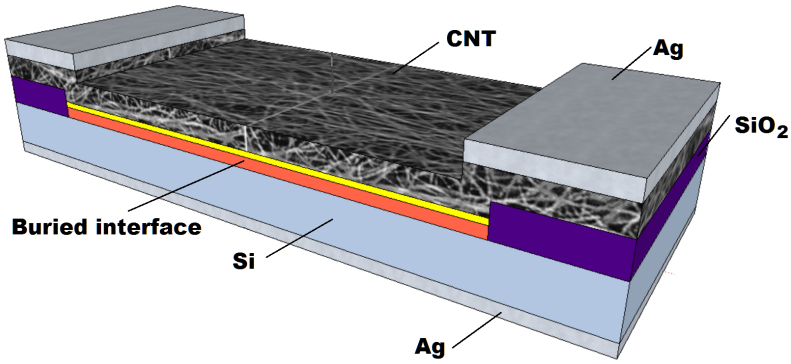

Figure 2.18: Representation of a first series device.

lic SWCNT are characterized by having diameters ranging from 0.7 and 1.4 nm, carbon >90%, purity 77%, and a bulk density of 0.09 g/cm^3. Semiconducting SWCNT, mostly with a (6,5) chirality, had diameters varying from 0.7 and 0.9 nm, carbon > 90%, purity 77%, and a bulk density of 0.14 g/cm^3. For the deposition of the SWCNT film onto the Si patterned substrates, a SWCNT dispersion was prepared by ultrasound treatment of 100 μg of SWCNT powder in a 3 wt% aqueous solution of Sodium dodecyl sulfate (SDS). After 1 hour of ultrasound bath, the dispersion was left to settle down, and the clear supernatant containing unbundled nanotubes was divided from the precipitate (mostly bundled nanotubes) and used to fabricate the film. The filtration process of the SWCNT dispersion in water was carried out by a vacuum filtration assembly to speed up the process using a cellulose acetate membrane filter (PALL corp. 0.45 μm diameter pores).

Once the SWCNT film was cast on the membrane filter, the residual SDS was removed by washing with deionized water and subsequently by an ethanol-methanol-water mixture (15:15:70 in volume). Films with different thickness were obtained by filtering different aliquots in volume of the same solution. The SWCNT film was transferred on the patterned Si substrate flipping it over and pressing the SWCNT coatedmembrane onto the Si/SiO_2 surface. To improve the adhesion and to promote the SWCNT film detachment from the membrane, this latter is soaked with ethanol and subsequently dried under a vacuum. The

residual cellulose acetate membrane lying on top of SWCNT film is removed by dipping the entire sample in warm acetone (30 °C) three times and finally rinsing in isopropanol. Finally, two silver painted metallic contacts are created on the SWCNT film just on top of the SiO_2 steps. The presence of SiO_2 steps between the metal electrodes and the Si underneath is fundamental to avoid short-circuits causing electron leakage. A scheme of the device is reported in Figure 2.18.

The samples used in chapter 3 and chapter 5 belongs to this first type of devices.

Second series devices. The devices of the second series are characterized by a change in the geometrical shape from rectangular to squared and to an overall improvement of the substrate architecture, carried out at the Bruno Kessler foundation (Figure 2.20). The substrates are based on a 1 x 1 cm^2 slice of n-type Si(100) (resistivity 312 Ω cm), passivated with 300 nm of SiO_2, covered by Cr/Au front electrode in which a window of 3 x 3 mm^2 has been obtained by lithographic processes. A Cr/Au ohmic contact was finally realized on the backside of the sample. The CNTs used here has a (7,6) chirality but were dispersed and deposited following the same procedures described in the previous paragraph, a SEM image of these films are reported in Figure 2.19. Devices analyzed in chapter 4 belong to this second series.

Third series devices. More recently, a change in the CNT dispersion and deposition method has led to huge improvement of the photovoltaic performances, allowing a third series solar cell to reach the record efficiency of 12.2% (Figure 2.21). This cell, obtained by vacuum-filtrating 2ml of (7,6) semiconducting nanotubes, will be characterized in Chapter 5.

To better disperse the suspension, CNTs were tip-ultrasonicated (Branson S250A, 200 W, 2% power, 20 KHz) in an ice-bath for one hour and the unbundled supernatant was collected. The result was a well-dispersed suspension which is stable for several months. Carbon nanotube films were fabricated by a vacuum-filtration process with a mixed cellulose ester filters (Pall GN6, 1 in diameter, 0.45 mm pore diameter). Subsequently, a rinsing in water and in a mixture of ethanol, methanol, and water (in ratio 15:15:70, respectively) was performed, in order to remove as much surfactant as possible. Samples were prepared by

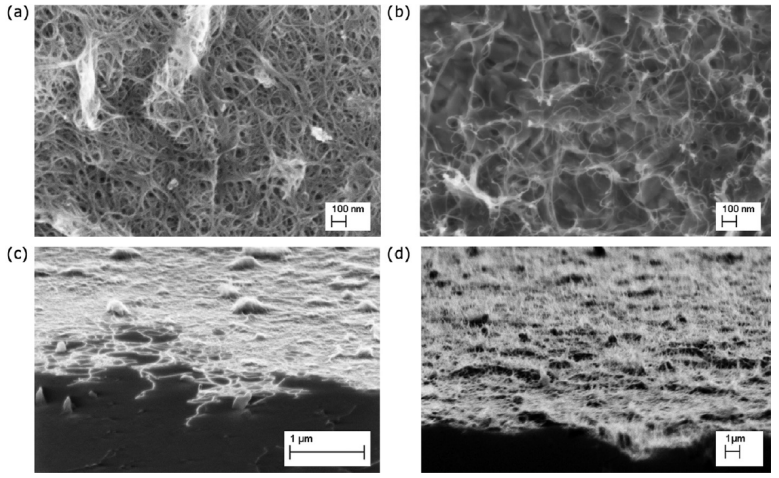

Figure 2.19: Scanning electron micrographs of SWCNT (a,c) and MWCNT (b,d) films at different magnifications 10,000X(c,d) and 200,000X (a,b). Carbon nanotube films appear as dense and porous (dark holes) random networks (a,b). In the image taken at grazing incidence (c,d) ($\sim 90^\circ$ respect with the plane normal), it is possible to observe micro-structures consisting in self-assembly ripples made of SWCNTs. Conversely, MWCNTs just aligned in the vertical direction. Dark areas correspond to the glass substrate underneath. Adapted from Ref. [80]

the newly developed *dry-transfer printing method*, which consists in soaking the SWCNT film with ethanol, in order to improve its adhesion, and then pressing it onto a substrate (which can be silicon, glass or also plastic) with a glass slide. After few minutes, the dried cellulose filter is removed by peeling it, leaving the SWCNT film adhered on the substrate. The same CNT film has been also transferred on glass for optical measurements.

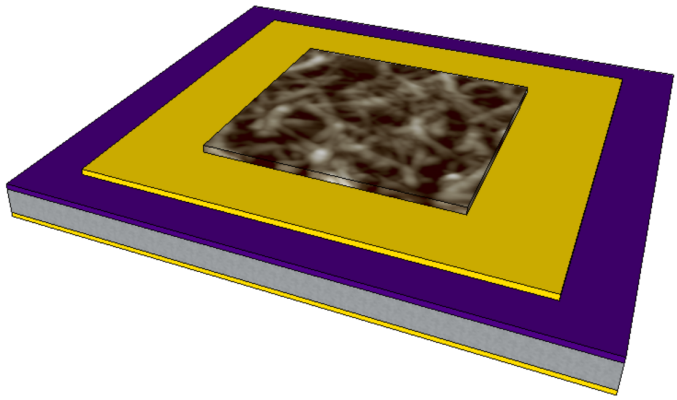

Figure 2.20: A scheme of a device belonging to the second series. The pattern used to sketch the CNT film is a real AFM image of the device surface.

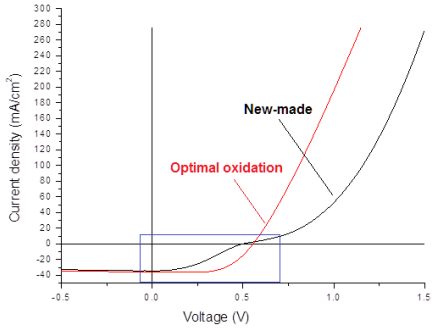

Figure 2.21: J-V curves with a solar simulator in standard conditions (100 mW/cm^2, AM 1.5) for a new-made (in black) and optimally oxidized (in red) solar cell of the third series. The power conversion efficiency was 12.2%.

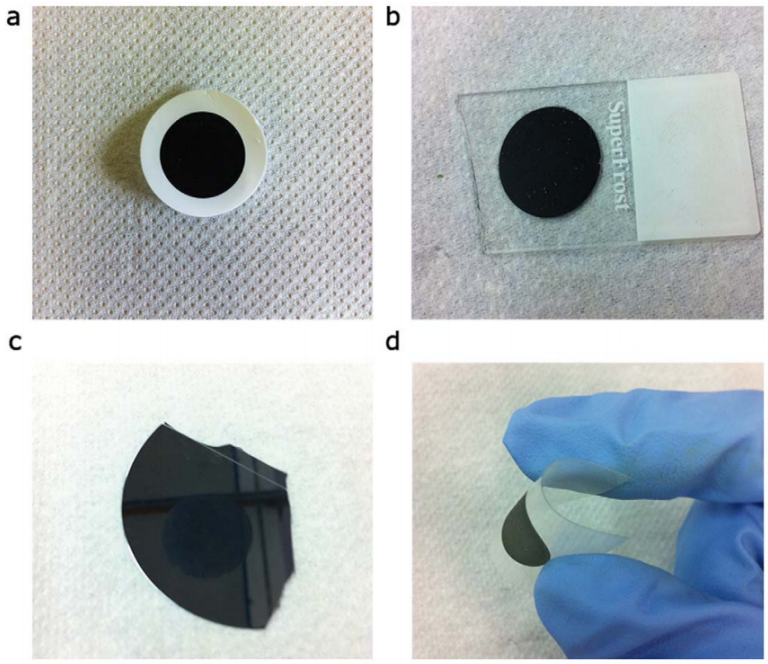

Figure 2.22: A SWCNT film realized on cellulose filter (a) may be deposited on glass (b), silicon (c), and plastic foils (d). Adapted from Ref. [81]

Chapter 3

AR-XPS analysis of the buried interface in CNT/Si PV devices

As previously seen in section 1.4, in CNT/Si heterojunctions, the SWCNT film works as a transport path for charge carriers (holes), while the n-type silicon wafer, used to extract electrons, is the main photogeneration site from which electrons are collected through an ohmic junction with the metal contact underneath [82]. In this kind of device, the SWCNT film thickness plays a double role: it should allow the largest number of photons to reach the Si layer, and, at the same time, it must be conductive enough to allow charge transport without significant losses. It was also claimed [83], that oxide-free Si surfaces favour the formation of more efficient heterojunctions with CNTs. As devices are prepared in air, it appears appropriate to investigate if the presence of any oxide influences the formation and the behaviour of the junction. Speculations about the role of a silicon oxide layer on the cell efficiency have been proposed [83, 84] but direct evidence of this layer and its physical and chemical characteristics (thickness, homogeneity, chemical composition) had not been so far reported in literature. The aim of our first study [85] was to investigate by AR-XPS the electronic properties of the buried interfaces in the hybrid CNT/Si heterojunction and

their effect on the overall efficiency of the devices. This is accomplished by an extensive modeling of the complex CNT/SiO_x/SiO_2/Si heterostructure which also provided important details on the thickness of each layer, along with an indication of partial coverage of the surface. Incidentally, we show that AR-XPS is an excellent tool for non-destructive depth profiling of nanostructured devices. For the first time, we have been able to show that the thickness and the chemical composition of the buried interface can determine the efficiency of the photovoltaic cell. In particular, in this chapter we will start showing how XPS can provide straightforward information about changes in the Si-O layer resulting from etching effects aimed to control the thickness of the buried silicon oxide interface.

3.1 Experimental and computational details

Samples. In this study, three samples belonging to the first series (see section 2.4) had been analysed:

- **Samples A and B**: both substrates were prepared in a single batch and exposed to air for several days prior to the SWCNT film transfer;
- **Sample C**: nanotubes were transferred on the substrate as soon as the Si substrate was prepared.

The sheet resistance and the optical transmittance (OT) measured at 550 nm for the three samples are reported in Table 3.1.

Sample	η (%)	R_s (kΩ)	OT at 550 nm (%)
A	0.26%	2.4	64.0
B	0.20%	1.8	66.0
C	2.72%	0.4	65.0

Table 3.1: Efficiencies (η), sheet resistances (R_s) and optical transmittance (OT) at λ= 550 nm for the three PV devices under consideration.

Efficiency Measurements: the PV efficiency measurements were carried out using a solar simulator Oriel LSO106 equipped with a 150 W Xe lamp, an AM1.5

global filter, and a Keithley source-meter 6202A. The devices were connected to the source-meter according to this scheme: Al contact on Si- ground, SWCNT film - signal. The results in term of efficiency derived from I/V curves are reported in Table 3.1. IV curves measured after etching of the whole junction were collected with an halogen lamp and a custom-made IV tracker, driven by a National Instrument PCIe-6251 data acquisition board through the LABview software package.

XPS Measurements. The XPS data have been collected at the Surface Science and Spectroscopy Lab of the Universita Cattolica del Sacro Cuore (Brescia, Italy) with a SCIENTA R3000 electron spectrometer, operating in the transmission mode and working with a 30 acceptance angle. The Al K_α line ($h\nu$ = 1486.6 eV, resolution 0.85 eV) of a non-monochromatized dual-anode PsP X-ray source was used, running at a power of about 110 W. The base pressure in the sample analysis chamber was 2 10^{10} mbar. With the sample holder clips being coated with gold, the binding energy (BE) of the Au $4f_{7/2}$ peak (BE = 83.96 eV) [86] was taken as a reference. In the present study, the analyzer transmission (or large acceptance) mode has been employed to maximize the count ratio and, thus, to speed up the acquisition time while keeping the energy resolution required for a reliable peak fitting. Because of the large thickness of CNT overlayer and the weak XPS signal from silicon, any improvement of the signal-to-noise ratio has been fundamental. The effect of the analyzer angular acceptance on XPS measurement is usually weak, especially when (as in the present case) the angle between the source and the analyzer axis is close to the magic angle (54.5°) and when the tilt angle is lower than 70°. Waligorski and Cooke [87] have shown that a large acceptance can improve the signal-to-noise ratio without reducing the effectiveness with which the detector can measure the angular distribution. ARXPS calculations of the C 1s and Si 2p peak areas carried out with the DDF approach for a CNT/silicon interface (see Figure 3.1) indicate that discrepancies between the C 1s and Si 2p relative intensities are kept below about 5% in the whole -range considered (0 - 60°). Since in Ref. [88], it has been shown that deviation from the predicted behavior can be found for takeoff angles above 70°, in the present study the maximum takeoff angle of all experiments is limited to 50°.

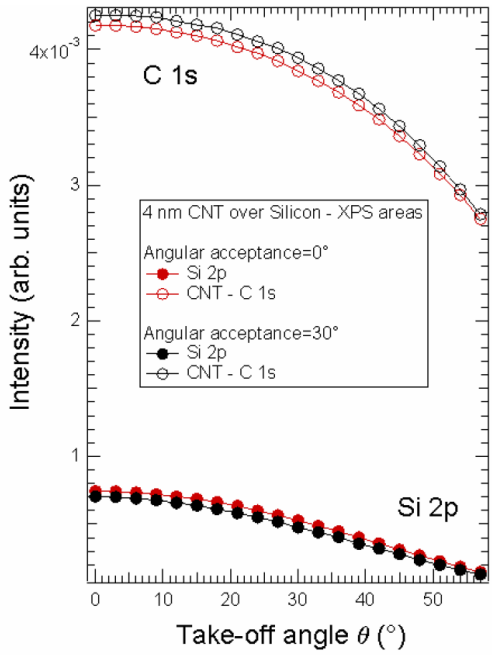

Figure 3.1: Calculated XPS intensities for C 1s and Si 2p peaks in an ARXPS experiment carried out on a 4 nm thick CNT layer deposited over clean silicon. The calculations have been carried for 0° (red lines and symbols)), and 30° (black lines and symbols) analyzer angular acceptance cone. In the calculations the experimental geometry was properly accounted for. Photon source: Al K_α X-ray emission at 1486.6 eV.

Modeling of AR-XPS. Modeling and simulation of the multilayer structure, aimed to fit the XPS peak angular dependence, was carried out with code developed at the Surface Science and Spectroscopy Lab, based on the IGOR 6.3 programming language. A variety of physical processes are known to play an important role in the XPS signal generation, such as elastic and inelastic scattering in the interior of the solid, surface excitations, and intrinsic excitations following the ionization that precedes the electron emission in XPS. Generally, such processes can occur repeatedly (multiple scattering) before the electron is

ejected from the surface, giving rise to a complex combination of effects responsible for some important features observed in experimental spectra. In XPS, the core-level peak intensities I(E_k, ϑ) of a selected layer at a depth d with a thickness t can be evaluated exactly using the theory presented in section 2.2.3, or, in a more simplified way, using the formula:

$$I(E_k, \vartheta) = N \cdot X_s \int_d^{d+t} DDF(E_k, \vartheta, z) dz \tag{3.1}$$

where N is the atomic density of the involved species, and X_s represents the photoionization cross section [89], depending also on the analyzer geometry; DDF(E_k, ϑ, z) is the escape probability, known as depth distribution function, of an electron generated at a depth z with a kinetic energy E_k at an angle ϑ, with respect to the surface normal (Figure 3.2).

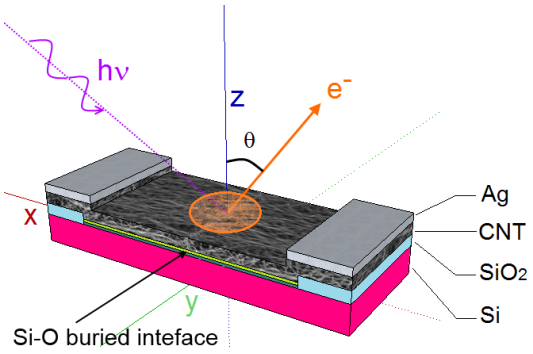

Figure 3.2: Schematic drawing of the CNT-Si hybrid heterojunction and representation of the XPS experimental geometry. The angle between the direction of the outgoing electron and the z axis is the photoelectron takeoff angle, which is referred to in the angle-resolved measurements.

According to the Lambert-Beer law, the DDF function is usually approximated with a Poisson distribution $\Phi = \exp(z/\lambda \cos\vartheta)$ [90], where λ is the IMFP [91]. When the direction of detection is along the normal to the surface ($\vartheta = 0$), the average depth of the sample being analyzed will then be <3λ, but if one records a signal at an angle $\vartheta > 0$ with respect to the surface, the sampled

thickness is reduced to $\sim 3\ \lambda \cos\vartheta$. In this work, following Ref. [92], we used Monte Carlo DDF calculations, including inelastic and elastic electronic scattering, in the transport approximation. The photoemission asymmetry parameters have been taken into account for each core-level. Monte Carlo calculations of electron trajectories have been carried out in order to predict the XPS peak intensities from each layer in our heterostructures.

Raman Measurements. Raman spectra have been collected with a Renishaw spectrometer equipped with a He- Ne laser (λ = 632.8 nm) and a Leika confocal microscope. A 50x microscope objective (N.A. = 0.75) has been used to collect the inelastically scattered light in a backscattering geometry. The laser power on the sample was 1.4 mW.

3.2 Results and discussions

Carbon 1s Core Levels. In Figure 3.3, the C 1s XPS core levels of the three samples are shown. An asymmetric peak with maximum at a binding energy (BE) of 284.5 eV is detectable, with a tail on the high BE side, ranging up to 292 eV. Panels a, b, and c refer to the data of samples A, B, and C, respectively. For a more detailed analysis of the C 1s lineshapes, we resorted to a data fitting aimed to identify the different carbon bonds contributing to each spectrum, along with their relative weight. The fitting results for the C 1s photoemission peaks are also shown in Figure 3.3. For the main peak at 284.5 eV, due to the contribution of the C-C bond, the peak fitting is carried out on the basis of the Doniach-Sunjic [93] line shape, as is usually done for CNTs [94]. In all these fits, we use a fixed value for the asymmetry parameter of the carbon peak (α = 0.075), as reported in the literature for graphene sheets [95]. In the peak fitting, we considered the possible contributions of four peaks ascribed to the C-C, C-O, C=O band O-C=O bonds [96]. In the fitting procedure, the binding energy of each peak has been kept fixed, according to the values available in the literature [96], while the full width at half-maximum (fwhm) and the intensity were used as parameters in the fitting. The fwhm difference among similar peaks in the three samples was allowed to vary within 10%, assuming that these differences could be ascribed to the different environment where the specific carbon-oxygen bonds (C-O, C=O and O-C=O) could be found, i.e., in the

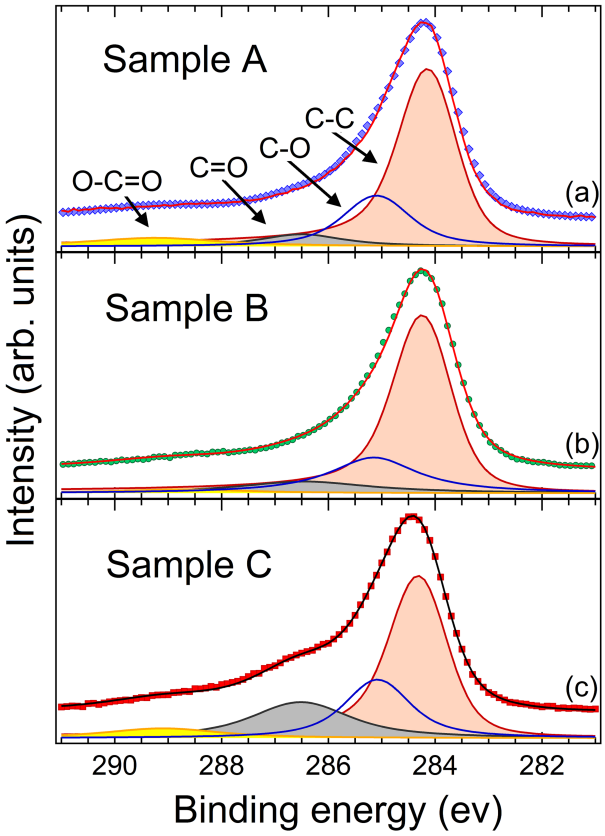

Figure 3.3: C 1s XPS core level data, and fitting with 4 components related to the C-C, C-O, C=O and O-C=O bonds. Panels **a**, **b**, and **c** refer to samples A, B and C, respectively. All spectra have been normalized to the maximum of the C 1s peak at 284.5 eV.

CNT bundles, at the surface, or at the CNT-SiO_x interface. For each sample, the relative weights of the four peaks are reported in Table 3.2.

As can be seen in Table 3.2, most of the C 1s spectral weight comes from the C-C bond (about 60%), while the remaining weight is ascribed to single and

Sample	C-C (%)	C-O (%)	C=O (%)	O-C=O (%)
A	65.2	20.7	6.3	7.8
B	65.8	21.1	9.9	3.2
C	53.7	21.7	19.0	5.6

Table 3.2: Results of the Analysis of the C 1s XPS Peak

double bonds between carbon and oxygen. Within the accuracy of the fitting procedure, we can assume that the three samples do not present significant differences among the main components. This justifies our choice to normalize all the ARXPS spectra to the C 1s core level intensity, collected at a take-off angle $\vartheta = 0°$ between the analyzer and the normal to the sample surface.

Silicon 2p Core Levels. Figure 3.4 shows the Si 2p core levels of the three samples collected at different take-off angles in the 0-50° range. Results from sample A, B, and C are shown in the left, central, and right panels, respectively. As can be observed, two main peaks corresponding to bulk silicon (BE = 99.5 eV) and to the SiO_2 native oxidation layer (BE = 103.2 eV) contribute to the spectral weight. On the basis of the binding energies alone, the central peak could be ascribed both to the silicon carbide SiC (with a BEs reported in the range from 99.85 eV [97] to 100.8 eV [98]) and to the non stoichiometric silicon oxide SiO_x (BE from 100.4 to 103.23 eV) [88]. We exclude silicon carbide as the origin of the middle peak, as we did not observe its counterpart in the C 1s spectral region. Indeed, in silicon carbide a C 1s peak at 282.5 eV is expected, as reported in Ref. [99], but this peak is absent in all samples here considered. Therefore, we are able to conclude that the central peak is due to SiO_x. The three peaks so far identified show a distinct angular dependence as the analyzer take-off angle ϑ is swept from the normal emission geometry (0°) to a more grazing emission angle (50°). In particular, we observe a steep decrease of the Si bulk signal as the probe is getting more surface sensitive, a roughly constant behavior of SiO_x, and a weak decrease of the SiO_2 contribution. As expected, this behavior agrees with the sequence of layers of the heterostructure. Silicon is the deepest layer, while SiO_2 and SiO_x lay in-between silicon and the CNT topmost layer. In Figure 3.4, the fitting results for the angle resolved Si 2p photoemission peak are also shown. All peaks are fitted by using Voigt functions.

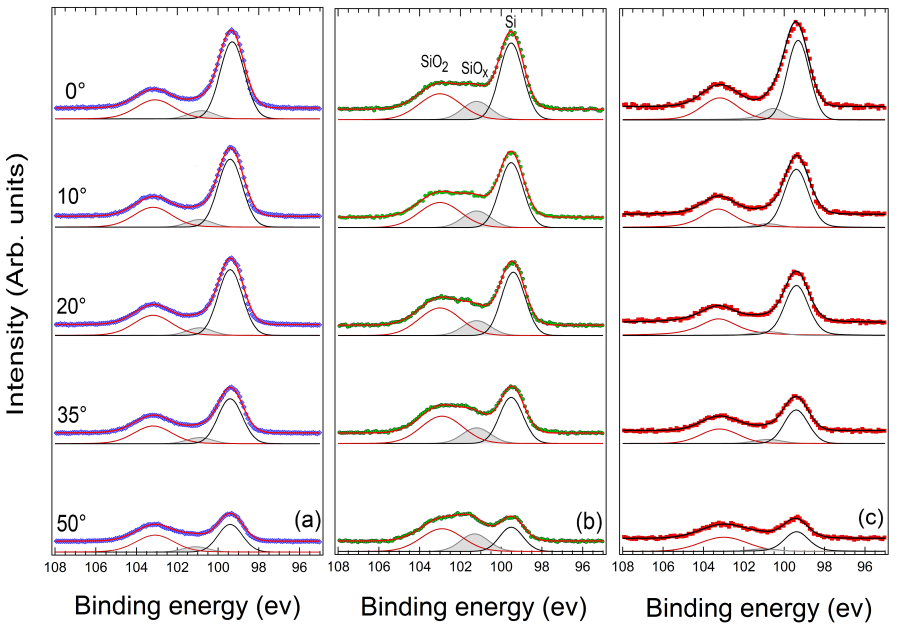

Figure 3.4: AR-XPS results for the silicon 2p peaks, normalized to C 1s intensity (left panel: sample A, central panel: sample B, right panel: sample C). The take-off angles ϑ (see Figure 3.2) between the normal to the surface and the detector vary between 0° and 50° and are reported on the left panel. The red component at high binding energy is ascribed to SiO_2, the midenergy, filled gray peak is ascribed to SiO_x, while the black component at low binding energy is ascribed to the bulk n-doped silicon.

It is important to observe that the SiO_x peak was not detected in the CNT-free substrate prior to the transfer of the CNT film (spectra not shown here), so its presence should be related to CNTs. The SiO_x layer may be in fact originated by the action of chemicals used to treat and transfer the CNT film or by a direct interaction between nanotubes and the native SiO_2 oxide layer. It is known [100] that, by pouring sulfur-based solutions (such as Piranha solution and SDS) on a silicon crystal, it is possible to obtain a layer of SiO_x. Piranha solution is a very strong oxidizer which first removes organic particles and contaminants

and then removes covalently adhered oxygen molecules, replacing them with hydrophilic OH molecules. On the other hand, because of strong van der Waals forces, upon CNT deposition, the oxygen atoms of SiO_2 can be pulled toward the nanotubes, yielding a thin layer of amorphous SiO_x. This passivation layer has a dangling bond defect density that is about 2 orders of magnitude higher than that of thermal oxides [101].

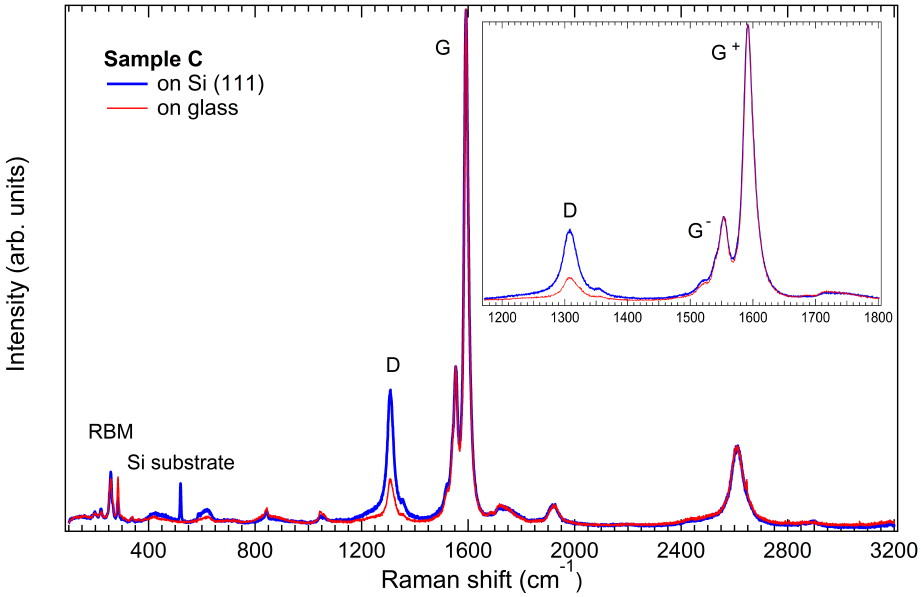

Figure 3.5: Raman spectra for sample C (thick blue line) and its counterpart on glass (thin red line). Inset: enlarged view of the spectral region where the D and G bands are detectable.

In order to test these assumptions, the CNTs used in the preparation of sample C have been also transferred on glass, and Raman spectroscopy measurements on these two samples have been carried out. The resulting spectra are shown in Figure 3.5. It is possible to discriminate the sample transferred on glass because of the absence of the characteristic first-order Raman line for a silicon crystal at 520 cm^{-1}. Since the CNTs transferred both on glass and

silicon are of the same type, the radial breathing modes are identical, but the D bands of these samples present a remarkable difference. In particular, sample C shows a more intense D-mode at 1310 cm^{-1}, when the spectra are normalized to the maximum of the G^+ band. This can be assumed as a proof of a higher density of defects when the CNTs are deposited on the (oxidized) silicon wafer. However, at this stage it is not possible to assess the origin of SiO_x, and we cannot exclude that the following causes can occur at the same time: (i) SDS is present in the CNT dispersion. Rinsing of the sample before the membrane filtration is expected to eliminate the SDS, but the XPS survey spectra showed that traces of S and Na are still detectable in the device. The formation of SiO_x could then be related (Ref. [100]) to the presence of residual SDS. (ii) On the other hand, the anchoring of CNTs on the SiO_2 layer can determine the formation of SiO_x (Ref [101]) and of the defects, detected by Raman spectroscopy, in the CNTs contacting the SiO_2 native oxide layer.

Global Fits of the AR-XPS Data. The interface modeling was carried out by considering a stack of layers with a non-uniform coverage on the topmost layers. For each takeoff angle ϑ, the area of all peaks (Si, SiO_x and SiO_2) contributing to the Si 2p spectral weight was considered, normalized to the C 1s peak area, and then processed using a dedicated software, based on algorithms written in the programming language of the IGOR Pro 6.3 software. After the chemical composition and the density of each layer are specified, the software calculates the DDF, and it is possible to create a layered model, initially guessing the layer thickness and the covering percentage (or island ratio). The fitting algorithm is therefore aimed to reproduce the experimental data (i.e., the peak intensity dependence on the takeoff angle ϑ), by using as fitting parameters all the thicknesses and the island ratio of the two topmost layers. The experimental data are compared in all steps of the fitting procedure with the expected intensities, calculated on the basis of the DDF function, the analyzer transmission, and the photoemission cross section. The fitting program then yields the estimated thickness of each layer as well as the island density in the CNT and SiO_x layers.

In order to model the sequence of layers at the interface, various attempts have been made, starting from models without island (Figure 3.6a) to models where the island also affects deeper layers (such as SiO_x, Figure 3.6c). For

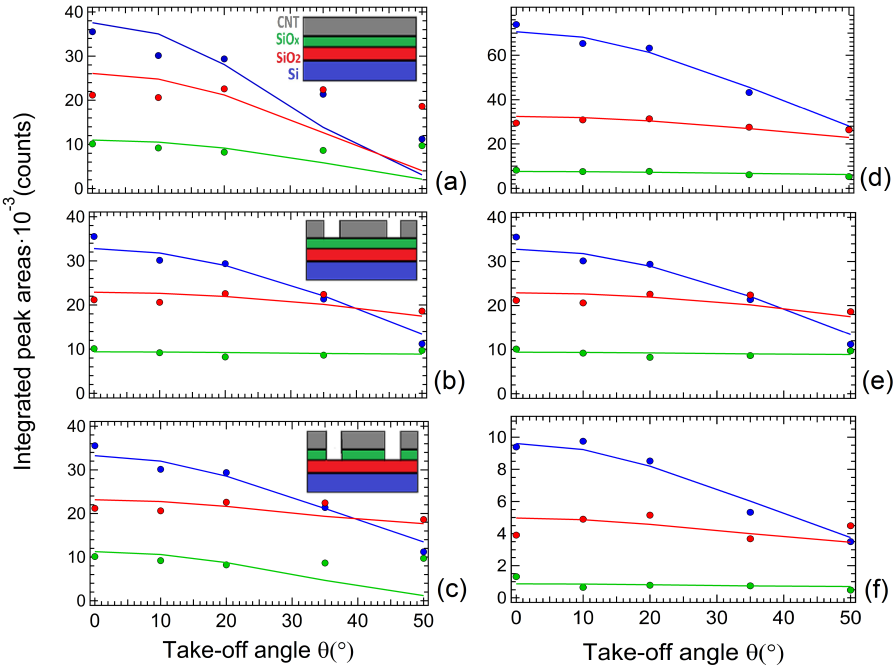

Figure 3.6: Dependence of the Si, SiO_2, and SiO_x XPS integrated peak areas on the takeoff angle ϑ. The lines are drawn according to the Global fit results, based on different models for the stacking of layers. Left panel: effects of the island distribution on the model output. The AR-XPS data are those extracted from the angle-resolved spectra of sample B. (a) No island; (b) islands only in the CNT film; (c) islands extended to the SiO_x layer. For all samples, the model that best matches the AR-XPS data is the second (b). Right panel: (d-f) AR-XPS data and global fit results for samples A, B, and C, with an island only in the CNT layer.

all samples, the best result (in terms of Chi-square) was obtained by assuming island only in the CNT topmost layer, as shown in Figure 3.6b. In particular, by comparing panels a and b, it is clear that the possibility to have an island in the topmost (i.e., CNT) layer yields an increase of the calculated intensities of the SiO_x and SiO_2 peaks at high takeoff angles. In turn, the addition of

an island in the SiO_x layer quenches too much the calculated intensity at high takeoff angles with respect to the measured angular dependence.

Sample	CNT (Å)	SiO_x (Å)	SiO_2 (Å)	island ratio (%)	SiO_x/SiO_2 (%)
A	254 ± 12	3.1 ± 0.4	13.9 ± 0.4	99.83 ± 0.02	23
B	346 ± 44	6.6 ± 0.4	19.1 ± 0.4	99.75 ± 0.02	35
C	360 ± 17	2.5 ± 0.7	15.1 ± 0.7	99.98 ± 0.01	17

Table 3.3: Results of the ARXPS Data Analysis Obtained by Modeling with a CNT-SiO_x-SiO_2-Si Multilayered Structure.

Finally, the best fitting results obtained for the three samples are shown in Figure 3.6d-f, while the thickness calculated for each layer is reported in Table 3.3. The first achievement of the ARXPS modeling is to show the possibility to estimate the overall thickness of the buried Si-O interface. In the present case, the thickness ranges from about 1.7 nm (sample A) to 2.6 nm (sample B). These values are those expected for the native oxide layer covering a silicon substrate, but they are different for the three samples, the thicker layer being that of sample B, while for the A and C samples the overall thickness is comparable. For each sample, the SiO_x/SiO_2 ratio is also different, and it is worth noting that the lowest SiO_x/SiO_2 ratio (17%) is shown by the device with highest efficiency (sample C), while for sample B, the least efficient of all, the ratio is the highest (35%). Finally, the thickness of the CNT layer is similar for the B and C samples, while it is lower in sample A, roughly scaling with the amount of CNT dispersion used to prepare the CNT layer. As stated in Chapter 1, the CNT film thickness appears to be one of the factors that affects the cell efficiency, but the present results show that the silicon oxide role is not negligible at all. In sample A, the SWCNTs are mostly metallic, but sample A shows a thinner oxide layer with respect to B, that in turn has been prepared with semiconducting SWCNTs. These factors might cooperate to provide the higher efficiency of A with respect to B. On the other hand, sample C displays the largest efficiency and an oxide layer comparable to sample A, though with a different SiO_x/SiO_2 ratio. Apparently, the 10-fold higher η of sample C can be related to a combination of advantageous parameters. First of all, sample C is characterized by being close to the CNT film thickness that is known to maximize the efficiency, as shown in a previous work [102]; moreover, in this

sample the CNT coverage results to be the most uniform, as the density of island is the lowest among the samples. Finally, in this sample the heterojunction formation could be favored by the amount of oxides. However, such a large difference in efficiency between samples B and C cannot be explained by focusing only on the CNT film characteristics and must be necessarily related to effects at the interface. In order to clarify the role played by the oxide in the device operation, we resorted to etch the oxide layer to track the oxidation of the interface by XPS and to monitor the cell efficiency by IV measurements.

Therefore, following Ref. [84], sample B was as first etched for 20 s in HF vapors in order to remove the oxide layers, and then left in air for about 300 h, to restore the native oxide layer. Any change of the electrical properties of the device was monitored through the acquisition of IV characteristics, and, in parallel, the Si 2p peak and C 1s were analyzed via XPS, in order to ensure that changes are due to the modulation of the thickness of the oxide layer and not to other effects, such as the acid doping of CNTs [103]. The effects of acid doping on CNTs are excluded at the present stage, as the line shape of the C 1s core level ascribed to the CNT contribution did not change upon etching and during the oxidation in air (not shown here). In turn, major changes were observed in the buried interface. In Figure 3.7a, the Si 2p peaks before (pink filled circles), immediately after (black filled diamonds), and 300 h after (blue filled triangle) the etching process are shown. It is easy to notice how the etching process acts on the oxide layer, removing the SiO_x and reducing the amount of SiO_2, inducing a change in the overall Si 2p lineshape. When the sample is left in air for 300 h, the SiO_x contribution did not show any detectable increase, while an oxidation of Si to SiO_2 is clearly observed. The combined effect of the etching and oxidation processes on the device operation is evident in Figure 3.7b, where the IV curves for all the three steps are shown. Before the etching, sample B was the one with the lowest efficiency and its IV characteristic is shown in Figure 3.7b (pink circles). After the oxide layer is removed through the etching process, the values of the electric parameters (V_{OC} and I_{SC}) decrease significantly and the cell performance deteriorates considerably (black diamonds). However, from the very first hours after the etching, an improvement of the IV curve is observed, till the cell reaches a stable behavior after a few tens of hours, staying constant up to 300 h (blue triangle). These results also demonstrate that the oxide layers, as well as the CNT film, should have an optimal thickness, necessary

to achieve high efficiencies. It is important to note that the change induced in the cell is effective, stable, and durable, disclosing the possibility to regenerate cells subjected for over one year to oxidation in air. It is important to remark that while the SiO_2 contribution increases, the SiO_x contribution does not show appreciable change up to 300 h after the etching, suggesting that SiO_x can be ascribed to one of the processing steps in the cell assembling. In this frame, SiO_x appears to influence the cell efficiency, and a first correlation, had been observed in Table 3 between the SiO_x/SiO_2 thickness ratio and the cell efficiency. With regard to the overall cell efficiency, we do not exclude that the optimal situation could be found in a suitable ratio between the thickness of the CNT film and of the SiO_2 layer, as the proper thickness of the SiO_2 layer may itself depend on the CNT thickness.

3.3 Conclusions

AR-XPS allowed us to carry-out a nondestructive profiling of a complex interface at the basis of a hybrid CNT/Si PV heterojunction. We have been able to directly probe that a chemically heterogeneous Si-O layer exists between the bulk Si n-type side of the junction and the p-type CNT layer. This layer is composed of SiO_2 and SiO_x, with a thickness in the 2-3 nm range. This proves and properly addresses early claims about the existence and the role of the silicon oxide in the PV cell [84]. The effects of the SiO layer on the junction efficiency are tracked by etching the junction in HF and collecting XPS and IV curves as the native oxide layer builds up. We show that etching removes the SiO_x layer and that the efficiency improves when a SiO_2 layer has regrown, due to spontaneous oxidation in air. Therefore, unlike what previously believed [103], SiO_2 acts as a buffer layer that improves the PV cell performances. Within the resolution of our XPS probe, HF etching does not appear to affect the CNT local electronic properties, excluding chemical doping of CNTs as the leading effect in the efficiency recovery after etching. In the present study, the silicon oxide buffer layer could be accessed by XPS provided that the CNT film thickness was not too high. This limited our choice to samples with a thickness of the CNT layers below about 40 nm. For several reasons, the efficiency of these cells is not high as compared to other samples reported in the literature. As first, the best performing cells we prepared with the present technique are those fabricated

with 4-5 mL of CNT dispersion. Second, comparison must be performed with devices like the present ones without any particular treatment (further p-type doping of CNTs and/or acid treatments), which have been reported to have efficiencies between 5% and 7%. With respect to these devices, all our samples are characterized by a lower short circuit current density and fill factor, thus yielding lower efficiencies. Both the low J_{SC} and FF values can be ascribed to too high series resistance, probably originating (1) from the presence of residual SDS surfactant (visible in the XPS spectrum through Na and S peaks), which, being an insulator, can increase the CNT film resistance, and, at a lower extent, (2) from the choice of a relatively high series resistance for the wafer. Finally, the contacts electrodes, based on silver paste, can be at the origin of additional resistances. Despite these limitations, the etching treatment yields a remarkable improvement of the fill factor (from 22% before etching to 36%, measured 300 h after the etching) and ultimately on the efficiency (from 0.2% to 0.35%) even in the low-efficiency cell (i.e., sample B), disclosing similar improvements for the best performing devices.

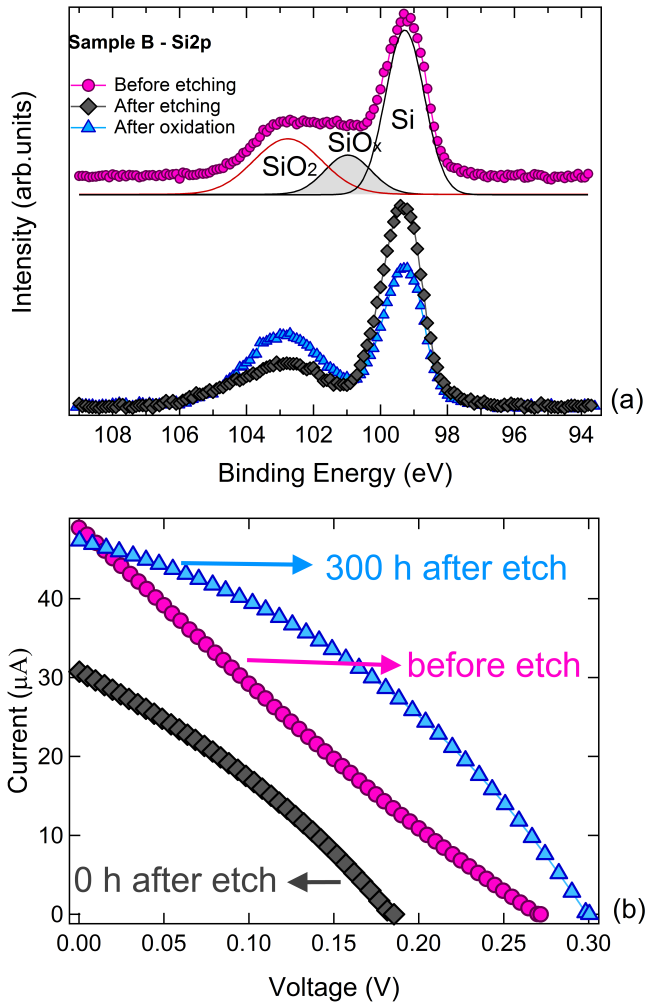

Figure 3.7: Etching effects on electronic and PV properties of sample B; the sample before the etching is represented with pink circles, after the etching with black diamonds, and after the oxidation with blue triangles. (a) Comparison between the XPS peaks of Si 2p, before and after the etching process and after 300 h of oxidation in air. It is possible to note how the chemical etching reduces the amount of oxides, inducing changes in the peak shape. (b) Effects of the variation of the oxide layer thickness on the IV characteristics.

Chapter 4

Effects of Acids Treatments on the Power Conversion Efficiency

A considerable effort has been recently made to increase the efficiency of CNT-Si heterojunctions, until reaching the record PCE of about 15% [52]. However, much has still to be done in order to identify the mechanisms behind the device operation and determine the parameters that mostly affect the cell behavior. In addition to a number of technical issues related to the cell geometry, to contacting pads, and to the choice of the CNT layer, several studies have pointed out [52, 84, 104, 105] that a silicon oxide layer grows at the interface between monocrystalline silicon and CNTs not only during the manufacturing process but also once the junction is built and that the properties of this layer may affect the overall cell performances. The role played by the oxide layer is of fundamental importance for understanding the working mechanism behind these devices that could behave either as p-n junctions [106] or as a metal-insulator-semiconductor (MIS) devices [107]. In particular, in a p-n junction model, the best efficiency should be reached once all the insulating silicon oxides are removed and perfect junctions between CNTs and Si can be built. On the other hand, in MIS junctions a relatively low potential barrier between

CNTs and silicon yields a high number of majority carriers recombinations, resulting in a saturation current larger than that of a p-n junction diode and, as a consequence, in a low open circuit voltage. In these devices a thin layer of insulating oxide is beneficial because it helps to confine electrons in silicon, avoiding them to fast recombine in CNTs [108]. Moreover, a thin insulating layer may also have the advantage to passivate interface states, hindering charge trapping, lowering recombinations and increasing the device open circuit voltage. The choice between the two junction schemes (i.e., p-n vs MIS) is still an open question that requires a specific investigation on the oxide role through direct evidence of the Si oxidation states during all the etching and ageing processes aimed to tailor the oxide layer properties. Oxide removal from silicon upon HF exposure is expected, as it is a standard treatment to etch silicon wafers and, on this basis, similar results have been claimed when CNT/Si heteojunctions were HF etched [105,109]. However, the results of the treatment are not usually documented by a probe sensitive to the Si oxidation state.

The possibility to access the buried interface layer by angle resolved X-ray photoemission spectroscopy (AR-XPS) has recently been demonstrated on devices similar to those analyzed in the present work [85]. Though the existence of an oxide layer with optimal thickness was inferred by several groups [84, 85, 105] to rationalize the behavior of the cells in the presence or absence of oxides, a complete analysis of this layer was so far overlooked and a direct evidence of the optimal layer thickness and composition is still virtually missing. Therefore, in spite of a seemingly straightforward preparation route, the CNT/SiO_x/Si interface represents a quite complex system from the point of view of materials, as it matches a relatively low density CNT bundle layer with a nanostructured and chemically inhomogeneous SiO_x layer grown on a n-doped silicon wafer. In particular, in devices based on bundles of randomly aligned SWCNTs the presence of a thin layer of oxides has always lead to better cell performances [84, 85, 105].

As shown by Jia *et al.* [84], the electrical parameters of a CNT/Si solar cell can be modulated by changing the thickness of the SiO_x layer, either by removing oxides with HF or by letting these oxides regrow, through either oxidation in ambient air or exposure to HNO_3. Since now, several groups [84, 105] have used exposure to HNO_3 to grow silicon oxides as a rapid alternative to ambient air oxidation, treating the two methods as if they would lead to equivalent

results. On the other hand, it is also well established that HNO_3 can be used to further p-dope the CNTs, [110–113] disclosing the possibility that HNO_3 does not merely act as an oxidant agent, but also as a chemical dopant. The 2-fold role of HNO_3 must be clarified and silicon oxidation and CNT doping processes need to be analyzed and discussed separately, with the help of suitable experimental techniques. Moreover, it is worth noting that efficient control of Si passivation through the introduction of a uniform and dense SiO_x layer is crucial to reduce leakage currents and to suppress charge recombination, in metal-oxide-semiconductor (MOS) devices, as shown by Kobayashi *et al.* [114] by considering nitric acid oxidation of silicon in conventional all-Si solar cells, as well as in Si/organic hybrid solar cells [115]. It is clear that a deeper understanding of the role played by acids in modifying the properties of CNTs, Si and SiO_x is mandatory. This can be accomplished by directly probing the changes of the physical and chemical properties of the surface and the buried interface through suitable spectroscopic tools.

The purpose of the present investigation [116] is then (i) to directly show on the device to which extent and how the hydrofluoric and nitric acid treatments affect the physical properties of both CNTs and the buried SiO_x interface and (ii) to probe how the CNT doping induced by HNO_3 exposure affects the overall cell behavior, discriminating effects on the CNT bundle layer from those due to changes in the physico-chemical properties of the oxide layer. To achieve these goals, a combination of spectroscopic tools has been considered: AR-XPS for a direct probe of the buried oxide interface, Raman spectroscopy to obtain information on CNT properties, and the acquisition of current density-voltage characteristics for monitoring the behavior of the photovoltaic device after exposure to acid. These techniques have been applied to the different steps of oxidation or acid exposure in order to obtain a real-time monitoring of the chemical and physical properties of the interface. Within this experimental frame, the HF etching resulted to be crucial to restore a common starting point between the samples in terms of interface oxide removal, directly and non-destructively documented by XPS analysis. It is worth mentioning that our HF treatments were milder than those carried out by Li *et al.* [109] that were able to n-dope their SWCNTs after a 5 min exposure to HF vapors. In this way it was possible to explore a junction between n-type CNT layer and a p-type silicon substrate, which is a reversed scheme with respect to the one discussed in the present

study (p-type CNT layer onto n-type Si wafer).

While in the previous chapter, the study of HF etching by ARXPS analysis was reported basically at a feasibility stage, here we fully exploit this approach to address several problems, spanning from the effects of HF etching to those of HNO_3 treatments and the tracking of spontaneous oxidation in air. This breadth of phenomena will be addressed by a combined spectroscopy study that goes beyond the usual characterization tools (transmission spectroscopy and sheet resistance measurements) aimed to monitor the effects of acid treatments. On the basis of this experimental approach, a clear correlation between the measured buried oxide layer thickness and the cell efficiency is demonstrated. Furthermore, the silicon oxide stoichiometry is also found to significantly affect the cell behavior. Finally, we have been able to show that, in the Si-CNT junction, HNO_3 behaves both as silicon oxidizing agent and a source of CNT chemical doping.

SWCNT/Si PV Devices. In this study, two PV cells belonging to the second series presented in section 2.4, hereafter in this chapter labelled A and B, were considered. The devices were realized by vacuum filtrating, respectively, 2 and 4 mL of semiconducting (7,6) CNTs, in solution with SDS. The layout of the device is shown in Figure 4.1a, while a cross section and the model stack of layers across the Si- CNT junction are shown in Figure 4.1b and c, respectively.

4.1 Results and Discussion

Effects of Exposure to HF: As devices were prepared in air, before starting any exposure to HF or HNO_3 it was necessary to record the initial cell efficiency through the acquisition of J-V curves on the pristine samples and to probe the silicon oxidation state with XPS at the pristine CNT-Si heterojunction (pink circles in Figure 4.2).

Incidentally, it is worth mentioning that the starting efficiency of our solar cells (0.035% and 0.147%, for samples A and B, respectively) are low if compared to those recently reported in literature [52, 84, 107, 111]. The cells were not optimized to yield the highest efficiencies, as the main focus was the detection of relative changes upon acid exposure. To access the SiO_x buried interface by AR-XPS, the CNT layer thickness is chosen to be relatively low. A similar choice

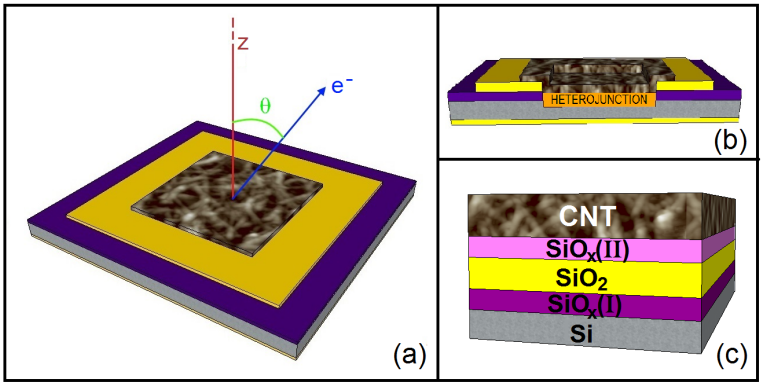

Figure 4.1: Three-dimensional sketch (a) and cross section (b) views of the CNTSi hybrid photovoltaic device. (c) Model of the complex buried interface as a stack of (bottom to top layer) $Si/SiO_x(I)/SiO_2/SiO_x(II)/CNT$ layers.

was also made by, for example, Tune *et al.* [105], that selected the devices not on the basis of their performances but, in that case, to guarantee the reproducibility of results. Moreover, these relatively low efficiencies are also determined by our experimental setup (halogen lamp, irradiance 64 mW/cm^2) which differs from the standard ones (solar simulator, 100 mW/cm^2) both in terms of power and spectral composition. However, this point would not affect the validity of our analysis, since we were looking for changes in the efficiency and in the electrical cell behavior by comparing different oxidation and doping states of the same sample.

XPS survey spectra collected on the pristine samples showed the presence of C, Si, and O, along with Na that was ascribed to traces of the CNT solution surfactant. High-resolution XPS studies on the Si oxidation [117–120], have shown that many oxide species can be detected during the oxidation process, each characterized by a specific binding energy (BE). In addition to bulk silicon (Si^0) the core lines of three suboxides (Si^{1+}, Si^{2+}, Si^{3+}) can be found in the binding energy range between Si and SiO_2. Even though our experimental resolution was lower than the one reached by using synchrotron radiation [117],

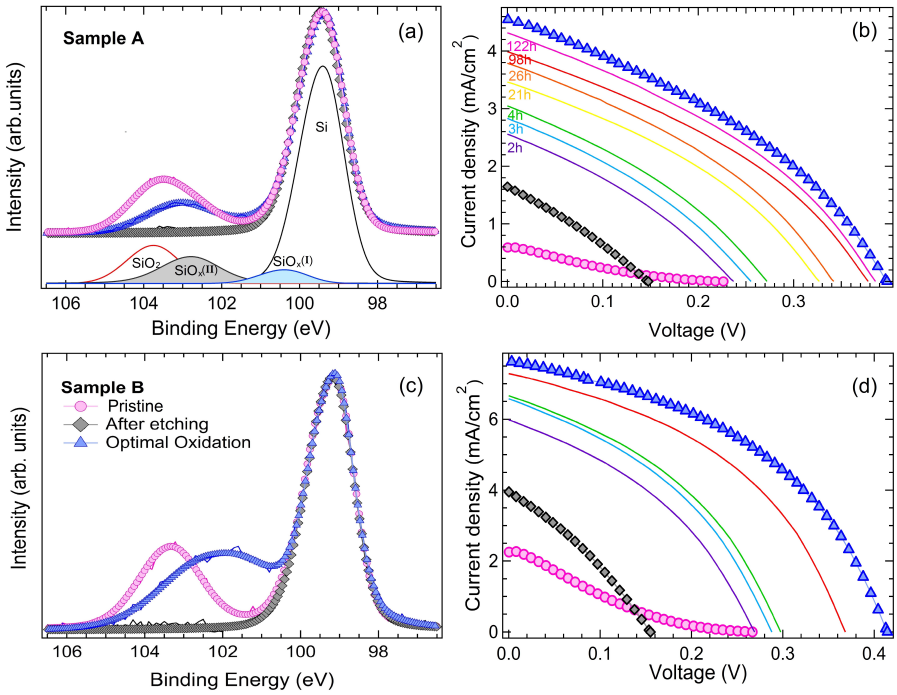

Figure 4.2: Three-dimensional sketch (a) and cross section (b) views of the CNTSi hybrid photovoltaic device. (c) Model of the complex buried interface as a stack of (bottom to top layer) Si/SiO_x(I)/SiO_2/SiO_x(II)/CNT layers.

in order to properly fit our spectra, we needed at least four peaks ranged from BE = 99.1 eV for bulk silicon to BE = 102.9 eV for SiO_2 with two additional peaks ascribed to non-stoichiometric silicon oxides. This choice was made necessary in particular for correctly fitting the Si 2p peak after the HF etching, where almost all the oxides were removed except for the Si^+ component, hereafter labelled as SiO_x(I), which determined an asymmetric line shape of the Si^0 peak. Since our experimental resolution does not allow to resolve the Si^{2+} and Si^{3+} contributions, they have been fit to a single peak and labelled as SiO_x(II).

Then, performing AR-XPS by varying the photoelectron takeoff angle ϑ

	η	FF	CNT	SiO_x(II)	SiO_2	SiO_x(I)	Total)
pristine	0.035	18.93	26.20	0.47	0.73	0.28	1.48
after HF	0.107	28.96	26.20	-	-	0.35	0.35
optimal	1.012	35.45	26.20	0.20	0.60	0.65	1.45

Table 4.1: Electrical Characteristics η and FF in (%) and Estimated Layer Thicknesses in (nm) of Sample A. Thickness values in silicon oxide layers are given with a ± 0.05 nm error.

	η	FF	CNT	SiO_x(II)	SiO_2	SiO_x(I)	Total)
pristine	0.147	17.91	31.41	0.24	1.72	0.55	2.51
after HF	0.295	31.88	31.41	-	-	0.64	0.64
optimal	2.297	48.28	31.41	0.72	1.23	0.36	2.31

Table 4.2: Electrical Characteristics η and FF in (%) and Estimated Layer Thicknesses in (nm) of Sample B. Thickness values in silicon oxide layers are given with a ± 0.05 nm error.

(Figure 4.1a), it was possible to evaluate the thickness of each layer composing our devices (Tables 4.1 and 4.2), following the method described in Ref. [85] and in Chapter 2. Based on this analysis, the four peaks have been ascribed to (i) bulk silicon (BE = 99.1 eV), (ii) non-stoichiometric silicon oxide (SiO_x(I)) (BE = 99.7 eV), which grows as a very thin layer on Si that eventually turns into SiO_2 during silicon oxidation process [117–120], (iii) stoichiometric SiO_2 (BE = 102.9 eV), and (iv) nonstoichiometric silicon oxide (SiO_x(II)) (BE = 101.3 eV), which lies between SiO_2 and the CNT layer, where oxygen atoms are likely shared between SiO_2 and the CNT bundles. The energetic preference for the CNT to bind on particular sites of an O-terminated SiO_2 surface has been predicted by M. Zubaer Hossain [121], indicating a significant interaction between oxygen from the SiO_x layer with CNT. The model stack of layer considered in the present study is depicted in Figure 4.1c.

After these characterizations, both samples were etched with HF vapors for 20 s to remove all silicon oxides, as confirmed by XPS analysis (Figure 4.2, black diamonds). Incidentally, we point out that our HF treatments have a different purpose as compared to those previously carried out by Li *et al.* [109]. In that

case, the etching was mainly addressed to remove oxygen from the tube walls and therefore to n-dope the CNTs, which in general are naturally p-doped in air due to O_2 adsorption. Therefore, a 5 min exposure in a vapor phase etcher was required to achieve n-doping. Then, samples had to be stored and analyzed into a nitrogen-filled glovebox to prevent nanotubes from coming into contact with oxygen, which would have p-doped the tubes again. On the other hand, our devices are based on p-doped CNTs so acid exposure and all measurements can be performed in air and a milder HF etching of 20 s is sufficient to remove silicon oxides without affecting the CNT doping. Even if samples were stored in the UHV analysis chamber just after the HF etching and the collection of the J-V curve, the time elapsed before reaching high vacuum conditions was enough to have the samples exposed to air and trigger the silicon oxidation. Indeed this process is known to be quite fast [118], and even just few minutes after etching the effects of oxidation are detectable, in the present case, as a small shoulder on the high BE side of the Si 2p core level. As a result, even after the oxides removal, a small quantity of SiO_x(I) is detected (Figure 4.2a and c). After the XPS analysis of the HF etched samples, the devices were exposed to air and the effects of oxidation were tracked through the J-V curves. The J-V curves in Figure 4.2b and d clearly highlight poor cell performances also in device without oxides (data collected immediately after the HF etching), but just after 2 h of oxidation in ambient air the efficiency starts to grow, following a rate very similar to the silicon oxidation rate at room temperature detected for silicon wafers, which is known to be quite fast in the first hours and then displaying a logarithmic-like growth rate) [118]. Selected J-V curves during the oxidation are shown in Figure 4.2b and d (thin lines), while the complete tracking of V_{OC}, J_{SC}, and η as a function of the oxidation time is shown in figures 4.3 and 4.4. About 1 week after HF etching (170 h), sample A and B reached their highest efficiency (1.01% and 2.30%, respectively), which is also assumed as the moment when the device has reached an optimal oxidation state (blue triangle in Figure 4.2). Through the AR-XPS analysis, we are now able for the first time to provide an estimation of the thickness of the silicon oxide layer yielding the best cell performances, as reported in Tables 4.1 and 4.2. At this stage two conclusions can be drawn. If we focus on the paths that lead sample A and B to their optimal oxidation states starting from the HF etching, which is assumed as the reference starting point, in both samples, an

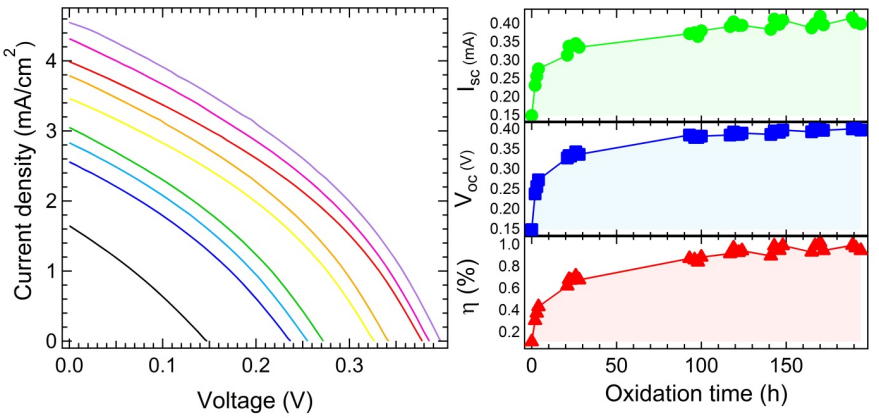

Figure 4.3: Left panel: Changes in the J-V characteristics during oxidation in air. Data were collected immediately after the HF etching (black curve, no silicon oxides) up to 175 hours (purple curve). Right panel: Short circuit current (I_{SC}) open circuit voltage (V_{SC}) and power conversion efficiency (η) dependence on oxidation time.

approximately 4- fold enhancement of the overall oxide layer thickness [SiO_x(II) + SiO_2 + SiO_x(I)/SiO_x(I)] is observed. Furthermore, even if the buried oxide layer thickness is comparable in the pristine and optimally oxidized samples, the chemical state of Si shows a clear change, as after optimal oxidation an increase of SiO_x and a reduction of SiO_2 is registered. On the other hand the lack of oxide (Figure 4.2, black diamonds) is detrimental to the performances of both cells, testifying an overall similar behavior.

These results induce to consider the oxide buried interface acting as a passivating/inversion layer in a MIS device. Oxides improve the cell performances by, on one side, avoiding trapping at silicon interface state and, on the other side, by reducing e-h pair recombination (see, e.g., ref [115]). This happens provided that silicon oxide thickness is kept below an optimal value, to prevent the detrimental effect of a large barrier to charge separation after the eh pair is created and to the hole photocurrent flow toward the CNT film. Referring to the Si-CNT hybrid cells, in principle, it should be easy to distinguish the two different junction models (i.e., p-n junction vs MIS). If the efficiency

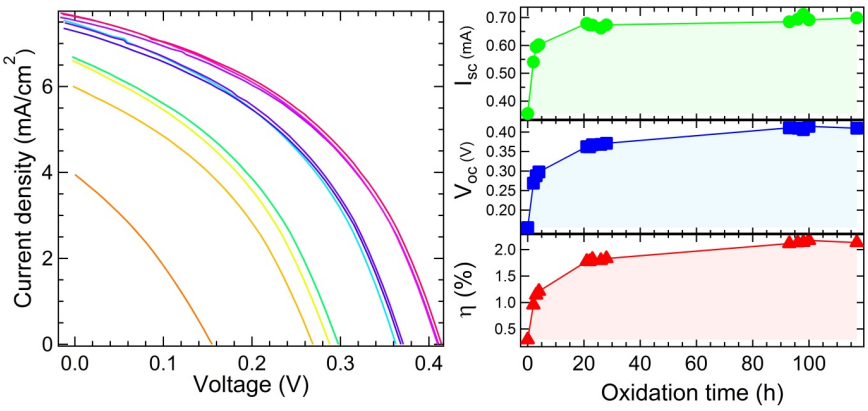

Figure 4.4: Sample B. Left panel: Changes in the J-V characteristics during oxidation in air. Right panel: I_{SC}, V_{SC} and η dependence on oxidation time.

grows when silicon oxides are completely removed by HF, the device can be modeled by a p-n junction, while if the device works better with a thin layer of Si oxides, the most suitable model is the MIS stack of layers. In literature, however, the role of the oxide layer in CNT/Si PV devices is an open matter of dispute [32, 52, 84, 85, 105–107, 111, 122], where the morphology of the CNT layer can play a relevant role. Evidence of devices working better with a thin layer of oxides (like MIS heterojunctions) are provided in the case of randomly aligned CNTs [84, 85, 105]. In fact, a perfect junction with silicon is hindered by the morphology of the CNT bundles, where only a relatively law number of CNTs is effectively in contact with the crystalline silicon underneath. When the amorphous silicon oxide grows, a higher number of heterojunctions is built up and the device efficiency improves. Finally, we noticed that J-V curves yielded the same results when measured after up to five HF etchings (20 s each), at least. Additional etches in some cases led to the degradation of the electrical contacts removing the SiO_2 insulating layer under the electrical contacts and yielding shorts between the electrodes and the n-type Si wafer. In addition, the XPS data were comparable both in terms of successful SiO_x removal and in terms of the Na content, that was not affected by HF etching (while being

affected by HNO_3 exposure, as shown in the next subsection).

Effects of Exposure to HNO3. As mentioned in the introductory remarks, HNO3 exposure is also often regarded as a tool to induce silicon oxidation but it may also lead to further p-doping of the CNT layer. To understand what ultimately affects cell performances, it is mandatory to discriminate these two effects separately, using AR-XPS measurements, performed in UHV, to monitor silicon oxidation, and Raman spectroscopy, and J-V characteristics, all performed in air, to highlight the eventual CNT doping. Since our two samples display a similar qualitative behavior, we resorted to analyze them separately, putting sample B in the UHV analysis chamber immediately after every acid treatment, to preserve it as much as possible from unwanted silicon oxidation occurring immediately after Si HF etching, and using sample A for the J-V measurements performed in air. Starting from the optimally oxidized samples, we restored a common initial condition by removing all oxides with HF (curves almost identical to those shown in Figure 4.2, black diamonds).

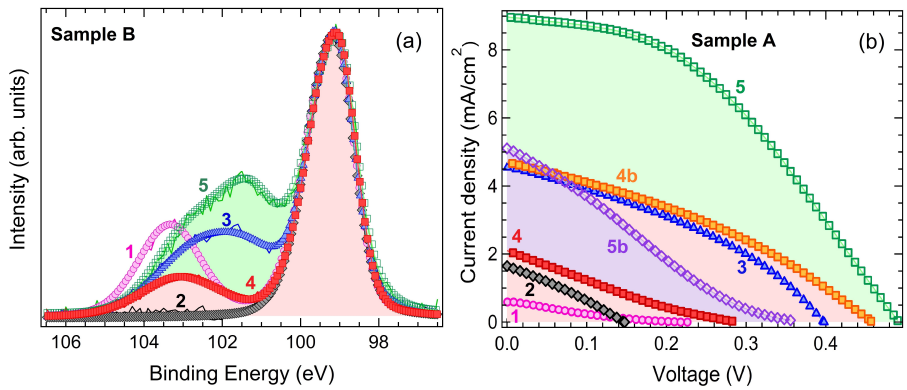

Figure 4.5: Sample B. Left panel: Changes in the J-V characteristics during oxidation in air. Right panel: I_{SC}, V_{SC} and η dependence on oxidation time.

Then, both samples were exposed to HNO_3 vapors at room temperature for 90 s, following the indications of Ref. [84]. The effects of nitric acid exposure were monitored through AR-XPS analysis on sample B (Figure 4.5a) and

through the J-V characteristics on sample A (Figure 4.5b).

	η (%)	FF (%)
HNO_3 vapors	0.197	20.52
optimal oxidation	1.163	34.29
HNO_3 liquid	2.866	41.69
after acid drying	0.651	22.99

Table 4.3: Efficiency and FF of HNO_3 Treatments of sample A

	CNT	SiO_x(II)	SiO_2	SiO_x(I)	Total)
HNO_3 vapors	31.41	0.29	0.83	0.52	1.64
HNO_3 liquid	31.41	0.79	1.54	1.18	3.51

Table 4.4: Thicknesses of Sample B Layers after HNO_3 Treatments

Efficiencies and FFs for sample A are reported in Table 4.3, while the silicon oxides thicknesses for sample B are listed in Table 4.4.

Immediately after the exposure to HNO_3, the device displays a slight increase of the efficiency (Table 4.3 and Figure 4.5b, curve 4 vs 2) but the oxidation state corresponding to the maximum η is reached only after leaving the device in air for 3 days (Table 4.3 and Figure 4.5, orange squares, curve 4b). As clearly shown by the Si 2p spectrum (curve 4, Figure 4.5) and in the results of the AR-XPS analysis (Table 4.4), this indicates that the silicon oxidation immediately after HNO_3 exposure (curve 4, Figure 4.5a) is not sufficient to yield the optimal oxidation state. After oxidation in air (curve 4b, Figure 4.5b), the maximum η is now slightly higher than the one reached without HNO_3 exposure (curve 3, triangles, in Figure 4.5b), giving a first suggestion of possible CNT doping. Since, at the present experimental conditions (T = 20 °C, exposure time 90 s, acid dilution 65%) only a low number of HNO_3 molecules effectively come into contact with CNT and Si, the nitric acid effects should be enhanced either by longer exposures or by directly wetting the devices with liquid HNO_3. We resorted to follow the second strategy: both samples were etched again with HF and immediately after etching a single drop of diluted HNO3 (65% RPE-ISO, Carlo Erba Reagents) was placed on the top of the CNT film. The result of

this last treatment (HNO_3 soaking) is a remarkable increase of the efficiency to 2.87%, two and a half times greater than the best value of 1.16% recorded with HNO_3 vapors (green empty squares in Figure 4.5 , curve 5). However, as the HNO_3 solution drop dries, 2 h after the treatment, the cell performances are found to worsen considerably (purple empty diamonds in Figure 4.5b, curve 5b), indicating that the initial jump of the efficiency is not only attributable to CNT p-doping alone but it can also be due (i) to a lensing effect by the acid droplet that focuses light on CNT surface [32], and (ii) to a formation of a temporary electrochemical cell between CNT and Si in the HNO_3 solution [111]. The rapid efficiency decrease from 2.87% to 0.65% recorded after the acid drying can be interpreted as an effect of the huge amount of silicon oxides, detrimental for the device operation, originated by the strong oxidizing effects of the HNO_3 drop as shown in Figure 4.5a (green empty squares, curve 5), which was previously counter-balanced by a favorable lensing-effect.

The conclusion we draw on this set of data is summarized in Figure 4.6 where a correlation between efficiency and oxide thickness is shown. The efficiency is measured on sample A, and not on sample B but in the two stages where the efficiency of both layers (η_A and η_B) was available the values measured for sample B were about 3 times the corresponding values for sample A ($\eta_B/\eta_A = 0.295/0.107$ after the first HF etching, $\eta_B/\eta_A = 1.55/0.49$ three months after the latest HNO_3 treatment). The effects of HNO_3 on the photovoltaic device are also evident in the XPS survey spectra, normalized to the C 1s intensity (Figure 4.7a).

In particular, before acid treatments, the percentage of oxygen present in the sample was 3.65%, which is almost doubled to 6.84% after exposure to HNO_3 vapors, and became five times higher after the soaking with HNO_3 drop, that is, 16.34% of the total probed area, indicating a clear oxidation induced by nitric acid. Furthermore, in all survey spectra, the Na 1s peak (as well as the Na Auger emission) ascribed to sodium dodecyl sulfate (SDS), the surfactant used to disperse the CNTs, resulted to be quenched by HNO_3, indicating a possible effect of surfactant removal. Another interesting consequence of HNO_3 vapor exposure is the shift of the C 1s peak to lower BE (inset of Figure 4.7b). This shift, not observed after HF etching, is a clear indicator of a Fermi level shift due to a hole doping of nanotubes. In the case of the HNO_3 drop, the C 1s peak shifts to low BE but also changes its shape in the high BE region, indicating an

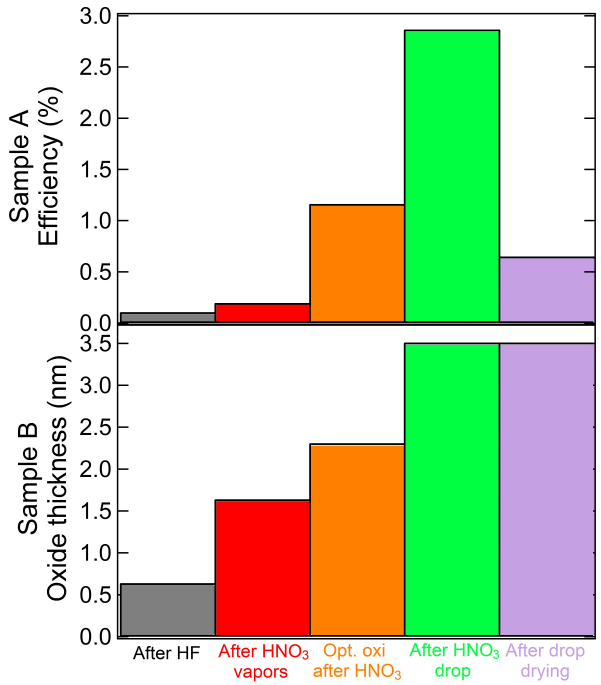

Figure 4.6: (Top panel) Efficiencies measured for sample A during various treatments of the cell. (Bottom panel) Overall oxide layer thickness for sample B.

increasing amount of oxygen bonded with the CNT carbon atoms [96]. These effects are more evident for the sample treated with liquid HNO_3, both because of the higher acid concentration and because HNO_3 in solution spends more time in contact with CNTs before evaporation, with respect to the gas phase.

To unambiguously prove the CNTs doping effect, we also collected Raman spectroscopy and optical absorption data. Raman spectroscopy is suitable to study fundamental tube properties, such as chirality, purity and defects [10]. In particular, in the presence of hole doping, the G^+-band of semiconducting SWCNT was found to move about 1 cm^{-1} toward higher wavenumbers [123].

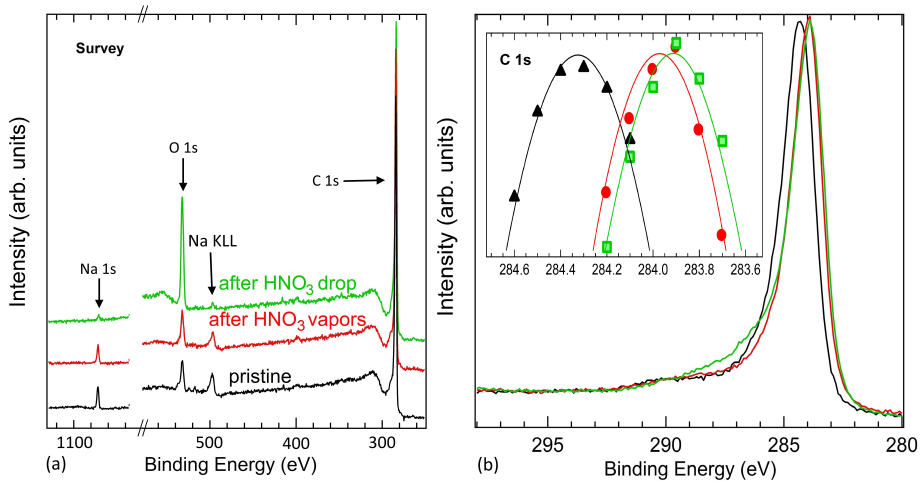

Figure 4.7: (a) Survey XPS spectra of sample B, normalized to the C 1s peak intensity. The C 1s, N 1s, and O 1s core levels are labelled, along with the Na Auger emission (b) C 1s spectra before and after acid treatment. Inset: Detail of the C 1s peak shift. Black line and triangles: Pristine sample. Red line and circles: After exposure to HNO_3 vapors. Green line and squares: After soaking with HNO_3 drop.

As shown in Figure 4.8 (left panel, sample A; right panel, sample B), while HF etching does not change the G^+-band position (1590.5 cm^{-1}), both gaseous and liquid HNO_3 exposures yield G^+ shifts of 0.9 and 1.8 cm^{-1}, respectively. This hole doping process is not completely reversible, because, even after a month in ambient air, sample B still presents a shift in the top of the G-band at 1591.4 cm^{-1}, which is less than the doped one (1592.3 cm^{-1}) but still far from the undoped value of 1590.5 cm^{-1}, as shown in Figure 4.8 (right panel). However, the CNT doping still observed one month after the HNO_3 exposure is not able to balance the detrimental effect on the cell efficiency of the thick oxide layer growth induced by the HNO_3 drop.

Optical spectroscopy data show, as expected [124], a quenching of the S_{11} and S_{22} bands upon HNO_3 exposure (Figure 4.9). These findings are also consistent with a decrease in the sheet resistance observed after HNO_3 exposure.

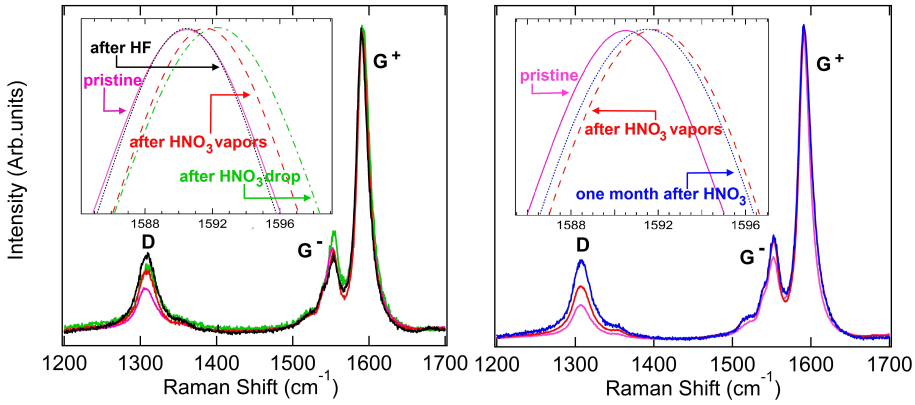

Figure 4.8: Raman spectra of D- and G-band of pristine (pink continuous line) sample A (left panel) and B (right panel), after HF (black dotted line), after HNO_3 vapors (red dashed curves), after HNO_3 drop (green dash-dotted line) and after one month from the acid treatments (blue dotted curve). The effect of HNO_3 doping is to shift the G^+ band toward higher Raman shifts as shown in the insets.

Indeed, starting from a base resistance of 10674 $\pm$ 12 ohm, the sheet resistance drops to 2470 $\pm$ 4 ohm after 10 s exposure and to 1834 $\pm$ 7 ohm with an additional 10 s exposure.

4.2 Conclusions

In conclusion, a spectroscopic investigation of the hybrid CNT-Si heterojunctions has been carried out with the aim to find a correlation between the physical and chemical properties of a buried oxide interface and the device performances. To this purpose, J-V tracking curves after each treatment were collected, to be matched with spectroscopic data from ARXPS and Raman probes. We have unambiguously demonstrated that, while a relatively mild HF etching does not change the CNT film properties, acting only as silicon oxides etcher, HNO_3 has the effect of both doping nanotubes and oxidizing the silicon underneath. This finding addresses a long-standing question on the CNT-Si hybrid junctions,

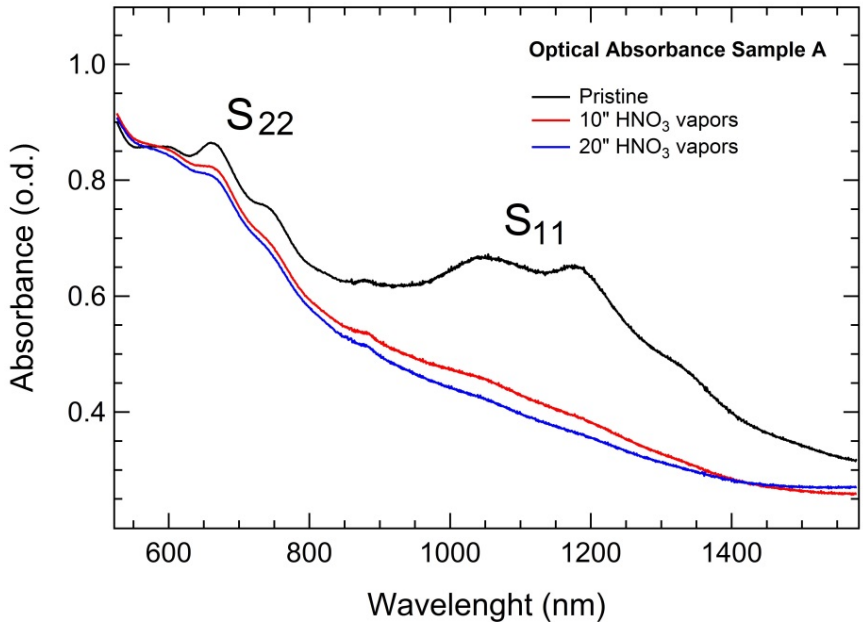

Figure 4.9: Optical absorbance of the pristine sample A (black curve), sample treated with HNO_3 vapors for 10 seconds (in red) and for 20 seconds (blue curve).

probing the role of the complex silicon oxide interface to tailor the PV cell performances and discriminating the effects of oxidation and p-doping which occur upon exposure to HNO_3. While a further p-doping of CNT is suitable to achieve higher efficiency, HNO_3 (especially in its liquid form) has to be used carefully because its strong oxidizing effect is detrimental to the cell performances, as it may yield a thickness of the oxide layer above the value (1.5-2.0 nm) recorded for the best performances of the PV cell. HF etching was used to remove Si oxide from the buried interface. This helped us establish a common starting point before carrying out any of the treatments considered in the present study. The build-up of an interface Si oxide layer is required to increase the efficiency. This is assumed as a strong indication that the junction can be described with a MIS model rather than a p-n junction. HF treatment was not strong enough

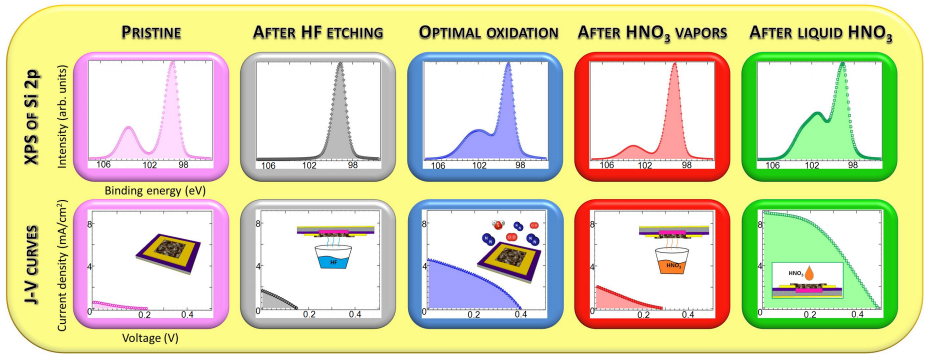

Figure 4.10: Graphical abstract for the effects of acid treatments on the efficiency of CNT/Si PV devices.

to n-dope the CNTs, as no change in the Raman and XPS spectra was observed upon HF exposure. HF etching did not affect the Na content of the CNT layer, unlike HNO_3 that was also able to etch Na away from the bundle layer.

The present results indicate that the SiO_x buried interface can be regarded as a passivating and inversion layer, which improves the cell performances by hindering the e-h pair recombination. Though these effects of the SiO_x interface in hybrid CNT-Si PV cells may have been unintentional in the original cell design, the thickness correlation with efficiency here demonstrated can provide a useful perspective in further device engineering.

Chapter 5

Charge Carriers Dynamics Investigations on High Efficiencies Solar Cells

In previous chapters has been shown that the efficiency of a CNT/Si solar cells can be easily modulated by modifying their building blocks through, for example, CNT doping, in particular with HNO_3, or by controlling the silicon oxidation at the buried interface level, removing oxides with HF etching and letting oxides regrow with natural oxidation in ambient air. Several experiments [85,116] have pointed out that a complex stack of thin layers of stoichiometric and non-stoichiometric silicon oxides (SiO_2 and SiO_x) can be found at the interface level, between bulk Si and CNT, in devices prepared and stored in air but the effect of the oxides layer is not yet been directly linked to devices electrical behavior. In fact, despite of a relatively simple architecture and manufacturing, understanding the physical operation of these devices is not trivial. Among the various open issues, the most controversial one concern the junction nature that could be either p-n like or metal-insulator-semiconductor. Previous studies have suggested that, in general, device behavior strictly depends on the geometry of the CNT thin film. In particular, for devices with a randomly aligned CNT film on top, an oxide interface layer with an optimal thickness is

needed to reach the best performances, but this behavior is not observed in the case of horizontally aligned CNT.

In order to understand how the dynamics of charge transfer processes at the interface, following photogeneration, can affect the cell behavior time-resolved pump-probe reflectivity measurement have been systematically carried out. This spectroscopy has revealed to be one of the most suitable techniques to study the dynamics of photogenerated carries in a wide range of CNT-related systems, from SWCNT, to MWCNT [125] and recently SWCNT-Si heterojunction [126], where ultrafast charge transfer occurring at the junction has been explored. Our aim is to find a correlation between the thickness of the buried SiO_x layer and the carrier photogeneration and transport, comparing I-V curves with the ultrafast behavior, analyzed by time-resolved reflectivity, in order to finally answer to the long standing question regarding the junction operation mechanism. A relatively slow dynamics (with a characteristic time τ_2) is identified, which scales with the cell efficiency η, showing how the growth of an oxide layer directly affects the charge dynamics.

Optical measurements: Time-resolved reflectivity measurements have been carried out in a variable-pump and fixed-probe configuration by using a 1 kHz amplified Ti:sapphire laser system, delivering 0.5 mJ, 150 fs, 1.55 eV light pulses together with a light conversion traveling wave optical parametric amplifier (TOPAS), generating laser pulses of 150 fs, with selectable photon energies in the 0.75-1.07 eV range. While the probe photon energy is fixed at 1.55 eV, two different pump energies have been used: the first is directly selected with the TOPAS in the infrared (IR) region at 0.935 eV, while the second was generated by doubling the TOPAS output with a BBO nonlinear optical crystal for second harmonic generation, leading to pump pulses in the visible (Vis) region at 1.87 eV. The experimental resolution is $\Delta R/R = 10^{-4}$.

5.1 Results and discussions on a first series solar cell

Since previous studies on similar devices [126, 128] have shown that decoupling the complex transient reflectivity (TR) signal is a tough task, preliminary

measurements have been carried out on *ad hoc* samples, before considering the high efficiency solar cells.

Firstly, in order to discriminate effects related to silicon from those due to only CNTs, we performed time-resolved reflectivity measurements not only on a solar cell but also on a reference sample obtained by depositing an identical CNT film on a glass slide, in which no Si/CNT junctions are present. To further discriminate signals, two different pump wavelengths (1326 nm and 663 nm, hereafter denoted as IR and Vis, respectively) had been used. In the IR, the pump photon energy of ∼0.9 eV (1326 nm) is not sufficient to excite carriers in silicon so all the signal can be in first approximation ascribed to CNTs. On the other hand, when the pump is set in the Vis region, with a photon energy of ∼1.8 eV (663 nm) larger than the Si gap, it is possible to photoexcite carriers also in the Si wafer and/or at the CNT/Si interface, i.e. at the heterojunction enabling the cell operation mechanism. At this wavelength and fluence, however, the TR signal coming from the bare silicon is negligible.

Finally, the first set of measurements have been carried out an the 5.5 ml metallic solar cell, belonging to the first series (see section 2.4 for details), since the same sample had been already characterized in Ref. [126] and the different dynamics composing its transient reflectivity signal revealed to be easier to deconvolve.

In Figure 5.1, the transient reflectivity signal (ΔR), normalized to the value of the static reflectivity R, for different oxidation time, has been collected. Starting from a very oxidized sample (black curve in Fig.5.1), stored in air for several months, the device was exposed for 20 seconds to HF vapors at room temperature to etch silicon oxides (red line) and then it was left in ambient air for several days to oxidize. During this oxidation process, the cell behavior was tracked both in terms of I-V curves, and time resolved reflectivity measurements. The first remarkable thing to note is that the IR signal, related only to charge relaxation into CNTs, does not change with the Si oxidation, remaining almost identical to the one displayed by the reference sample (in blue in Fig. 5.1). The transient signal is negative, due to a photobleaching channel, as expected for CNT [129–131], with a very fast dynamics (within 1 ps).

Therefore, for evaluating the effect of the interface on both the cell efficiency and the transient reflectivity, only the data collected through the Vis pump can be helpful. In CNT-related systems, [129–131] this signal is usually fitted with

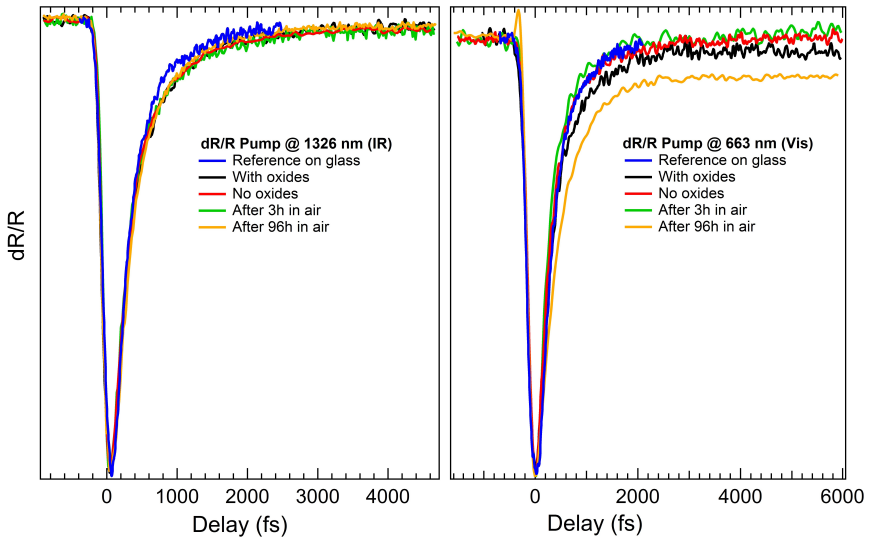

Figure 5.1: Time-resolved IR (a) and Vis (b) reflectivity signal for reference glass sample (in blue) and PV devices. The evolution of the interface oxides layer has been followed, starting from a very oxidized sample (in black), after oxides removal (red line), 3 hours after HF etching (in green) and after 96 hours of oxidation in ambient air (in orange).

a convolution of two exponential curves, accounting for two different relaxation dynamics, namely τ_1 faster and more intense (in blue in figure 5.2), and τ_2 slower and less intense (yellow peak in figure 5.2). While the first dynamics is the same on both the reference sample and on the cell suggesting that it is due to the CNT response, the second is present only on the cell response and strongly depends on the oxidation process.

In Figure 5.3, the ΔR/R signals obtained by exciting the cell in the Vis regime, for different oxidation times, are directly compared to their corresponding I-V curves. When the sample is highly oxidized, as well as all oxides are removed with HF vapors, the device performs poorly, displaying an efficiency of 0.41% and 0.23% and a FF of 22.2% and 20.5%, respectively.

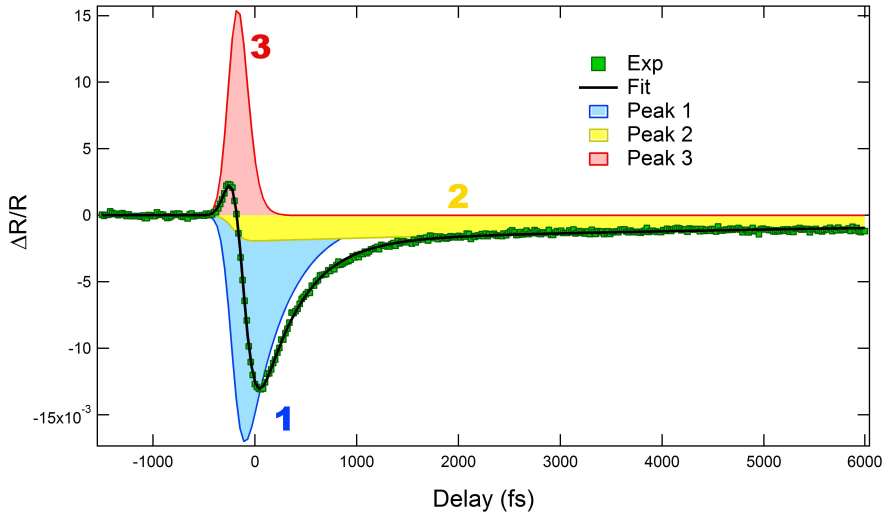

Figure 5.2: An example of the deconvolution of the three peaks used to fit the complex Vis dynamics.

As the PV device is left in air, oxygen molecules reach the silicon below CNTs and contribute to create a complex stack of stoichiometric and non-stoichiometric silicon oxides, already reported in Ref. [85] and studied in detail in Ref. [116]. This thin layer of oxides is necessary to steadily improve performances, until reaching the best electrical behavior after 120 hours in air (η=2.64% and FF=49.6%). Excess of oxides, that can be obtained either through a long ageing (storage) in air or through exposure to HNO_3, are detrimental to efficiency [116].

Interestingly, when the solar cell is close to its maximum efficiency state, a third dynamics appear (red peak in figure 5.2). This dynamics, which appears only in the visible range and is absent in the glass reference, is characterized by being very fast (i.e. within the laser pulsewidht of 150 fs) and positive. In carbon nanotubes, a positive signal is related to a photoabsorption (PA) and can be related to an intra-band transition due to a strong tube-tube interaction [127], but in this case, tube-tube interaction does not change during the

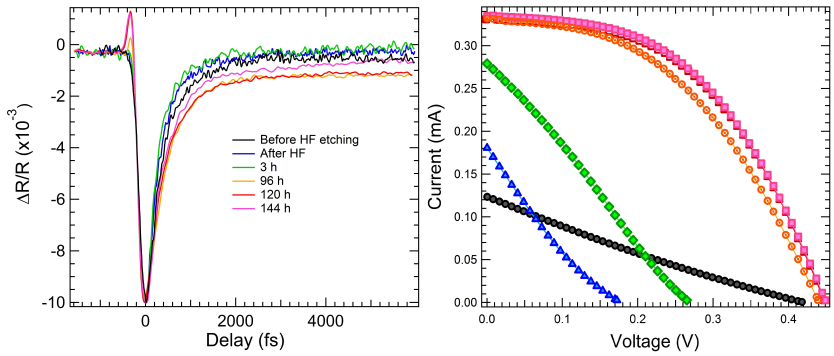

Figure 5.3: Transient reflectivity (a) and I-V curves (b) of a PV device with different oxides layer. Starting from a oxidized sample (black), oxides are removed through HF (blue) and then the sample is left in air for 3 (green), 96 (orange), 120 (red) and 144 (pink) hours, respectively.

oxidation process. Even if the origin of this positive peak is not completely clear, at this stage it can be tentatively attributed to the growth of the amorphous silicon oxide which contributes to improve connections between the randomly aligned SWCNTs. Even the second dynamics in Fig. 5.3a follows the device performance, being longest when the efficiency reaches its maximum value. As reported by Ponzoni *et al.* [126], the second dynamics has to be ascribed to the interface. When, in fact, the photon energy is able to excite carriers in the Si wafer a hole transfer process driven by the built-in heterojunction potential takes place from Si to CNT giving rise to the second dynamics.

This result is confirmed by Figure 5.4 where the cell electrical parameters (I_{SC}, V_{OC}, η and FF) and τ_2 are plotted versus the oxidation time, before and after the HF etching. From Figure 5.4 it is possible to observe that I_{SC} and V_{OC} display different trends during the oxidation process. In particular, I_{SC} is very low before the etching and grows extremely rapidly with oxidation, becoming three times larger than its initial value in one day, indicating a fast increasing of the number of carriers. On the other hand, V_{OC} is already high at the starting point, sharply decrease with the HF etching and then regrows slower than the I_{SC}. Here, τ_2 seems to follow the behavior of the I_{SC} confirming

that this second dynamics is a fingerprint of the quality of the interface. This dynamics cannot be related to silicon alone because, as reported by Ponzoni *et al.* [126], the Si absorption is almost negligible at this wavelength but cannot also be attributed to CNTs alone, because it is absent in the IR signal. This elongation of the second dynamics τ_2 must be interpreted as a fingerprint of changing in charges transferred at the interface level. In general, because the decay constant τ of an exponential relaxation can be interpreted as an inverse of a probability, a τ increase can be related with a probability reduction. In our case, a longer second dynamics is accompanied with an increase of the power conversion efficiency, indicating that the processes becoming less probable are the ones usually unfavorable to the solar cell operation mechanism. This scenario is compatible with a MIS junction, in which an optimal thickness of the oxide interface layer is necessary to raise the potential barrier, reducing recombinations and favoring the tunneling of carriers across the junction.

5.2 First partial conclusion

With this preliminary pump-probe investigation we have been able for the first time to put in direct correlation the cell electrical parameter with the ultrafast relaxation charge transfer at the interface level. Moreover, by interpreting the correlation between τ_2 elongation and efficiency enhancement as a reduction of the charge recombination probability, we have been finally able to show that the oxide layer plays an important role in changing the interface dynamics.

5.3 High η solar cells characterization.

The findings presented in previous chapters, together with the improved CNT dispersion and deposition techniques presented in section 2.4, have led to the high efficiencies in all the third series devices. The best performing sample reached the maximum efficiency of 12.2% (J-V curve reported in Fig.2.21), measured under a standard solar simulator (100 mW/cm^2 AM 1.5) and the reasons of this outstanding performance will be discussed and analyzed in this section.

A preliminary XPS analysis of the third series solar cell is presented in the blue survey spectrum in Fig.5.5(a). Here, only the O 1s, C 1s and Si 2p peaks are detectable. Comparing this spectrum with the ones collected from previous samples (See 4.7, for example), it is possible to note the first effect of the new CNT preparation routine. In this case, in fact, the Na 1s and its Auger peaks are not detected, testifying that the surfactant removal is now more effective, since only SDS can be identified as the source of sodium. This can be seen as the first fingerprint of a cleaner CNT layer which led to a higher film conductivity.

At this point, on the basis of the results already obtained for the 5.5 ml sample, we performed transient reflectivity measurements, only in the visible range, for the new 2 ml solar cell. Its surface had been firstly exposed to hydrofluoric acid vapors for 20 seconds, than its oxidation in ambient air has been followed both with TR and I-V measurements. In figure 5.6, a comparison between the glass reference sample, the solar cell immediately after HF and at its optimal oxidation state is reported while the electrical measurements are presented in figure 5.7.

By comparing the TR signal from the reference sample to those of the solar cell it is possible to confirm the trend observed in the previous section. Here, it is clear that not only the second but also the third dynamics are related to an interaction between CNTs and silicon, since they are respectively different and absent in the reference glass sample. The second dynamics has already been attributed to a decrease of recombinations at the interface level, now we can also try to assign the third peak. This dynamics, in fact, is already intense after HF etching (figure 5.8), if compared to the one displayed by the 5.5 ml sample. Then it grows with silicon oxides and reaches its maximum at the optimal oxidation state (figure 5.9). Thus, this third positive dynamics could tentatively be attributable to a transfer of carriers from silicon and CNTs at the

interface level, which, in randomly aligned nanotubes is favored by the oxide mediation.

Now, the reasons why this cell displays such a high power conversion efficiency will be discussed, by means of the analysis of I-V characteristic collected with the custom-made J-V tracker, shown in Figure 5.7. This solar cell immediately displays a high I_{SC} from the beginning, which continuously grows with oxidation, eventually sending in saturation our set-up near the optimal oxidation state (blue squares in Fig. 5.7). After the HF removal, the sample η measured with our set-up (irradiance 64 mW/cm^2) had an efficiency of 0.28%, which exceeds the limit of 6% at the saturation point.

Interestingly, in this case, the optimal oxidation state is reached after only 46 hours in ambient air, instead of the $\simeq$150 hours taken by other samples. This happens because, in previous cells, surfactant surrounded nanotubes, hindering carbon oxidation. In the third-series CNT films, the SDS is removed more efficiently, improving the conductivity but leaving the uncovered nanotube sidewalls free to oxidize. This assumption is confirmed by comparing the C 1s spectra before and after HF etching, as shown in Figure 5.5 (b). In this case, the HF treatment causes a change in shape of the C 1s spectrum, not recorded in previous samples. It is probable that the surfactant removal makes easier for oxygen molecules to reach the buried interface and to oxidize silicon. In Figure 5.5(c) a comparison between the Si 2p spectra before and after HF etching, confirms that, in order to reach the highest efficiency, a change of spectral weight from SiO_2 to SiO_x is needed, as already evidenced in Chapter 4.

Finally, the stability in time of the third series cells electrical parameters have been studied. To overcome the problem of set-up saturation, the irradiance on the 2 ml solar cell has been lowered from 64 to 46 mW/cm^2 and another solar cell, always belonging to the third series but made of multiwall carbon nanotubes, has been considered.

In Figure 5.10, the I-V curves, V_{OC}, I_{SC} and η *versus* the oxidation time (i.e. the time in which the cell is left in air) for the 2 ml solar cell, with SWCNTs and a lowered irradiance, are presented. While the V_{OC} remains almost stable during the considered time slot (96 hours, four days), I_{SC} varies also within the same day, affected by external factors such as air humidity and temperature.

The J-V curves and electrical parameters of the MWCNTs PV devices *versus* the oxidation time are reported in figure 5.11. The evolution of this cell has

been followed for more than two weeks (up to 362 hours) and this permitted to evaluate that, on a longer time-scale, even the I_{SC} reaches a stability condition, which is more or less the same than the starting point.

5.4 Second partial conclusion

In conclusion, by TR measurements on the best performing SWCNT third series PV device, it has been possible to better analyze the third dynamics which clearly depends on the efficiency and on the oxidation at the interface. Two different physical processes can justify this quite fast photoabsorption: a charge transfer at the interface and/or possible interface states. To clarify this point, theoretical calculations of the electronic properties of the CNT/Si interface, along with TR measurements at different visible wavelength (possibly with a supercontinuum set-up), are needed.

The factors which have led to the huge jump in the efficiency recorded for the third series solar cells can be identified with the ability to get cleaner and more conductive CNTs film, thanks to SDS removal. The study of the MWCNT PV devices on the long time-scale of two weeks allows us to conclude that this solar cells show their best performances earlier than the ones of the previous series (46 hours instead of 140 hours). However, this high efficiency state does not last but both the V_{OC} and the I_{SC} decrease in time (even if with different rate), until a stability condition is reached.

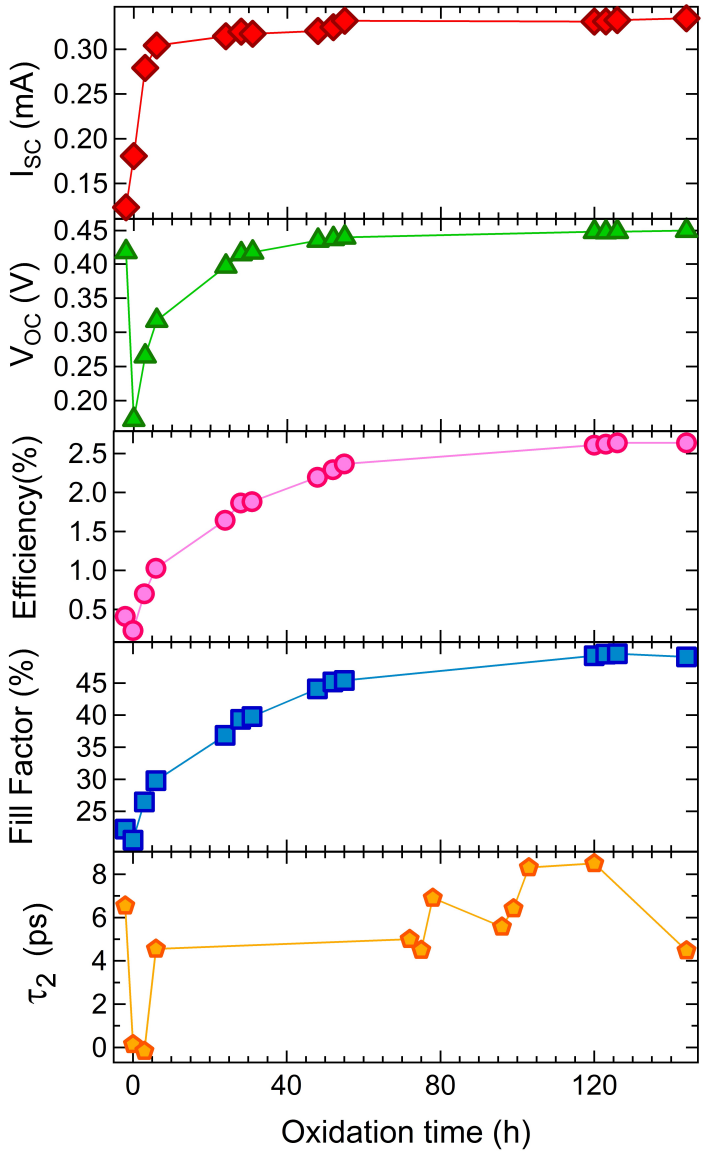

Figure 5.4: Electrical solar cell parameter (I_{SC}, V_{OC}, η and FF) compared to the transient reflectivity second dynamics τ_2 of the 5.5 ml metallic cell.

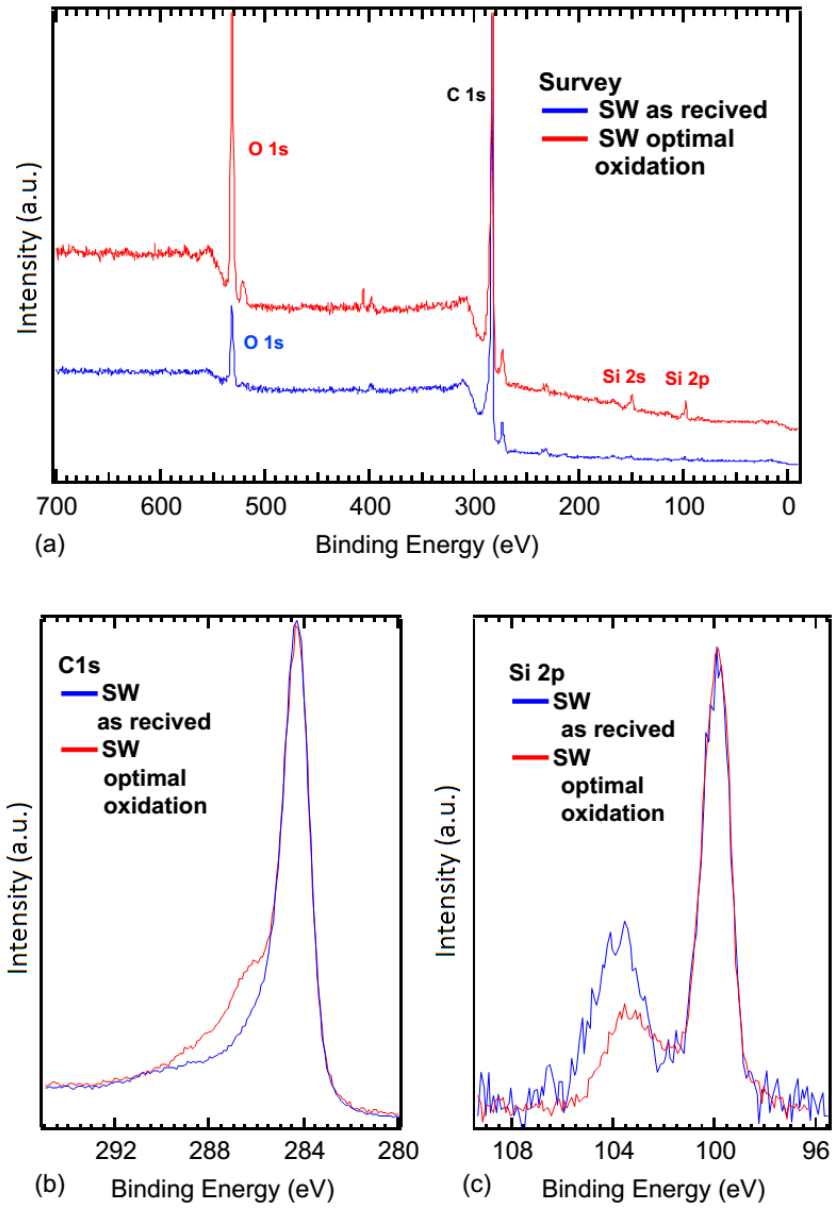

Figure 5.5: XPS survey (a), C 1s and Si 2p spectra of the high efficiency sample as received (in blue) and at its optimal oxidation state (in red).

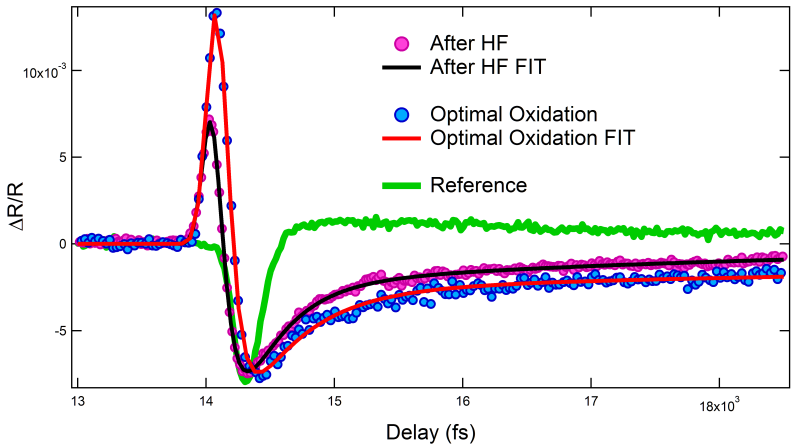

Figure 5.6: Comparison between the transient reflectivity signal of: the glass reference sample (in green), solar cell after HF (in black) and at its optimal oxidation state (in red), in the visible range.

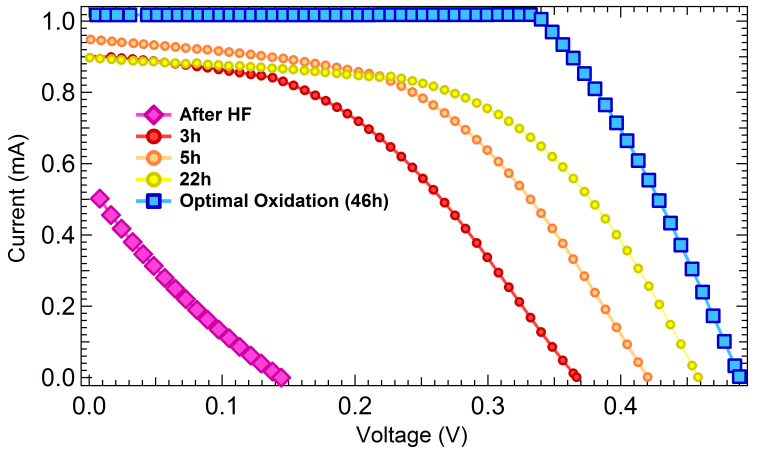

Figure 5.7: I-V curves for the 2ml solar cell after HF etching (pink diamond) and as a function of oxidation time, until the optimal oxidation state (blue squares).

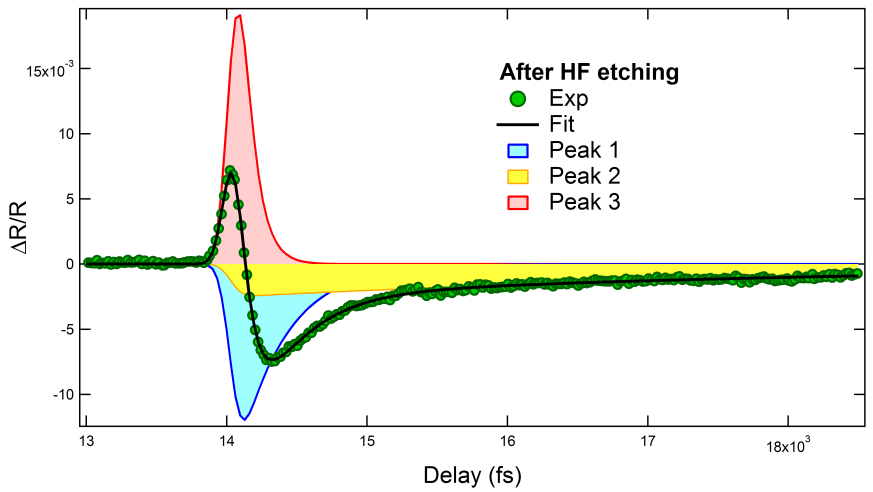

Figure 5.8: TR measurement after HF etching in which the first (in blue), the second (in yellow) and the third dynamics (in red) are deconvolved.

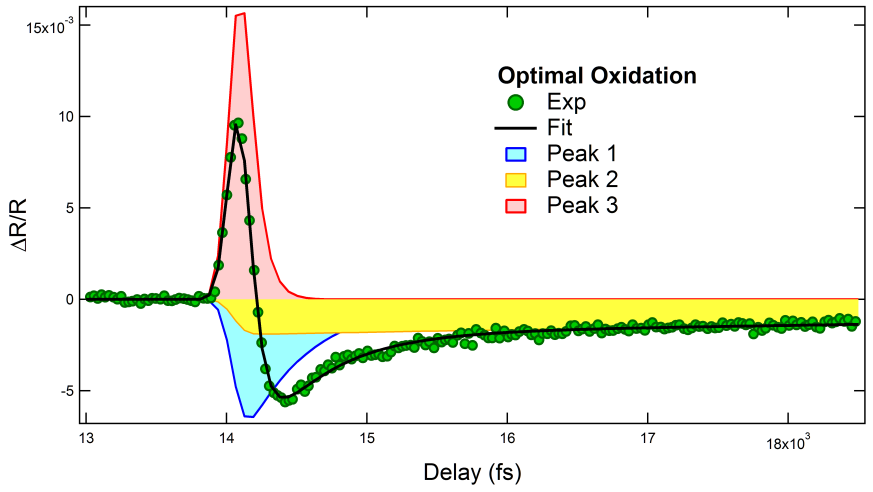

Figure 5.9: TR measurement at the optimal oxidation state in which the first (in blue), the second (in yellow) and the third dynamics (in red) are deconvolved.

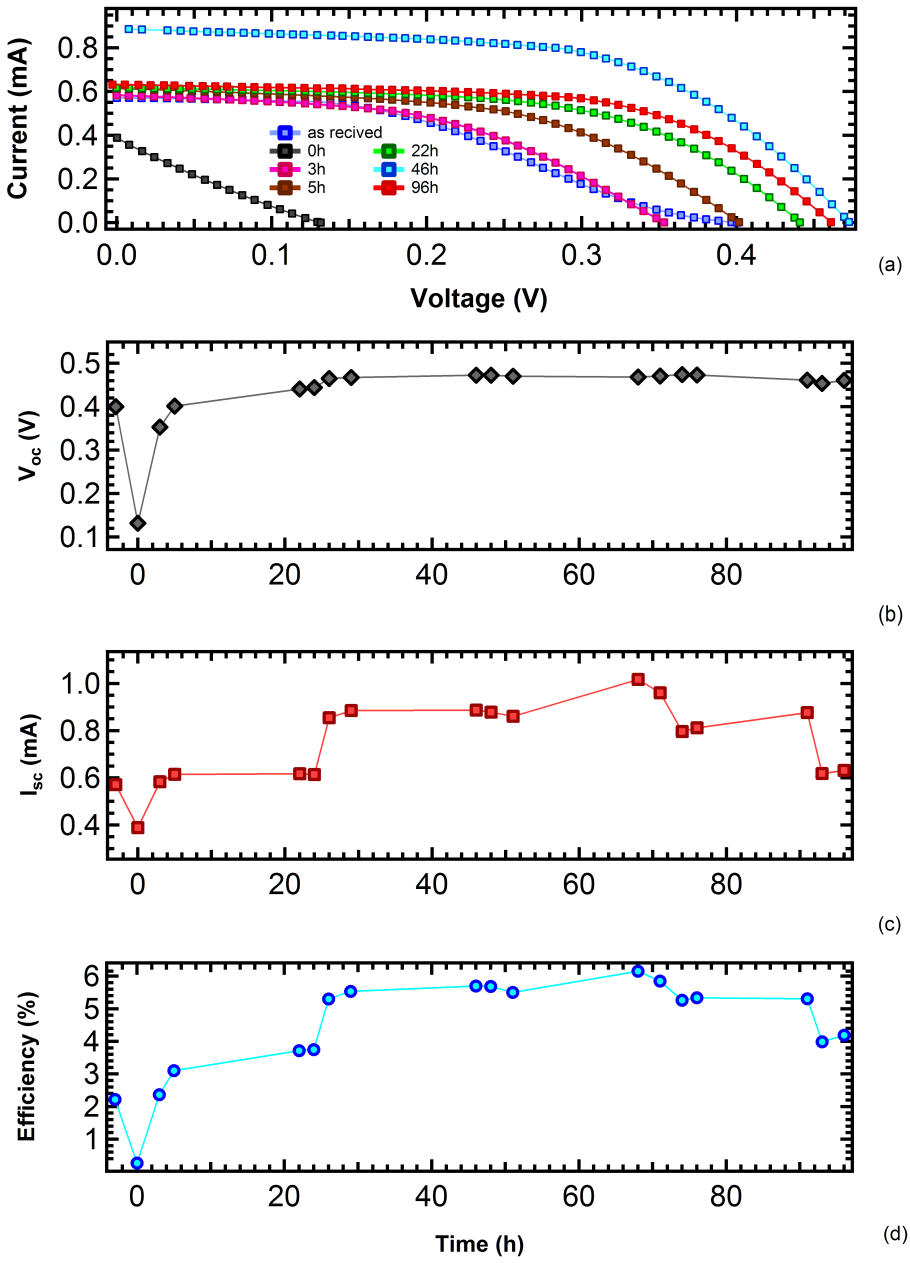

Figure 5.10: I-V curves, V_{OC}, I_{SC} and η *vs* oxidation time of the 2ml solar cell.

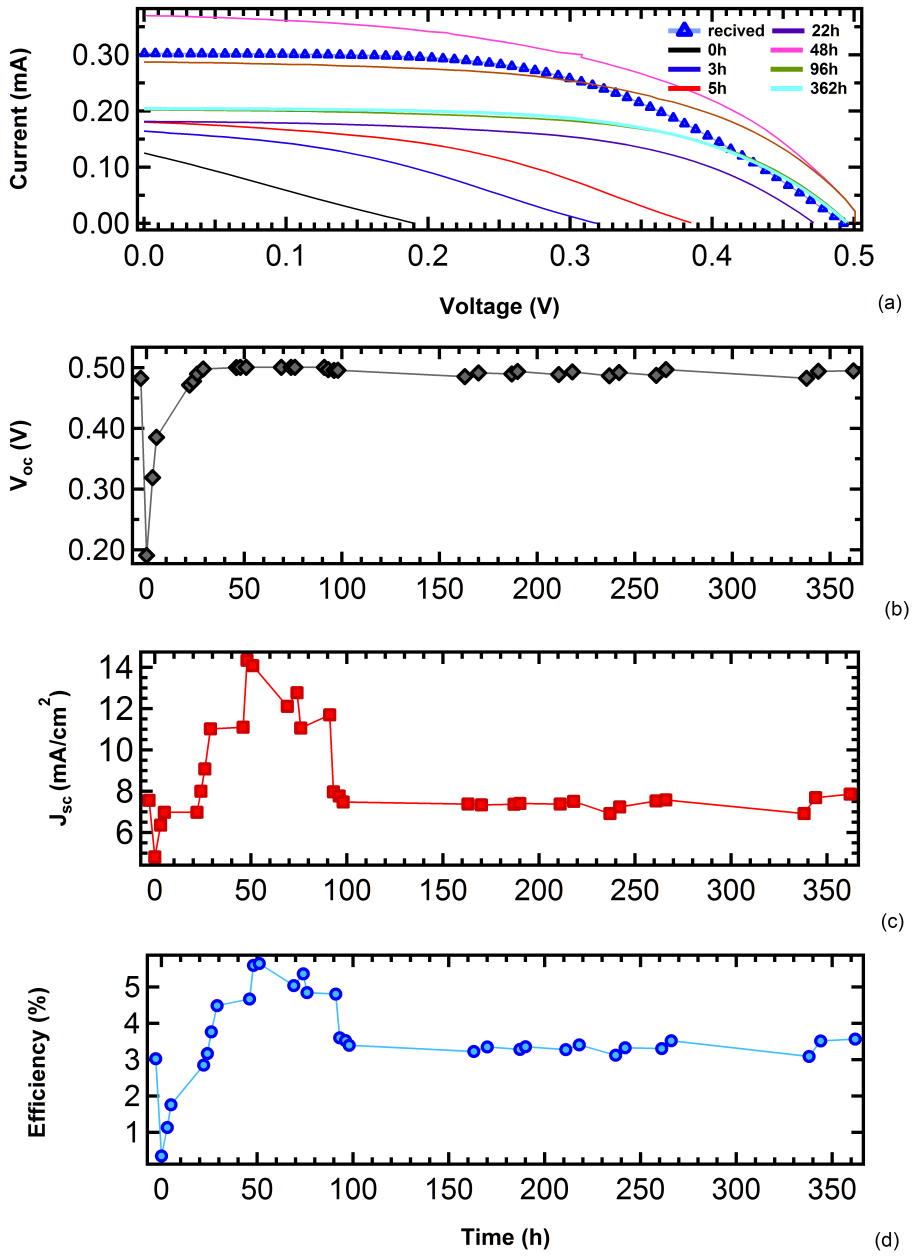

Figure 5.11: J-V curves, V_{OC}, I_{SC} and η *vs* oxidation time of the third series MWCNT PV devices. The evolution of this cell has been followed for more than two weeks.

Appendix A

Solar Cells

A solar cell (also called a photovoltaic cell) is an electrical device that converts the energy of light directly into electricity by the photovoltaic effect. It is a form of photoelectric cell (in that its electrical characteristics, e.g. current, voltage, or resistance, vary when light is incident upon it) which, when exposed to light, can generate and support an electric current without being attached to any external voltage source. The term *photovoltaic* comes from the Greek *phõs* meaning "light", and from $Volt$, the unit of electro-motive force, which in turn comes from the last name of the Italian physicist Alessandro Volta. The term *photovoltaic* has been in use since the 19th century. The photovoltaic effect was first experimentally demonstrated by the French physicist A. E. Becquerel.

In 1839, at age 19, experimenting in his father's laboratory, he built the world's first photovoltaic cell, observing the action of light on a silver coated platinum electrode immersed in electrolyte that produced an electric current.

Forty years later the first solid state photovoltaic devices were constructed by workers investigating the recently discovered photoconductivity of selenium. In 1876, William Adams and Richard Day found that a photocurrent could be produced in a sample of selenium joined by two heated platinum contacts. The photovoltaic action of the selenium differed from its photoconductive action because a current was produced spontaneously by the action of light. No external power supply was needed. In this early photovoltaic device, a rectifying junction had been formed between the semiconductor and the metal contact.

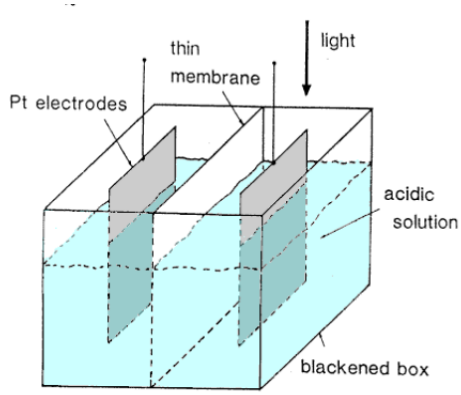

Figure A.1: Apparatus described by E.Becquerel in 1839.

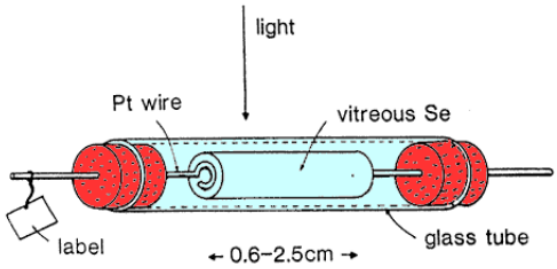

Figure A.2: Sample geometry used by Adams and Day for the investigation of the photoelectric effects in selenium.

In 1894, Charles Fritts prepared what was probably the first large area solar cell by pressing a layer of selenium between gold and other metals. Fritts was able to prepare thin Se films which adhered to one of the two plates, but not to the other. By pressing a gold leaf to the exposed selenium surface, he thereby prepared the first thin film photovoltaic devices.

In the following years photovoltaic effects were observed in copper-copper oxide thin film structures, in lead sulphide and thallium sulphide. These early

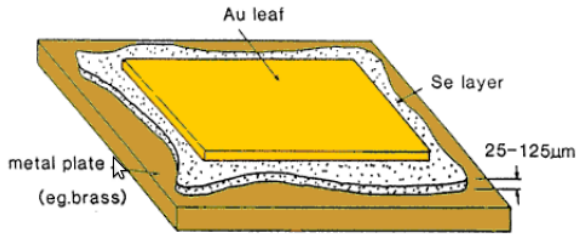

Figure A.3: Thin-film selenium device.

cells were thin film Schottky barrier devices, where a semitransparent layer of metal deposited on top of the semiconductor provided both the asymmetric electronic junction, which is necessary for photovoltaic action, and the access to the junction for the incident light.

The photovoltaic effect of these types of structures was related to the existence of a barrier to current flow at one of the semiconductor-metal interfaces (i.e., rectifying action) by Goldman and Brodsky in 1914.

During the 1930s, the theory of metal-semiconductor barrier layers was developed by Walter Schottky, Neville Mott and others. However, it was not the photovoltaic properties of materials like selenium which excited researchers, but the photoconductivity. The fact that the current produced was proportional to the intensity of the incident light, and related to the wavelength in a definite way meant that photoconductive materials were ideal for photographic light meters. The photovoltaic effect in barrier structures was an added benefit, meaning that the light meter could operate without a power supply.

It was not until the 1950s, with the development of good quality silicon wafers for applications in the new solid state electronics, that potentially useful quantities of power were produced by photovoltaic devices in crystalline silicon.

In the 1950s, the development of silicon electronics followed the discovery of a way to manufacture p-n junctions in silicon. Naturally n-type silicon wafers developed a p-type skin when exposed to the boron trichloride gas. Part of the skin could be etched away to give access to the n-type layer beneath. These p-n junction structures produced much better rectifying action than Schottky barriers, and better photovoltaic behavior.

The first silicon solar cell was reported by Chapin, Fuller and Pearson in 1954 and converted sunlight with an efficiency of 6%, six times higher than the best previous attempt but, at an estimated production cost of 200 $ per Watt, these cells were not seriously considered for power generation for several decades. Nevertheless, the early silicon solar cell did introduce the possibility of power generation in remote locations where fuel could not easily be delivered. The obvious application was to satellites where the requirement of reliability and low weight made the cost of the cells unimportant and during the 1950s and 60s, silicon solar cells were widely developed for applications in space.

In the 1970s the crisis in energy supply experienced by the oil-dependent western world led to a sudden growth of interest in alternative sources of energy, and funding for research and development in those areas. Photovoltaics was a subject of intense interest during this period, and a range of strategies for producing photovoltaic devices and materials more cheaply and for improving device efficiency were explored. Routes to lower cost included photoelectrochemical junctions, and alternative materials such as polycrystalline silicon, amorphous silicon, other *thin film* materials and organic conductors. Strategies for higher efficiency included tandem and other multiple band gap designs. Although none of these led to widespread commercial development, our understanding of the science of photovoltaics is mainly rooted in this period.

During the 1990s, interest in photovoltaics expanded, along with growing awareness of the need to secure sources of electricity alternative to fossil fuels. The trend coincides with the widespread deregulation of the electricity markets and growing recognition of the viability of decentralised power. During this period, the economics of photovoltaics improved primarily through economies of scale.

In the late 1990s the photovoltaic production expanded at a rate of 15-25% *per annum*, driving a reduction in cost. Photovoltaics first became competitive in contexts where conventional electricity supply is most expensive, for instance, for remote low power applications such as navigation, telecommunications, and rural electrification. As prices fall, new markets are opened up. An important example is building integrated photovoltaic applications, where the cost of the photovoltaic system is offset by the savings in building materials.

A.1 Photogeneration of charge carriers

The operation of a photovoltaic (PV) cell requires 3 basic steps:

1. The absorption of light, generating either electron-hole pairs or excitons
2. The separation of the various types of charge carriers
3. The separate extraction of those carriers to an external circuit

When a photon hits a piece of silicon, one of three things can happen:

- the photon can pass straight through the semiconductor (this generally happens for lower energy photons),
- the photon can reflect off the surface,
- the photon can be absorbed by the semiconductor, if the photon energy is higher than the band gap. This generates an electron-hole pair and sometimes heat, depending on the band structure.

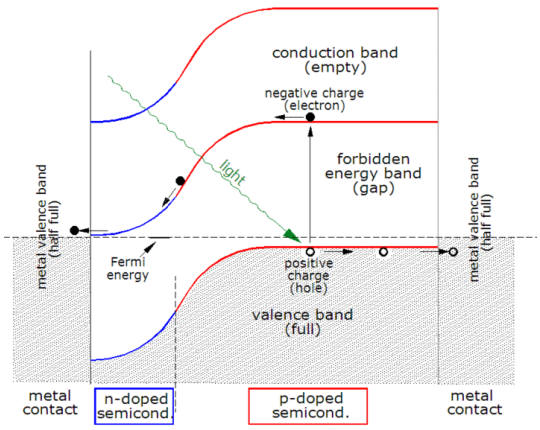

Figure A.4: Band diagram for a silicon solar cell.

When a photon is absorbed, its energy is given to an electron in the crystal lattice. Usually this electron is in the valence band, and is tightly bound in covalent bonds between neighboring atoms, and hence unable to move far.

Due to photon absorption, the electron in excited into the conduction band, where it is free to move around within the semiconductor. The covalent bond that the electron was previously a part of now has one fewer electron this is known as a hole.

The presence of a missing covalent bond allows the electrons of neighboring atoms to move into the hole, leaving another hole behind, and in this way a hole can move through the lattice. Thus, it can be said that photons absorbed in the semiconductor create mobile electron-hole pairs.

A photon needs to have greater energy than that of the band gap in order to excite an electron from the valence band into the conduction band. However, the solar frequency spectrum approximates a black body spectrum at about $5800K$, and as such, much of the solar radiation reaching the Earth is composed of photons with energies greater than the band gap of silicon. These higher energy photons will be absorbed by the solar cell, but the difference in energy between these photons and the silicon band gap is converted into heat (via lattice vibrations, the phonons) rather than into usable electrical energy. Charge carrier separation in a solar cell can occur in two different ways:

- drift of carriers, driven by an electric field established across the device
- diffusion of carriers due to their random thermal motion, until they are captured by the electrical fields existing at the edges of the active region.

In thick solar cells there isn't an electric field developing in the active region, so the dominant mode of charge carrier separation is diffusion. In these cells the diffusion length of minority carriers (the length that photogenerated carriers can travel before they recombine) must be large compared to the cell thickness.

In thin film cells (such as amorphous silicon), the diffusion length of minority carriers is usually very short due to the existence of defects, and the dominant charge separation is therefore drift, driven by the electrostatic field of the junction, which extends to the whole thickness of the cell. The most commonly known solar cell is configured as a large-area p-n junction made from silicon.

As a simplification, one can imagine bringing a layer of n-type silicon into direct contact with a layer of p-type silicon. In practice, p-n junctions of silicon

solar cells are not made in this way, but rather by diffusing an n-type dopant into one side of a p-type wafer (or *vice versa*). If a piece of p-type silicon is placed in intimate contact with a piece of n-type silicon, then a diffusion of electrons occurs from the region of high electron concentration (the n-type side of the junction) into the region of low electron concentration (p-type side of the junction). When the electrons diffuse across the p-n junction, they recombine with holes on the p-type side.

The diffusion of carriers does not continue indefinitely, however, because charges build up on either side of the junction and create an electric field. The electric field creates a diode that promotes charge flow, known as drift current, that opposes and eventually balances out the diffusion of electrons and holes. This region where electrons and holes have diffused across the junction is called the *depletion region*, because it no longer contains any mobile charge carriers, or the *space charge region*.

Ohmic metal-semiconductor contacts are made to both the n-type and p-type sides of the solar cell, and the electrodes connected to an external load. Electrons that are created on the n-type side, or have been collected by the junction and swept onto the n-type side, may travel through the wire, power the load, and continue through the wire until they reach the p-type semiconductor-metal contact. Here, they recombine with a hole that was either created as an electron-hole pair on the p-type side of the solar cell, or a hole that was swept across the junction from the n-type side after being created there.

The voltage measured is equal to the difference in the Fermi levels of the minority carriers, i.e. electrons in the p-type portion and holes in the n-type portion.

A.2 Equivalent circuit of a solar cell

To understand the electronic behavior of a solar cell, it is useful to create a model which is electrically equivalent, and is based on discrete electrical components whose behavior is well known. An ideal solar cell may be modelled by a current source in parallel with a diode; in practice no solar cell is ideal, so a shunt resistance and a series resistance component are added to the model. The resulting equivalent circuit of a solar cell is shown in Fig. *A*.5.

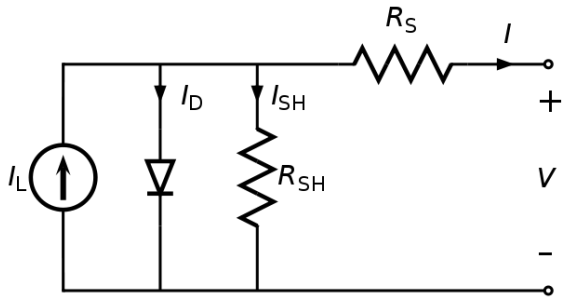

Figure A.5: The equivalent circuit of a solar cell.

A.2.1 Characteristic equation

From the equivalent circuit it is evident that the current produced by the solar cell is equal to that produced by the current source, minus the currents flowing through the diode, and through the shunt resistor:

$$I = I_L - I_D - I_{SH} \tag{A.1}$$

where:

I = output current
I_L = photogenerated current
I_D = diode current
I_{SH} = shunt current

The current through these elements is governed by the voltage drop across them:

$$V_j = V + IR_S \tag{A.2}$$

where:

V_j = voltage across both diode and resistor R_{SH}
V = voltage across the output terminals
R_S = series resistance.

By the Shockley diode equation, the current diverted through the diode is:

$$I_D = I_0 \left[\exp\left(\frac{qV_j}{nkT} \right) - 1 \right] \tag{A.3}$$

with:

I_0 = reverse saturation current
n = diode ideality factor (1 for an ideal diode)
q = elementary charge
k = Boltzmann's constant
T = absolute temperature

By Ohm's law, the current diverted through the shunt resistor is:

$$I_{SH} = \frac{V_j}{R_{SH}} \tag{A.4}$$

where R_{SH} is the shunt resistance. Substituting these into the first equation produces the characteristic equation of a solar cell, which relates solar cell parameters to the output current and voltage:

$$I = I_L - I_0 \left[\exp\left(\frac{q(V + IR_S)}{nkT} \right) - 1 \right] - \frac{V + IR_S}{R_{SH}}. \tag{A.5}$$

In principle, given a particular operating voltage V the equation may be solved to determine the operating current I at that voltage. However, because the equation involves I on both sides in a transcendental function the equation has no general analytical solution. However, even without a solution it is physically instructive. Furthermore, it is easily solved using numerical methods. Since the parameters I_0, n, R_S, and R_{SH} cannot be measured directly, the most common application of the characteristic equation is nonlinear regression to extract the values of these parameters on the basis of their combined effect on solar cell behavior.

A.2.2 Open-circuit voltage and short-circuit current

When the cell is operated at open circuit, $I = 0$ and the voltage across the output terminals is defined as the open-circuit voltage. Assuming the shunt

resistance is high enough to neglect the final term of the characteristic equation, the open-circuit voltage V_{OC} is:

$$V_{OC} \approx \frac{nkT}{q} \log\left(\frac{I_L}{I_0} + 1\right). \tag{A.6}$$

Similarly, when the cell is operated at short circuit, $V = 0$ and the current I through the terminals is defined as the short-circuit current. It can be shown that for a high-quality solar cell (low R_S and I_0, and high R_{SH}) the short-circuit current I_{SC} is:

$$I_{SC} \approx I_L. \tag{A.7}$$

It should be noted that it is not possible to extract any power from the device when operating at either open circuit or short circuit conditions.

A.2.3 Effect of physical size

The values of I_0, R_S, and R_{SH} are dependent upon the physical size of the solar cell. In comparing otherwise identical cells, a cell with twice the surface area of another will, in principle, has twice the I_0 because it has twice the junction area across which current can leak. It will also have half the R_S and R_{SH} because it has twice the cross-sectional area through which current can flow. For this reason, the characteristic equation is frequently written in terms of current density, or current produced per unit cell area:

$$J = J_L - J_0 \left[\exp\left(\frac{q(V + Jr_S)}{nkT}\right) - 1\right] - \frac{V + Jr_S}{r_{SH}} \tag{A.8}$$

where

J = current density
J_L = photogenerated current density
J_0 = reverse saturation current density
r_S = specific series resistance
r_{SH} = specific shunt resistance.

This formulation has several advantages. One is that, since cell characteristics are referenced to a common cross-sectional area, they may be compared between cells of different physical dimensions. While this is of limited benefit in a

manufacturing setting, where all cells tend to have the same size, it is useful in research and in comparing cells between manufacturers.

Another advantage is that the density equation naturally scales the parameter values to similar orders of magnitude, which can make numerical extraction of them simpler and more accurate even with *naive* solution methods.

There are practical limitations of this formulation. For instance, certain parasitic effects grow in importance as cell sizes shrink and can affect the extracted parameter values. Recombination and contamination of the junction tend to be greatest at the perimeter of the cell, so very small cells may exhibit higher values of J_0 or lower values of R_{SH} than larger cells that are otherwise identical. In such cases, comparisons between cells must be made cautiously.

This approach should only be used for comparing solar cells with comparable layout. For instance, a comparison between primarily quadratical solar cells, like the typical crystalline silicon ones, and narrow but long solar cells, like the typical thin film ones, can lead to wrong assumptions caused by the different kinds of current paths and therefore the influence of a distributed series resistance r_S.

A.2.4 Effect of temperature

Temperature affects the characteristic equation in two ways: directly, via T in the exponential term, and indirectly via its effect on I_0 (strictly speaking, temperature affects all of the terms, but these two far more significantly than the others). While increasing T reduces the magnitude of the exponent in the characteristic equation, the value of I_0 increases exponentially with T.

The net effect is to reduce V_{OC} (the open-circuit voltage) linearly with increasing temperature. The magnitude of this reduction is inversely proportional to V_{OC}; that is, cells with higher values of V_{OC} suffer smaller reductions in voltage with increasing temperature. For most crystalline silicon solar cells the change in V_{OC} with temperature is about $-0.50\%/^\circ$ C, though the rate for the highest-efficiency crystalline silicon cells is around $-0.35\%/^\circ$ C. By way of comparison, the rate for amorphous silicon solar cells is $-0.20\%/^\circ$C to $-0.30\%/^\circ$ C, depending on how the cell is made.

The amount of photogenerated current I_L increases slightly with increasing temperature because of an increase in the number of thermally generated carriers

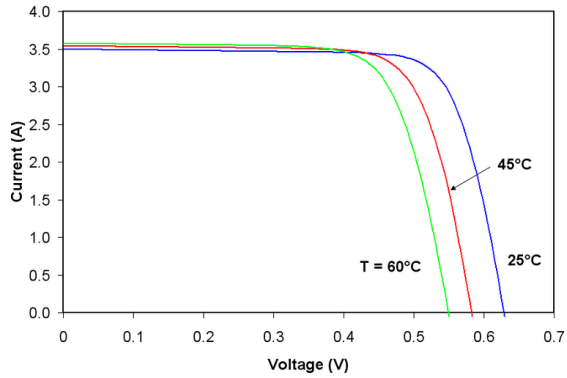

Figure A.6: Effect of temperature on the current-voltage characteristics of a solar cell.

in the cell. This effect is slight, however: about 0.065%/°C for crystalline silicon cells and 0.09 % for amorphous silicon cells.

The overall effect of temperature on cell efficiency can be computed using these factors in combination with the characteristic equation. However, since the change in voltage is much stronger than the change in current, the overall effect on efficiency tends to be similar to that on voltage. Most crystalline silicon solar cells decline in efficiency by 0.50%/° C and most amorphous cells decline by 0.15-0.25%/°C. The figure $A.6$ shows $I - V$ curves that might typically be seen for a crystalline silicon solar cell at various temperatures.

A.2.5 Series resistance

As series resistance increases, the voltage drop between the junction voltage and the terminal voltage becomes greater for the same current. The result is that the current-controlled portion of the $I - V$ curve begins to sag toward the origin, producing a significant decrease in the terminal voltage V and a slight reduction in I_{SC}, the short-circuit current.

Very high values of R_S will also produce a significant reduction in I_{SC}; in these regimes, series resistance dominates and the behavior of the solar cell

resembles that of a resistor. These effects are shown for crystalline silicon solar cells in the $I-V$ curves displayed in figure $A.7$.

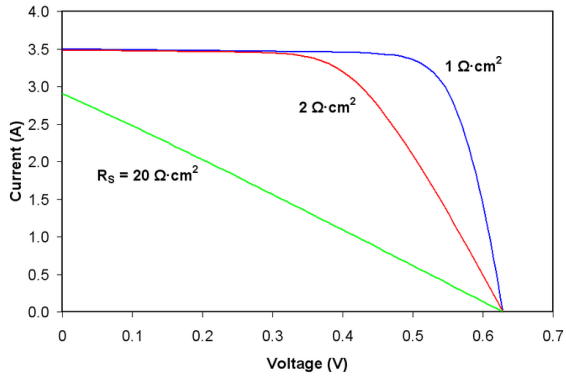

Figure A.7: Effect of series resistance on the current-voltage characteristics of a solar cell.

Losses caused by series resistance are in a first approximation given by $P_{loss} = V_{Rs}I = I^2R_S$ and increase quadratically with photocurrent. Series resistance losses are therefore most important at high illumination intensities.

A.2.6 Shunt resistance

As shunt resistance decreases, the current diverted through the shunt resistor increases for a given level of junction voltage. The result is that the voltage-controlled portion of the $I-V$ curve begins to sag toward the origin, producing a significant decrease in the terminal current I and a slight reduction in V_{OC}. Very low values of R_{SH} produce a significant reduction in V_{OC}.

Much as in the case of a high series resistance, a badly shunted solar cell will take on operating characteristics similar to those of a resistor. These effects are shown for crystalline silicon solar cells in the $I-V$ curves displayed in the figure $A.8$

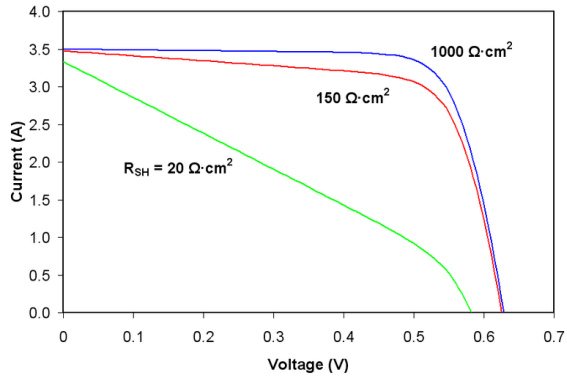

Figure A.8: Effect of shunt resistance on the currentvoltage characteristics of a solar cell.

A.2.7 Reverse saturation current

If one assumes infinite shunt resistance, the characteristic equation can be solved for V_{OC}:

$$V_{OC} = \frac{kT}{q} \log\left(\frac{I_{SC}}{I_0} + 1\right). \tag{A.9}$$

Thus, an increase in I_0 produces a reduction in V_{OC} proportional to the inverse of the logarithm of the increase. This explains mathematically the reason for the reduction in V_{OC} that accompanies increases in temperature described above. The effect of reverse saturation current on the $I-V$ curve of a crystalline silicon solar cell are shown in figure $A.9$.

Physically, reverse saturation current is a measure of the *leakage* of carriers across the p-n junction in reverse bias. This leakage is a result of carrier recombination in the neutral regions on either side of the junction.

A.2.8 Ideality factor

The ideality factor (also called emissivity factor) is a fitting parameter that describes how closely the diode's behavior matches that predicted by theory,

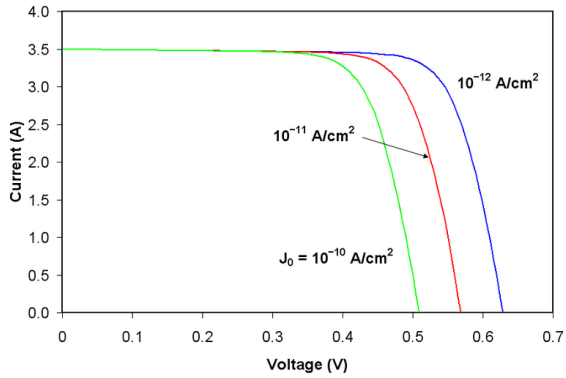

Figure A.9: Effect of reverse saturation current on the current-voltage characteristics of a solar cell.

which assumes the p-n junction of the diode is an infinite plane and no recombination occurs within the space-charge region.

A perfect match to theory is indicated when $n = 1$. When recombinations in the space-charge region dominate other recombinations, one has $n = 2$. The effect of changing ideality factor independently of all other parameters is shown for a crystalline silicon solar cell in the I-V curves displayed in figure $A.10$.

Most solar cells, which are quite large compared to conventional diodes, well approximate an infinite plane and will usually exhibit near-ideal behavior under Standard Test Condition (STC) ($n \sim 1$). Under certain operating conditions, however, device behavior may be dominated by recombination in the space-charge region. This is characterized by a significant increase in I_0 as well as an increase in ideality factor to $n \sim 2$. The latter tends to increase solar cell output voltage while the former acts to erode it.

The net effect, therefore, is a combination of the increase in voltage shown for increasing n in figure $A.10$ and the decrease in voltage shown for increasing I_0. Typically, I_0 is the more significant factor and the result is a reduction in voltage.

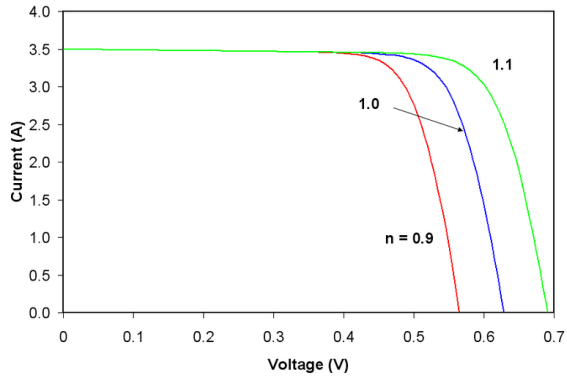

Figure A.10: Effect of ideality factor on the current-voltage characteristics of a solar cell.

A.3 Solar cell efficiency

Solar cell efficiency is the ratio of the electrical output of a solar cell, to the incident energy, in the form of sunlight. The average energy of sunlight on a sunny day is about 1 kW/m^2. A 1 $\times$ 1.5 m^2 solar panel made of 20% efficient solar cells would receive 1.5 kW of energy from the sun, providing an output of 300 watts.

The energy conversion efficiency (η) of a solar cell is the percentage of the solar energy to which the cell is exposed that is converted into electrical energy. The efficiency of the solar cells used in a photovoltaic system forms the starting point for the overall annual output of the system.

Several factors affect a cell conversion efficiency value, including its reflectance efficiency, thermodynamic efficiency, charge carrier separation efficiency, and conduction efficiency values. Because these parameters can be difficult to measure directly, other parameters are measured instead, including *quantum efficiency*, V_{OC} *ratio*, and *fill factor*.

Reflectance losses are accounted for by the quantum efficiency value, as they affect *external quantum efficiency*. Recombination losses affect the quantum efficiency, V_{OC} ratio, and fill factor values. Resistive losses are predominantly

accounted for by the fill factor value, but also contribute to the quantum efficiency and V_{OC} ratio values.

Energy conversion efficiency is defined by dividing a cell power output (in watts) at its maximum power point (P_m) by the input light (E, in W/m^2) and the surface area of the solar cell (A_c in m^2) under standard test conditions.

$$\eta = \frac{P_m}{E \cdot A_c} \tag{A.10}$$

STC specifies a temperature of 25°C and an irradiance of 1000 W/m^2 with an air mass 1.5 (AM 1.5) spectrum. These correspond to the irradiance and spectrum of sunlight incident on a clear day upon a sun-facing 37° tilted surface with the sun at an angle of 41.81° above the horizon. This condition approximately represents solar noon near the spring and autumn equinoxes in the continental United States with surface of the cell aimed directly at the sun.

For example, under these test conditions a solar cell of 12% efficiency with a 0.01 m^2 surface area would produce 1.2 watts of power. In 2012, the highest efficiencies have been achieved by using multiple junction cells at high solar concentrations (43.5% using 418x concentration).

A.3.1 Thermodynamic efficiency limit

The maximum theoretically possible conversion efficiency for sunlight is 93% due to the Carnot limit, given the temperature of the photons emitted by the sun's surface. However, solar cells operate as quantum energy conversion devices, and are therefore subject to the *thermodynamic efficiency limit*.

Photons with an energy below the band gap of the absorber material cannot generate a hole-electron pair, and so their energy is not converted to useful output and only generates heat if absorbed. For photons with an energy above the band gap, only a fraction of the energy above the band gap can be converted to useful output.

When a photon of greater energy is absorbed, the excess energy above the band gap is converted to carrier kinetic energy. The excess kinetic energy is converted to heat through phonon interactions as the kinetic energy of the carriers slows to equilibrium velocity. Solar cells with multiple band gap absorber materials improve efficiency by dividing the solar spectrum into smaller bins where the thermodynamic efficiency limit is higher for each bin.

A.3.2 Quantum efficiency

As described above, when a photon is absorbed by a solar cell it can produce an electron-hole pair. One of the carriers may reach the p-n junction and contribute to the current produced by the solar cell; such a carrier is said to be collected or, the carrier can recombine with no net contribution to cell current.

Quantum Efficiency refers to the percentage of photons that are converted to electric current (i.e., collected carriers) when the cell is operated under short circuit conditions. Some of the light striking the cell is reflected, or passes

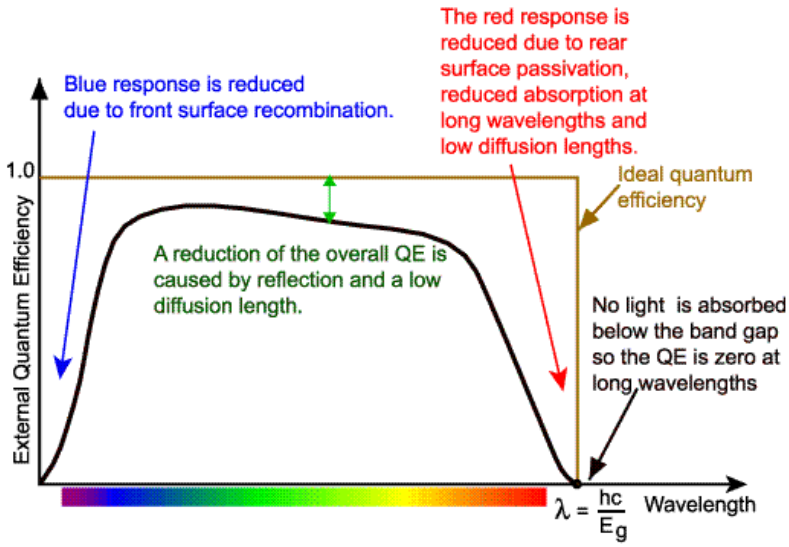

Figure A.11: The quantum efficiency of a silicon solar cell. Quantum efficiency is usually not measured much below 350 nm as the power contained in such low wavelengths is low.

through the cell; **External Quantum Efficiency** (EQE) is the fraction of incident photons that are converted to electric current.

Not all the photons captured by the cell contribute to electric current; **Internal Quantum Efficiency** (IQE) is the fraction of absorbed photons that are converted to electric current.

Quantum efficiency is most usefully expressed as a spectral measurement (that is, as a function of photon wavelength or energy). Since some wavelengths are absorbed more effectively than others, spectral measurements of quantum efficiency can yield valuable information about the quality of the semiconductor bulk and surfaces. Quantum efficiency alone is not the same as overall energy conversion efficiency, as it does not convey information about the fraction of power that is converted by the solar cell.

A.3.3 Maximum power point

A solar cell may operate over a wide range of voltages (V) and currents (I). By increasing the resistive load on an irradiated cell continuously from zero (a short circuit) to a very high value (an open circuit) one can determine the maximum power point, the point that maximizes $V \cdot I$; that is, the load for which the cell can deliver maximum electrical power at that level of irradiation (the output power is zero in both the short circuit and open circuit extremes).

A high quality, monocrystalline silicon solar cell, at 25°C cell temperature, may produce 0.60 volts open-circuit (V_{OC}). The cell temperature in full sunlight, even with 25° C air temperature, will probably be close to 45°C, reducing the open-circuit voltage to 0.55 volts per cell. The voltage drops modestly, with this type of cell, until the short-circuit current is approached (I_{SC}). Maximum power (with 45°C cell temperature) is typically produced with 75% to 80% of the open-circuit voltage (0.43 volts in this case) and 90% of the short-circuit current.

This output can be up to 70% of the $V_{OC} \cdot I_{SC}$ product. The short-circuit current from a cell is nearly proportional to the illumination, while the open-circuit voltage may drop only 10% with a 80% drop in illumination. Lower-quality cells have a more rapid drop in voltage with increasing current and could produce only 1/2 V_{OC} at 1/2 I_{SC}. The usable power output could thus drop from 70% of the $V_{OC} \cdot I_{SC}$ product to 50% or even as little as 25%.

The maximum power point of a photovoltaic varies with incident illumination. For example, accumulation of dust on photovoltaic panels reduces the maximum power point. For systems large enough to justify the extra expense, a maximum power point tracker tracks the instantaneous power by continually measuring the voltage and current (and hence, power transfer), and uses this

information to dynamically adjust the load so the maximum power is always transferred, regardless of the variation in lighting.

A.3.4 Fill factor

Another defining term in the overall behavior of a solar cell is the fill factor (FF). This is the available power at the maximum power point (P_m) divided by the open circuit voltage V_{OC} and the short circuit current I_{SC}:

$$FF = \frac{P_m}{V_{OC} \cdot I_{SC}} = \frac{\eta \cdot A_c \cdot E}{V_{OC} \cdot I_{SC}}. \tag{A.11}$$

The fill factor is directly affected by the values of the cell's series and shunt resistances. Increasing the shunt resistance (R_{sh}) and decreasing the series resistance (R_s) lead to a higher fill factor, thus resulting in greater efficiency, and bringing the cel output power closer to its theoretical maximum.

List of Publications and Presentations

Publications related to this thesis

C. Pintossi, G. Salvinelli, G. Drera, S. Pagliara, L. Sangaletti, S. Del Gobbo, M. Morbidoni, M. Scarselli, M. De Crescenzi,"Direct Evidence of Chemically Inhomogeneous, Nanostructured, Si-O Buried Interfaces and Their Effect on the Efficiency of Carbon Nanotube/Si Photovoltaic Heterojunctions", *J. Phys. Chem. C*, **117**, 18688-18696 (2013).

C. Pintossi, S. Pagliara, G. Drera, F. De Nicola, P. Castrucci, M. De Crescenzi, M. Crivellari, M. Boscardin and L. Sangaletti, "Steering the Efficiency of Carbon NanotubeSilicon Photovoltaic Cells by Acid Vapor Exposure: A Real-Time Spectroscopic Tracking", *ACS Appl. Mater. Interfaces*, **7** (18), 9436-9444 (2015).

F. De Nicola, C. Pintossi, F. Nanni, I. Cacciotti, M. Scarselli, G. Drera, S. Pagliara, L. Sangaletti, M. De Crescenzi, and P. Castrucci, "Controlling the thickness of carbon nanotube random network films by the estimation of the absorption coefficient", *Carbon*, **95**, 28-33 (2015).

C. Pintossi and L. Sangaletti, "Semiconducting Carbon Nanotubes: Properties, Characterization and Selected Applications", pp 239-259, Chapter 10 of the Book: *Low-Dimensional and Nanostructured Materials and Devices*, Springer

(2016).

Publications in preparation

C. Pintossi, S. Ponzoni, S. Pagliara, G. Drera, F. De Nicola, P. Castrucci, M. De Crescenzi, and L. Sangaletti, "Oxide Dependence of Interface Charge Carrier Dynamics in Carbon Nanotube-Silicon Solar Cells", *in preparation.*

C. Pintossi, F. Rigoni, S.Pagliara, G. Drera, F. De Nicola, P. Castrucci, M. De Crescenzi and L. Sangaletti, "A cross-functional nanostructured platform based on CNT-Si hybrid junctions: where photon harvesting meets gas sensing", *in preparation.*

Oral and poster presentations at international conferences

C. Pintossi *et al.*, oral presentation: *Development, characterization and regeneration of photovoltaic hybrid devices based on heterojunctions between ultrathin layers of carbon nanotubes and silicon*, International Conference of Diamond and Related Materials, Riva del Garda (Italy), 2013.

C. Pintossi *et al.*, flash oral and poster presentations: *Regeneration of photovoltaic hybrid devices based on heterojunctions between carbon nanotube and silicon*, SILS summer school, Grado (Italy), 2013.

C. Pintossi *et al.*, oral and poster presentations: *Nanosized buried interfaces in CNT/Si solar cells: regeneration and efficiency optimization through AR-XPS analysis*, Workshop: From carbon nanotubes to graphene: the key materials of the future?, Brescia (Italy), 2013.

C. Pintossi *et al.*, oral and flash presentations: *Effects of the nanostructured SiO_x buried interface tuning on the efficiency of CNT/Si photovoltaic devices*,

ECOSS30 (European Conference of Surface Science), Antalya (Turkey), 2014.

C. Pintossi *et al.*, poster presentation: *Acid-induced surface and interface modifications and their effect on CNT/Si solar cells efficiency*, ECOSS30 (European Conference of Surface Science), Antalya (Turkey), 2014.

C. Pintossi *et al.*, oral presentation: *Investigating the buried interface in carbon nanotube/silicon solar cells: understanding its properties to improve performances*, SIF (Societá Italiana Fisica), Pisa (Italy), 2014.

C. Pintossi *et al.*, oral presentation: *Investigating the buried interface in carbon nanotube/silicon solar cells: understanding its properties to improve performances*, EMRS (European Materials Research Society) Fall Meeting, Warsaw (Poland), 2015.

C. Pintossi *et al.*, oral presentation: *How far can an oxide interface layer affect efficiency in CNT/Si solar cells?*, EMRS (European Materials Research Society) Fall Meeting, Warsaw (Poland), 2015.

C. Pintossi *et al.* flash and poster presentation: *Acid-induced surface and interface modifications and their effect on CNT/Si solar cells efficiency*, TrendOxides, Brescia (Italy), 2015.

Bibliography

[1] M. Endo, *Mecanisme de croissance en phase vapeur de bres de carbone (The growth mechanism of vapor-grown carbon fibers)*. PhD thesis, University of Orleans, Orleans, France (1975), in French.

[2] M. Endo, *PhD thesis*, Nagoya University, Japan (1978), in Japanese.

[3] S. Iijima, *J. Cryst. Growth*, **55** 675-683 (1980).

[4] A. Oberlin, M. Endo, and T. Koyama, *Carbon* **14**, 133 (1976).

[5] A. Oberlin, M. Endo, and T. Koyama, *J. Cryst. Growth* **32**, 335-349 (1976).

[6] S. Iijima, *Nature* **354**, 56 - 58 (1991).

[7] M.S. Dresselhaus, G. Dresselhaus, Ph. Avouris, *Carbon Nanotubes. Synthesis, Structure, Properties, and Applications*. Springer (2001).

[8] P. Castrucci, C. Scilletta, S. Del Gobbo, M. Scarselli, L. Camilli, M. Simeoni, B. Delley, A. Continenza and M. De Crescenzi *Nanotechnology* **22** 115701 (2011).

[9] I. Stemmler and C. Backes *Absorption Spectroscopy as a Powerful Technique for the Characterization of Single-Walled Carbon Nanotubes* White paper, *PerkinElmer* (2013).

[10] M.S. Dresselhaus, G. Dresselhaus, R. Saito and A. Jorio *Physics Reports* **409** 4799 (2005).

[11] P. Melinon , B. Masenelli , F. Tournus , A. Perez , *Nat. Mater.*, **6**, 479.

[12] Y. L. Wang , R. A. Poirier , *Can.J.Chem.*, **76** , 477 (1998).

[13] G. K. Bhagavat , K. D. Nayak, *Thin Solid Films*,**64**, 57 (1979) .

[14] P. H. Fang , T. Takeuchi , E. Y. Chen , *Sol. Cells*, **28** , 315 (1990).

[15] G. Amaratunga , W. Milne , A. Putnis , *IEEE Electron Device Lett.*, **11**, 33 (1990).

[16] H. A. Yu , Y. Kaneko , S. Yoshimura , S. Otani , *Appl. Phys. Lett.* , **68** , 547 (1996).

[17] K. M. Krishna , T. Soga , T. Jimbo , M. Umeno , *Carbon*, **37**, 531 (1999).

[18] N. Konofaos , E. Evangelou , C. B. Thomas , *J. Appl. Phys.*, **84** , 4634 (1998).

[19] M. Allonalaluf , J. Appelbaum , M. Maharizi , A. Seidman , N. Croitoru , *Thin Solid Films*, **303** , 273 (1997).

[20] S. Saito , A. Oshiyama , *Phys. Rev. Lett.*, **66** , 2637 (1991).

[21] S. L. Ren , Y. Wang , A. M. Rao , E. Mcrae , J. M. Holden , T. Hager , K. A. Wang , W. T. Lee , H. F. Ni , J. Selegue , P. C. Eklund , *Appl. Phys. Lett.*, **59** , 2678 .(1991)

[22] J. Mort , M. Machonkin , R. Ziolo , D. R. Huffman , M. I. Ferguson , *Appl. Phys. Lett.*, **60** , 1735 (1992).

[23] K. M. Chen , Y. Q. Jia , S. X. Jin , K. Wu , X. D. Zhang , W. B. Zhao , C. Y. Li , Z. N. Gu , *J. Phys. Condens. Matter*, **6** , L367 (1994).

[24] C. J. Wen , T. Aida , I. Honma , H. Komiyama , K. Yamada , *Denki Kagaku*, **62** , 264 (1994).

[25] D. J. Fu , Y. Y. Lei , J. C. Li , M. S. Ye , H. X. Guo , Y. G. Peng , X. J. Fan , *Appl. Phys. A : Mater.*, **67** , 441 (1998).

[26] T. Kim, H. Kim, J. Park, H. Kim, Y. Yoon, S. Kim, C. Shin, H. Jung, I. Kim, D. S. Jeong , H. Kim, J. Y. Kim, B. Kim, M. J. Ko, H. J. Son, C. Kim, J. Yi, S. Han, D. Lee, *Sci. Rep.*, *4* , 7154 (2014).

[27] M. H. Yun , J. H. Jang , K. M. Kim , H. Song , J. C. Lee , J. Y. Kim , *Phys. Chem. Chem. Phys.*, **15** , 19913 (2013).

[28] X. Li, Z. Lv, and H. Zhu, *Adv. Mater.* **27**, 65496574 (2015).

[29] A. S. Mayorov , R. V. Gorbachev , S. V. Morozov , L. Britnell , R. Jalil , L. A. Ponomarenko , P. Blake , K. S. Novoselov , K. Watanabe, T. Taniguchi , A. K. Geim , *Nano Lett.*, **11** , 2396 (2011).

[30] X. M. Li , H. W. Zhu , K. L. Wang , A. Y. Cao , J. Q. Wei , C. Y. Li , Y. Jia , Z. Li , X. Li , D. H. Wu , *Adv. Mater.*, **22** , 2743 (2010).

[31] Y. Song , X. M. Li , C. Mackin , X. Zhang , W. J. Fang , T. Palacios , H. W. Zhu , J. Kong , *Nano Lett.* , **15** , 2104 (2015).

[32] X. M. Li, D. Xie, H. Park, M. Zhu, T. H. Zeng, K. L. Wang, J. Q. Wei, D. H. Wu, J. Kong, H. W. Zhu, *Nanoscale*, **5** , 1945 (2013).

[33] X. C. Miao, S. Tongay, M. K. Petterson, K. Berke, A. G. Rinzler, B. R. Appleton, A. F. Hebard, *Nano Lett.*, **12** , 2745 (2012).

[34] Y. Shi , K. K. Kim , A. Reina , M. Hofmann , L. Li , J. Kong , *ACS Nano.*, **4** , 2689 (2010).

[35] E. Kymakisa and G.A.J.Amaratunga, *Appl. Phys. Lett.* **80** (1) 112-114 (2010).

[36] B. Pradhan, S. K. Batabyal, A. J. Pal *Applied Physics Letters* **88** (9): 093106.

[37] D. Chirvase, J. Parisi, J. C. Hummelen, V. Dyakonov, *Nanotechnology* **15** (9): 1317-1323.

[38] I. Robel, B. A. Bunker, P. V, Kamat, *Adv. Mater.* **17** (20): 24582463

[39] Y. K. Jin, K. Lee, N. E. Coates, D. Moses, T. Q. Nguyen, M. Dante, A. J. Heeger, *Science* **317** (5835): 222225.

[40] J. Van de Lagemaat. T.M. Barnes, G. Rumbles, S. E. Shaheen, T. J. Coutts, C. Weeks, I. Levitsky, J. Peltola and P. Glatkowski *Appl. Phys. Lett.* **88** 23: 23350313.

[41] P. Brown, K. Takechi, P. V. Kamat *J. Phys. Chem. C*, **112**, 4776-4782 (2008).

[42] A. K. K. Kyaw, H. Tantang, T. Wu, L. Ke, C. Peh, Z. H. Huang, X. T. Zeng, H. V. Demir, Q. Zhang, and X. W. Sun *Appl. Phys. Lett.* **99**, 021107 (2011).

[43] A. Fujiwara, Y. Matsuoka, H. Suematsu, N. Ogawa, K. Miyano, H. Kataura, Y. Maniwa, S. Suzuki, and Y. Achiba, *Jpn. J. Appl. Phys.*, **40**, L1229-L1231 (2001).

[44] A. Mohite, S. Chakraborty, P. Gopinath, G. U. Sumanasekera and B. W. Alphenaar, *Appl. Phys. Lett.*, **86**, 061114 (2005).

[45] W. Shockley and H. J. Queisser, *J. Appl. Phys.*, **32**, 510 (1961).

[46] S. Wang, M. Khafizov, X. Tu, M. Zheng and T. D. Krauss, *Nano Lett.*, **10**, 2381-2386 (2010).

[47] P. L. McEuen and J. Y. Park, J.Y., *MRS Bull.*, **29**, 272-275 (2004).

[48] P. Castrucci, M. Scarselli, M. De Crescenzi, M. A. El Khakani, F. Rosei, N. Braidy, N. and J. H. Yi, *Appl. Phys. Lett.*, **85**, 3857(2004).

[49] Sun,J.L.; ,J.Q.; Zhu,J.L.; Xu,D. *Appl. Phys. Lett.*, **88**, 131107-131109 (2006).

[50] Jinquan Wei, Yi Jia, Qinke Shu et al. *Nanoletters* **7** (8), 2317-2321 (2007).

[51] P. Castrucci, C. Scilletta, S. Del Gobbo,M. Scarselli, L. Camilli, M. Simeoni,B. Delley , A. Continenza,M. De Crescenzi *Nanotechnology* **22**, 115701 (2011).

[52] E. Shi, L. Zhang, Z. Li, P. Li, Y. Shang, Y. Jia, J. Wei, K. Wang, H. Zhu, D. Wu, S. Zhang and A. Cao, *Scientific Report*, **2**, 884 (2012).

[53] Z. Li, V. P. Kunets, V. Saini, Y. Xu, E. Dervishi, G. J. Salamo, A. R. Biris and A. S. Biris, *ACS Nano*, **3**, 1407-1414 (2009).

[54] Y. Jia, P. Li, J. Wei, A. Cao, K. Wang, C. Li, D. Zhuang, H. Zhu and D. Wu, *Mater. Research Bull.*, **45**, 1401-1405 (2010).

[55] S. Del Gobbo, P. Castrucci, M. Scarselli, L. Camilli, M. De Crescenzi, L. Mariucci, A. Valletta, A. Minotti, and G. Fortunato, *Appl. Phys. Lett.*, **98**, 183113 (2011).

[56] S. Del Gobbo, P. Castrucci, S. Fedele, L. Riele, A. Convertino, M. Morbidoni, F. De Nicola, M. Scarselli, L. Camilli and M. De Crescenzi, *J. Mater. Chem. C*, **1**, 6752-6758 (2013).

[57] A. Einstein, *Annalen der Physik*, **322**, 6, 132148, (1905).

[58] C. S. Fadley. *Basic Concepts of X-ray Photoelectron Spectroscopy, Electron Spectroscopy, Theory, Thechniques and Applications.*, Pergamon Press, (1978).

[59] D. Briggs and M. Seah. *Practical Surface Analysis, Auger and X-ray Photoelectron Spectroscopy.* Wiley (1996).

[60] M. A. H. Wolfgang Schattke. *Solid-State Photoemission and related Methods, theory and experiment.* Wiley (2003).

[61] J. M. Hollas. *Modern Spectroscopy.* Wiley (2004).

[62] C. S. Fadley. *Angle-resolved X-Ray Photoelectron Spectroscopy, in Progr.Surf. Science.* Pergamon Press, (1984).

[63] S. Tanuma, C.J. Powell and D.R. Penn, *Surf. Interf. Anal.*, **35**, 268-275 (2003).

[64] Alberto Herrera-Gomez *Self consistent ARXPS analysis for multilayer conformal films with abrupt interfaces* Internal report (2008).

[65] F. Wooten, OPTICAL PROPERTIES OF SOLIDS, *Academic Press* (1972).

[66] V. Lucarini, K. Peiponen, J. J. Saarinen and E. M. Vartiainen, Kramers Kronig Relations in Optical Materials Research, *Springer* (2005).

[67] A. Jorio, G. Dresselhaus and M. S. Dresselhaus, Carbon Nanotubes: Advanced Topics in the Synthesis, Structure, Properties and Applications, *Springer-Verlag*, (2008).

[68] Y. Z. Ma, L. Valkunas, S. L. Dexheimer and G. R. Fleming", *Mol. Phys.*, **104**, 1179-1189 (2006).

[69] M. J. O Connell, S. M. Bachilo, C. B. Huffman, V. C. Moore, M. S. Strano, E. H. Haroz, K. L. Rialon, P. J. Boul, W. H. Noon, C. Kittrell, J. P. Ma, R. H. Hauge, R. B. Weisman and R. E. Smalley, *Science*, **297**, 593-596 (2002).

[70] Y.Z. Ma, C. D. Spataru, L. Valkunas, S. G. Louie and G. R. Fleming", *Phys. Rev. B*, **74**, 085402 (2006).

[71] C. Manzoni, A. Gambetta, E. Menna, M. Meneghetti, G. Lanzani and G. Cerullo, *Phys. Rev. Lett*, **94**, 20, 207401-4 (2005).

[72] F.Wang, G. Dukovic, E. Knoesel, L. E. Brus and T. F. Heinz, *Phys. Rev. B*, **70**, 241403 (2004).

[73] Y. Z. Ma, J. Stenger, J. Zimmermann, S. M. Bachilo, R. E. Smalley, R. B. Weisman *et al., J. Chem. Phys.*, **120**, 7, 3368-73 (2004).

[74] L. Luer, S. Hoseinkhani, D. Polli, J. Crochet, T. Hertel and G. Lanzani, *Nat. Phys.*, **5**, 54-58 (2008).

[75] T. Hertel and G. Moos, *Phys. Rev. Lett.*, **84**, 5002-5005 (2000).

[76] S.I. Anisimov, B.L. Kapeliovich and T.L. Perelman, *Zh. Eksp. Teor. Fiz.*, **66**, 776 (1974).

[77] G. Moos, R. Fasel and T. Hertel, *J. Nanosci. Nanotech.*, **3**, 145-149 (2002).

[78] P. B. Allen, *Phys. Rev. Lett.*, **59**, 1460-1463 (1987).

[79] S. Frank, P. Poncharal, Z. L.Wang and W. A. de Heer, *Science*, **280**, 1744-1746 (1998).

[80] F. De Nicola, C. Pintossi, F. Nanni, I. Cacciotti, M. Scarselli, G. Drera, S. Pagliara, L. Sangaletti, M. De Crescenzi, and P. Castrucci, *Carbon*, **95**, 28-33 (2015).

[81] F. De Nicola, P. Castrucci, M. Scarselli, F. Nanni, I. Cacciotti, and M. De Crescenzi. *SCIENTIFIC REPORTS*, **5** : 8583 (2015).

[82] V. Le Borgne, L. A. Gautier, P. Castrucci, S. Del Gobbo, M. De Crescenzi, M. A. El Khakani, *Nanotechnology*, **23**, 215206215216 (2012).

[83] Y. Jia, J. Wei, K. Wang, A. Cao, A.; Q. Shu, X. Gui, Y. Zhu, D. Zhuang, G. Zhang, B. Ma, *Adv. Mater.*, **20**, 45944598 (2008).

[84] Y. Jia, A. Cao, F. Kang, P. Li, X. Gui, L. Zhang, E. Shi, J. Wei, K. Wang, H. Zhu, *Phys. Chem. Chem. Phys.*, **14**, 83918396 (2012).

[85] C. Pintossi, G. Salvinelli, G. Drera, S. Pagliara, L. Sangaletti, S. Del Gobbo, M. Morbidoni, M. Scarselli, M. De Crescenzi, *J. Phys. Chem. C*, **117**, 18688-18696 (2013). and Paola Castrucci

[86] M. P. Seah, I. Gilmore, G. Beamson, *Surf. Interface Anal.*, **26**, 642649 (1998).

[87] G. Waligorski and W. E. Cooke, *Meas. Sci. Technol.*, **12**, 299-305 (2001).

[88] (20) W. A. M. Aarnik, A. Weishaupt and A. van Silfout, *Appl. Surf. Sci.*, **45**, 37-48 (1990).

[89] J. J. Yeh, I. Lindau, I. *Atomic Data Nuclear Data Tables*, **32**, 1-155 (1985).

[90] W. S. M. Werner, *Surf. Int. Anal.* **31**, 141-176 (2001).

[91] I. Tilinin, A. Jablonski, J. Zemek, S. J. Hucek, *J. Electron Spectrosc. Relat. Phenom.* , **97**, 127140 (1997).

[92] A. Jablonski, *Phys. Rev. B*, 58, 16470-16480 (1998).

[93] S. Doniach, M. Sunjic, *J. Phys. C: Solid State Phys.*, **3**, 285-291 (1970).

[94] S. Hufner, *Photoelectron Spectroscopy: Principles and Applications*; Springer: Berlin (1995).

[95] F. Sette, G. Wertheim, Y. Ma, G. Meigs, S. Modesti, C. Chen, Phys. Rev. B 1990, 41, 9766-9770.

[96] K. A. Wepasnick, B. A. Smith, J. L. Bitter, D. H. Fairbrother, *Anal. Bioanal. Chem.*, **396**, 1003-1014 (2010).

[97] T. Aoyama, T. Sugii, T. Ito, *Appl. Surf. Sci.*, **41**, 584-586 (1989).

[98] A. Galuska, J. Uht, N. Marquez, *J. Vac. Sci. Technol. A*, 6, 110-122 (1988).

[99] T. Maruyama, H. Bang, N. Fujita, Y. Kawamura, S. Naritsuka, M. Kusunoki, *Diamond Relat. Mater.*, **16**, 1078-1081 (2007).

[100] Y. Liu, Z. Zhang, M. C. Wells, T. P. Beebe, *Langmuir*, **21**, 8883-8891 (2005).

[101] H. Wei, S. N. Kim, S. Kim, B. D. Huey, F. Papadimitrakopoulos, H. L. Marcu, *Mater. Sci. Eng. C*, **28**, 1366-1371 (2008).

[102] V. Le Borgne, P. Castrucci, S. Del Gobbo, M. Scarselli, M. De Crescenzi, M. Mohamedi, M. A. El Khakani, *Appl. Phys. Lett.*, **97**, 193105-193107 (2010).

[103] Y. Jia, P. Li, X. Gui, J. Wei, K. Wang, H. Zhu, D. Wu, L. Zhang, A. Cao, Y. Xu, *Appl. Phys. Lett.*, **98**, 133115-133118 (2011).

[104] P. Castrucci, *Adv. Nano Res.*, **2**, 23-56 (2014).

[105] D. D. Tune, A. J. Blanch, R. Krupke, B. S. Flavel, J. G. Shapter, *Phys. Status Solidi A*, **211**, 1479-1487 (2014).

[106] Y. Jung, X. Li, N. K. Rajan, A. D. Taylor, M. A. Reed, *Nano Lett.*, **13**, 96-99 (2013).

[107] P. Wadhwa, B. Liu, M. A. McCarthy, Z. Wu, A. G. Rinzler, *Nano Lett.*, **10**, 5001-5005 (2010).

[108] H. C. Card, *Solid-State Electron.*, **20**, 971-976 (1977).

[109] X. Li, J. S. Huang, S. Nejati, L. McMillon, S. Huang, C. O. Osuji, N. Hazari, A. D. Taylor, *Nano Lett.*, **14**, 6179-6184 (2014).

[110] T. Lin, V. Bajpai, T. Ji, L. Dai, *Aust. J. Chem. Phys.*, **56**, 635-651 (2003).

[111] Y. Jia, A. Cao, X. Bai, Z. Li, L. Zhang, N. Guo, J. Wei, K. Wang, H. Zhu, D. Wu, P. M. Ajayan, *Nano Lett.*, **11**, 1901-1905 (2011).

[112] F. Wang, D. Kozawa, Y. Miyauchi, K. Hiraoka, S. Mouri, K. Matsuda, *Appl. Phys. Express*, **6** (102301), 1-4 (2013).

[113] K. Kamaras, A. Pekker, B. Botka, H. Hu, S. Niyogi, M. E. Itkis, R. C. Haddon, *Phys. Status Solidi B* , **247**, 2754-2757 (2012).

[114] H. Kobayashi, Asuha, O. Maida, M. Takahashi, H. Iwasa, *J. Appl. Phys.*, 94, 7328-7335 (2003).

[115] J. Sheng, K. Fan, D. Wang, C. Han, J. Fang, P. Gao, J. Ye, *ACS Appl. Mater. Interfaces*, **6**, 16027-16034 (2014).

[116] C. Pintossi, S. Pagliara, G. Drera, F. De Nicola, P. Castrucci, M. De Crescenzi, M. Crivellari, M. Boscardin and L. Sangaletti, *ACS Appl. Mater. Interfaces*, **7** (18), 9436-9444 (2015).

[117] F. J. Himpsel, F. R. McFeely, A. Taleb-Ibrahimi, J. A. Yarmoff, G. Hollinger, *Phys. Rev. B: Condens. Matter Mater. Phys.*, **38**, 60846096 (1988).

[118] G. Mende, J. Finster, D. Flamm, D. Schulze, *Surf. Sci.*, **128**, 169-175 (1983).

[119] See, for example, M. Ohtsu, M., Ed. Optical and Electronic Process of Nano-Matters; Springer Science+Business Media: Dordrecht, the Netherlands, (2001) Chapter 10 and refs therein.

[120] G. Hollinger and F. J. Himpsel, *Appl. Phys. Lett.*, 44, 93-95 (1984).

[121] M. Zubaer Hossain, *Appl. Phys. Lett.*, **96**, No. 053118 (2010).

[122] J. Di, Z. Yong, X. Zheng, B. Sun, B. Li, *Small*, 9, 1367-1372 (2013).

[123] W. Zhou, J. Vavro, N. M. Nemes, J. E. Fischer, F. Borondics, K. Kamaras, D. B. Tanner, *Phys. Rev. B: Condens. Matter Mater. Phys.*, **71**, No. 205423 (2005).

[124] P. L. Ong, W. B. Euler, I. A. Levitsky, *Nanotechnology*, **21**, No. 105203 (2010).

[125] G. Galimberti, S. Ponzoni, A. Cartella, M. T. Cole, S. Hofmann, C. Cepek, G. Ferrini, S. Pagliara, *Carbon*, **57**, 50-58 (2013).

[126] S. Ponzoni, G. Galimberti, L. Sangaletti, P. Castrucci, S. Del Gobbo, M. Morbidoni, M. Scarselli and S. Pagliara, *J. Phys. Chem. C*, **118**, 2411024116 (2014).

[127] G. Galimberti, S. Pagliara, S. Ponzoni, S. Dal Conte, F. Cilento, G. Ferrini, S. Hofmann, M. Arshad, C. Cepek, F.Parmigiani. The photoinduced charge transfer mechanism in aligned and unaligned carbon nanotubes. *Carbon*, **49**, 15, 5246-5252 (2011).

[128] N. O. Haugen, A- B. Phillips, T. E. Dykstra, S. Watthage, M. J. Heben, R. J. Ellingson, *J. Phys. Chem. C*, **118**, 43, 25253-25260 (2014).

[129] J. S. Lauret, C. Voisin, G. Cassabois, C. Delalande, P. Roussignol, O. Jost, and L. Capes, *Phys. Rev. Lett.*, **90**, 057404-4 (2003).

[130] L. Huang, H. N. Pedrosa, T. D. Krauss, *Phys. Rev. Lett.*, **93**, 017403-4 (2004).

[131] M. Ichida, S. Saito, Y. Miyata, K. Yanagi, H. Kataura, and H. Ando, *Eur. Phys. J. B*, **86**, 45-5 (2013).

Acknowledgement & Ringraziamenti

At the end of this thesis, I want to spend some word to acknowledge all the people who have made this possible.

First of all, Prof. Luigi Sangaletti, for giving me the opportunity to work with him in his research group for this three years, allowing me to travel a lot, to talk in international conferences, to meet inspiring people and to grow as a researcher and especially as a person.

Thanks to all the Carbon Lab at the Physics department of Roma Tor Vergata, in particular to Paola Castrucci and Francesco De Nicola, not only for providing samples and for the fruitful collaborations and discussions but also for the warm hospitality in Rome.

Thanks to all the people of the Elphos Lab, leaded by Prof. Stefania Pagliara, for guesting me during the time-resolved reflectivity measurements, and in particular to S. Ponzoni for teaching me this new experimental technique and for the support during measurements.

I want to thank Carla Bittencourt, for accepting to be my referee and to be present at the discussion.

Finally, thanks to Keith Richards, because, well, HE IS KEITH RICHARDS!!

Il primo ringraziamento va a mamma Sonia, sapientina e lentaintutto, per mille e piú cose ma soprattutto per avermi finalmente permesso di sperimentare come il vero viaggio non sia nel vedere nuove cose ma nell'avere nuovi occhi.

Grazie al papá Fulvio, per avermi trasmesso fin da bambina la passione per la buona musica grazie alla *canzone dell'elicottero* e per avermi mostrato l'esistenza e la percorribilitá della via del cambiamento, quando ho finalmente deciso di accettare il mio carattere come parte del suo.

Grazie Maria! Sei la mia piccola grande sorellina ed essere un modello per te, mi sprona ogni giorno ad essere migliore.

Grazie alla piccola nonna Rosa, tecnologica, cattiva, troppo sincera e con un carattere inscalfibile, per avermi sempre accolta quando ad ogni etá andavo a suonarle nel cuore della notte con il mio cuscino sotto il braccio.

Grazie allo zio Giovannino, il preferito da tutti, per essere sempre stato un grande amico e che, come tutti i grandi amici, so di avere sempre al mio fianco, indipendentemente da quanto ci si veda o ci si senta.

Grazie a Cecilia per il supporto e sostegno, sempre aiutato dalla qualitá del miglior negozio di Inzino e del mondo "La bottega di Duilia"(andate tutti a comprare!!!).

Ed ora finalmente, grazie a voi, mie Spice+1! Siete stati la parte migliore del mio dottorato: é stato un onore ed un privilegio conoscervi e condividere questo percorso (e queste tequile) con voi. Grazie in primis alla bullissima Federica, una Accademia della Crusca in pratica edizione tascabile (#processodellunedí), grazi*a* a Silvia, per avermi insegnato le abitudini dei volatili meglio di quanto avrebbe potuto fare Piero Angela (#rafatocco) e grazie a Stefano per avermi sempre ricordato chi sia il vero nemico: "percheé sapete, non ci sono mai giorni in cui mi sveglio e dico: Ma.. sí.. peró, in effetti.. il diavolo...(#diavoloporco)."Il laboratorio é stata una bella spinta ma sono sicura che ci saremmo scelti ugualmente. Ora mi si stanno cariando i denti, quindi... Andatevene aff*****o!

Grazie a Giovanni, compagno di Man & Woman *vs* Food (& Dignity), a Miss Muretto (in faccia) Alessio, per avermi fornito spunti sempre nuovi su a chi sparare i *bang* del primo giro, e al migliore amico di ogni commerciante Emanuele. So long, and thanks for all the (raw) fish!

Grazie a tutti gli amici di Lumezzane (e dintorni): all'unico uomo al mondo che si vergogna di dire che il suo cognome finisce con la lettera Y, Paolo Gnaly; allo stupido, cretino, mongolo, papagal, ma molto devoto, Bono; alla mia compagna di levatacce ed insulti alle divinitá vecchie e nuove quando il sole non é ancora sorto, Giulia; a colui che ha iniziato e *finito* con me, Zizzo; al classe nocciolina dentro la doccia, Andrea; alla lanciatrice di croccantini Giuly; a quello che viene da Scampia, Longo; alla migliore scavalcatrice di guinzagli, Cry; al bellissimo Paci, ai compagni di acqua solida Stefano e Davide, al giornalista Fabio e al Brad Pitt di Mongiana, Bruno. Ricordatevi sempre che senza Lo Zio non saremmo nessuno!

Ed infine grazie, grazie a tutte le persone che hanno iniziato con me questo percorso e a chi ha saputo entrare dopo, sbirciando dalla serratura o buttandosi prepotentemente in scena, a tutti quelli che sono ancora qui oggi a condividere gioie, speranze, paure, sbornie e barzellette sui muffin. E grazie anche a chi si é perso per strada, a chi si é allontanato per scelta e a coloro con i quali la vita ha sempliemente allentato le maglie dei rapporti.

Ma soprattutto grazie a te, che non c'eri all'inizio, che non ci sarai alla fine, che ci sei ogni giorno, flebile e continuo come un sussurro, assordante e vivo come un tuono che scuote l'angolo malato e santo, dolorante e caldo del mio essere piú profondo. Grazie Davide perché son cresciuta con te e perché in te continuo a crescere.